



UNIVERSITÀ DEGLI STUDI DI PISA

Dipartimento di Ingegneria dell'Informazione:  
Elettronica, Informatica, Telecomunicazioni

Dottorato di Ricerca in Applied Electromagnetism in  
electrical and biomedical engineering, electronics,  
smart sensors, nano-technologies

**Transport and Noise properties of  
silicon and carbon one-dimensional  
devices**

**Alessandro Betti**

Tutori: **Giuseppe Iannaccone**

**Gianluca Fiori**

Pisa, Febbraio 2011



# Contents

<b>1</b>	<b>Introduction</b>	<b>1</b>
1.1	Organization of the thesis . . . . .	5
1.2	The NEGF formalism . . . . .	6
1.2.1	Basis set for Hamiltonian of the isolated channel .	7
1.2.2	Self-energies . . . . .	9
1.2.3	Computation of the Green Function . . . . .	14
1.2.4	Carrier density and current . . . . .	15
1.2.5	Quasi-one dimensional systems: Carbon Nanotubes	17
<b>2</b>	<b>Statistical theory of shot noise in the presence of electron-electron interaction</b>	<b>19</b>
2.1	Generalization of the Landauer-Büttiker formula to in- clude Coulomb repulsion . . . . .	21
2.2	Computational methodology . . . . .	31
2.3	Concluding remarks . . . . .	35
<b>3</b>	<b>On the shot noise in quasi-1D FETs computed by means of Monte Carlo simulations</b>	<b>37</b>
3.1	Simulated devices . . . . .	38
3.2	DC Characteristics . . . . .	39
3.3	Shot noise suppression in (13,0) CNT-FETs and SNW-FETs	41
3.3.1	On the importance of exchange interference effects on current fluctuations . . . . .	46
3.3.2	Shot noise versus thermal channel noise . . . . .	48
3.3.3	Effect of scaling on noise . . . . .	50
3.4	Enhanced shot noise in CNT-FETs . . . . .	51
3.5	Concluding remarks . . . . .	62

<b>4</b>	<b>Atomistic investigation of low-field mobility in graphene nanoribbons</b>	<b>63</b>
4.1	Methodology . . . . .	64
4.2	Results and Discussions . . . . .	69
4.2.1	Line-edge roughness limited mobility . . . . .	69
4.2.2	Defect-limited mobility . . . . .	71
4.2.3	Ionized impurities limited mobility . . . . .	73
4.2.4	Acoustic and optical phonon-limited mobility . . . . .	75
4.3	Concluding remarks . . . . .	77
<b>5</b>	<b>Strong mobility degradation in graphene nanoribbons due to phonon scattering</b>	<b>79</b>
5.1	Full-band approach . . . . .	82
5.1.1	GNR phonons . . . . .	82
5.1.2	Remote phonons . . . . .	91
5.2	Low-field GNR phonon-limited mobility . . . . .	93
5.3	Results . . . . .	94
5.3.1	Scattering rates . . . . .	95
5.3.2	Optical energy offset . . . . .	98
5.3.3	Effect of the intrasubband intravalley scattering approximation . . . . .	100
5.3.4	Low-field GNR phonon-limited mobility and mean free path . . . . .	102
5.3.5	Effect of temperature . . . . .	107
5.3.6	Acoustic and optical phonon-limited mobility . . . . .	107
5.3.7	Remote phonon-limited mobility . . . . .	111
5.3.8	Comparison with results present in the literature . . . . .	113
5.3.9	Polarons in armchair GNRs . . . . .	117
5.4	Concluding remarks . . . . .	118
<b>A</b>	<b>Alternative derivation of the shot noise formula</b>	<b>121</b>
<b>B</b>	<b>The Fischer-Lee relation</b>	<b>127</b>
<b>C</b>	<b>Approximations of electron-phonon scattering</b>	<b>129</b>
C.1	Approximation IIS: intrasubband intravalley scattering . . . . .	129
C.2	Approximation IISNS: neglect of the spinor . . . . .	133
C.3	Approximation 2DPNS: neglect of the spinor and 2D phonons . . . . .	134
	<b>Bibliography</b>	<b>137</b>

<b>List of Acronyms</b>	<b>151</b>
<b>Curriculum Vitae</b>	<b>153</b>



# Acknowledgments

First of all, I would like to thank my advisor Prof. Giuseppe Iannaccone for the valuable guidance and the stimulating discussions during the course of this work, and the researcher Gianluca Fiori for his essential support to my work.

In particular, I would like to spent some words regarding Gianluca Fiori, which not only guided me in my research with availability and patience, but also he has represented a truthful friend. To him, I tribute a fervent thank.

I also wish to express my gratitude for the benefits that I have gained from conversations with the other members of the Nanoelectronic group, in particular Dr. Paolo Michetti and Dr. Paolo Marconcini. I also thank Valentina Bonfiglio, a member of the Nanoelectronic group, which has represented a very free-spoken friend during these years.

Finally, I would like to thank my parents, Romano and Nadia and my brother Francesco for their indispensable support in this part of my life.





# Chapter 1

## Introduction

In the last few decades, semiconductor technology has been characterized by an impressive decrease in device size and a similar increase in performance. In particular, according to the Moore's law, the number of transistors, based on the Complementary Metal-Oxide Semiconductor (CMOS) silicon-based technology, which can be placed on an integrated circuit are expected to double approximately every two years. The trend is continued for more than half a century and is not expected to stop until 2015 or later. Actually, the 32 nm technology modules is now being used by the major chipmakers for industrial production. In addition, the first solutions to the extraordinary challenges in scaling, transistor architecture, lithography technique posed by the 15 nm technology node start to be investigated.

However, in a near future, power dissipation, presence of unintentional doping and of single-atom defect distributions will make further miniaturization more difficult and less convenient. Indeed, despite aggressive downscaling results in higher device density and device frequency and in the reduction of supply voltage and power dissipation of individual transistors, the total power dissipation per unit area and the electrical current in the subthreshold regime increase inversely with the device dimensions, therefore degrading the ratio of ON to OFF-state currents  $I_{\text{ON}}/I_{\text{OFF}}$  and limiting DC performance figures. On the other

hand, new emerging materials may represent a great opportunity for the development of alternative technology for nanoelectronics.

In this context, the development of devices based on carbon nanotubes [1] or on the recently synthesised graphene [2], the two-dimensional form of carbon with atoms ordered in a honeycomb lattice (Fig. (1.1)), has represented in the last decade an appealing opportunity to go beyond silicon CMOS. It may be one of the most promising and versatile materials ever discovered. The strong interest in graphene electronics has been driven by its extraordinary properties, such as an high mobility even at room temperature [3, 4, 5, 6], a large mean free path [7] and the near massless (relativistic-like) behavior of its charge carriers [8]. It is also one of the most strongest and lightest materials known to humankind. However, in despite of many advantages, graphene presents also a defect. Indeed it is a semimetal, i.e. it has no bandgap, and thus is unsuitable for use as a channel in a field-effect transistors. In order to open a bandgap, graphene has to be laterally confined, as in a Graphene NanoRibbon (GNR), or has to be rolled up as a Carbon NanoTube (CNT). Alternatively, graphene can be hydrogenated by exposing it to a stream of hydrogen atoms to produce graphane [9, 10], or it can be used to realize a graphene bilayer transistor [11], where the mirror-like symmetry of the two layers is broken by the electric field of the gate electrodes, opening a widely tunable electronic bandgap.

In 2008, 1 nm-wide GNR transistors were created [12]. They were only one atom thick and 10 atoms across, with a size not much larger than that of a molecule. They were not only smaller than the smaller silicon transistors, but they could also represent the absolute physical limit of Moore's law governing the shrinking size and growing speed of computer processors. However, graphene can not only be used for the realization of super-small transistors. Indeed, new type of graphene-based, flash-like storage memory, more dense and less lossy than any existing storage technology have been created [13], and graphene films can be also exploited to creat new ultracapacitors to store and transmit electrical power [14]. In addition, due to its strength, flexibility and light-sensitivity, graphene could improve the efficiency of solar cells and LEDs [15]. It can also aid the production of next-generation devices like flexible touch screens, photodetectors and ultrafast lasers, replacing rare and expensive metals like platinum and indium, performing the same tasks with greater efficiency at a fraction of the cost.

In this thesis, we study fundamental properties of transport and noise in quasi-one dimensional (1D) devices, with particular attention

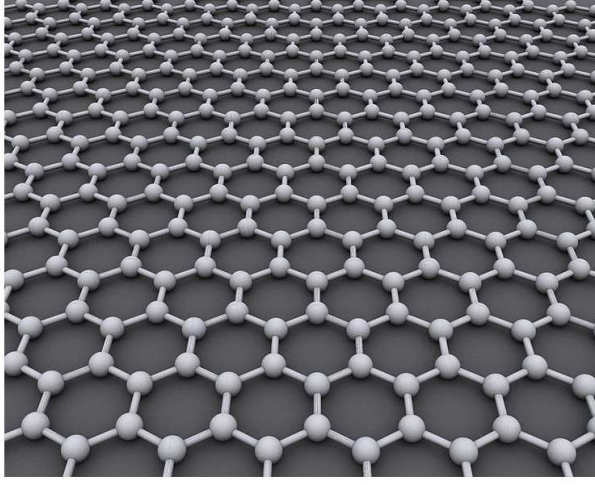


Figure 1.1: A two-dimensional graphene sheet (*From Wikipedia, the free encyclopedia.*)

to carbon-based devices. The thesis has two main themes.

The first theme is shot noise in one-dimensional transistors based on carbon nanotubes (CNTs) and silicon nanowires (SNWs). In these quasi-1D devices, electrical noise places serious limits on device performance, due the reduced amount of electron charge in the channel, where electron count can be of the order of few units, leading to an extreme sensitiveness of device performance to charge fluctuations. Of course, noise may represent a hindrance to signal detection. More likely, it can be used to probe the kinetics of electrons by investigating the interaction between carriers, which affect noise by controlling their relative motion and is particularly important in nanoscaled conductors due to the reduced electrostatic screening.

Pauli exclusion principle and Coulomb repulsion represent the main types of interaction affecting noise. As known, Pauli principle alone suppresses noise. Indeed electrons are fermions. As a consequence, due to the wave nature of electrons, Pauli principle restricts the occupation of quantum-mechanical states and spread electrons more uniformly among the available wave-packets, thus regulating the electron flow and reducing shot noise below the full value predicted for completely uncorrelated

carriers. Instead, Coulomb repulsion can either suppress or enhance electrical noise and in general its contribution to shot noise cannot be neglected. For example, noise enhancement, due to Coulomb force, has been already observed in resonant tunneling diodes [16], because of the positive feedback between successive electrons tunneling into resonant states of the quantum well. Instead in ballistic CNT and SNW-FETs many questions still remain unanswered. Indeed, although noise measurements [17] points out the need to build a theoretical model including also many-body corrections, so far this issue has not yet received significant attention [16]. Here we address the problem of the shot noise evaluation under the conditions of the interplay between Pauli and Coulomb interactions in ballistic CNT and SNW-FETs.

The second theme is mobility in graphene nanoribbons. Despite the fact that suspended 2D graphene has an intrinsic mobility at room-temperature several orders of magnitude larger than that of bulk semiconductors, state-of-the art GNRs present many scattering sources, which strongly limit electron transport [12, 18]. Indeed, although atomically smooth edges and clean GNR samples are essential for many applications, to open a gap of just 1 eV in graphene would mean making GNRs narrower than 2 nm with single atom precision, something which is difficult by exploiting conventional physico-chemical methods. Defects [19], in the bulk and at the edge, impurities [20], phonon scattering [21] and surface phonon scattering [22] due to the polar nature of gate dielectrics used in such devices, strongly degrade mobility with respect to 2D graphene flakes. On the other hand, experiments do not allow to isolate each scattering source in order to evaluate its impact on mobility: only the total electron mobility can be measured. In this context, theory can be of great help to individually evaluate the impact of each scattering source on mobility. In particular, device simulations on an atomistic scale, presented in chapter 4, may represent a very useful tool to understand effects observed experimentally or even to predict new effects in nanoscaled channels, which the present technology is not able to pattern.

Of course, in order to assess if graphene-based electronics represents a real alternative to silicon CMOS, simulations have also to be performed for the best possible case scenarios, which in a near future could be reached, when only lattice vibrations are present and all extrinsic scattering sources have been suppressed. Indeed phonon scattering represents the unavoidable scattering mechanism at a finite temperature, in the case of an ideally perfect GNR, and provides useful informations

of the potential for the material in electronics, either for devices or interconnects [23]. Actually, although many theoretical works have been published concerning transport limited by electron-phonon scattering in 2D graphene [24, 25, 26, 22, 27, 28], very few indications are present in GNRs [21]. Here a very accurate full-band approach to evaluate low-field phonon-limited mobility in GNRs is proposed.

## 1.1 Organization of the thesis

In the next section of Chapter 1, we introduce the non-equilibrium Green function method, due to its importance in order to solve quantum transport problems.

Chapter 2 is mainly devoted to the theoretical background exploited in order to compute shot noise in quasi-one dimensional Field Effect Transistors (FETs). In particular, we present a novel expression for the shot noise power spectral density in quasi-one dimensional conductors electrostatically controlled by a gate electrode, that includes the effects of Coulomb interaction and of Pauli exclusion among charge carriers, the main types of interaction that have a clear effect on noise. In this sense, this expression extends the well known Landauer-Büttiker noise formula to include the effect of Coulomb interaction inducing fluctuations of the potential in the device region. This approach is based on evaluating the statistical properties of the scattering matrix and on a second-quantization many-body description. In the last part of the chapter, we present instead the simulation methodology. In particular, statistical properties are obtained by means of Monte Carlo simulations on an ensemble of different configurations of injected states, requiring the solution of the Poisson-Schrödinger equation on a three-dimensional grid, with the non-equilibrium Greens functions formalism.

In chapter 3, by means of the simulation methodology presented in the previous chapter, we show in a series of examples about (13,0) CNT-FET and SNW-FET that failure to consider the effects of Coulomb interaction on noise leads to a gross overestimation of the noise spectrum. In particular, the suppressed noise observed in these devices can be overestimated up to the 180% by only using the Landauer-Büttiker formula, i.e. by considering only the Pauli exclusion principle. However, correlations among electrons can also lead to an enhanced noise, or superpoissonian noise. Actually, this is the subject of the last section in chapter 3, where we predict noise enhancement in (25,0) CNT-FETs, due

to peculiar shape of the density of states in the channel, which gives rise to a positive correlation between trapping of holes from the drain into quasi-bound states in the channel and thermionic injection of electrons from the source.

In chapter 4 we investigate the main scattering mechanisms affecting mobility in state-of-the-art GNRs using detailed atomistic simulations. We consider carrier scattering due to acoustic and optical phonons, edge roughness, single-atom defects, and ionized impurities, by exploiting a methodology based on simulations of statistically meaningful ensembles of nanoribbon segments. Edge disorder and defects heavily affects mobility at room temperature in narrower nanoribbons due to quantum localization phenomena, whereas charged impurities and phonons are hardly the limiting factors. Results are also favorably compared to the few experiments available in the literature.

Finally, in chapter 5 we focus our attention on phonon-limited mobility in GNRs. Indeed, with the progressive improvement of graphene preparation methods and the consequent realization of clean graphene samples, understanding the role of phonon scattering in graphene-based electronics becomes of primary importance, since the coupling between electrons and the semiconductor lattice determines the ultimate intrinsic mobility limit of any electronic devices. In particular, we use a full band approach to investigate the low-field phonon-limited mobility in sub-10-nm armchair GNRs. Scattering rates are obtained within the deformation potential approximation, whereas the mobility is calculated by means of the Kubo-Greenwood formula. Mobility close to  $500 \text{ cm}^2/\text{Vs}$  is found for 1 nm-wide GNRs, corresponding to coherence length of  $\approx 10 \text{ nm}$  or smaller, very far from the ballistic limit. When depositing GNRs on  $\text{HfO}_2$ , surface phonons largely degrade mobility down to  $100 \text{ cm}^2/\text{Vs}$  even for small temperatures ( $\approx 100 \text{ K}$ ). Polaron formation is observed in armchair GNRs, with a band gap renormalization of  $\approx 118 \text{ meV}$  for 1 nm-wide GNRs.

## 1.2 The NEGF formalism

The Non-Equilibrium Green Function (NEGF) formalism [29, 30, 31, 32] provides a powerful tool for the development of atomic-level quantum mechanical simulators that are needed for nanoscale devices, such as those based on Carbon Nanotubes (CNTs) or Silicon NanoWires (SNWs). The NEGF formalism essentially consists of four steps.

The first step consists in identifying a suitable basis set to be used for the representation of the Hamiltonian matrix  $H$  for the isolated channel. In this step, the self-consistent potential computed by solving the electrostatic and transport equations has to be properly included in  $H$ . The second step is to compute the self-energy matrices  $\Sigma_S$  and  $\Sigma_D$  which describe the coupling between the channel and the source ( $S$ ) and drain ( $D$ ) reservoirs. Scattering processes can be also considered by properly considering an additional self-energy  $\Sigma_{SC}$ . For the sake of simplicity, in the following only ballistic transport will be treated. After  $H$ ,  $\Sigma_S$  and  $\Sigma_D$  are known, the third step is to compute the retarded Green's function as:

$$\mathbf{G}(E) = \frac{1}{(E + i0^+) \mathbf{I} - \mathbf{H} - \mathbf{\Sigma}_S - \mathbf{\Sigma}_D} \quad (1.1)$$

Once  $\mathbf{G}$  is known, all physical quantities of interest can be derived.

### 1.2.1 Basis set for Hamiltonian of the isolated channel

Now we address the question of how we can calculate the Green's function. In the following we will assume for simplicity a 1D system along the  $x$  direction, which anyway retains all properties useful for the understanding of the method. Generalization to systems having a larger complexity can be found in specialized papers on the subject [30, 31, 32, 33]. The 1D Schrödinger equation for the channel coupled to source and drain leads reads:

$$H\Psi(x) = E\Psi(x) \quad (1.2)$$

where  $H$  is the Hamiltonian defined as:

$$H = -\frac{\hbar^2}{2m} \frac{d^2}{dx^2} + E_C + U(x) \quad (1.3)$$

where  $E_C$  is the conduction band minimum, whereas  $U(x)$  is the self-consistent potential and  $m$  is the effective mass.

To obtain a matrix representation for  $H$ , we use a discrete lattice in real space [29, 30]: we choose a lattice whose points are located at  $x_n = (n - 1)a$ , where  $a$  is the lattice constant and  $n$  is an integer (Fig. (1.2)). In particular,  $1 \leq n \leq N$  denote lattice points in the channel, whereas  $n \leq 0$  and  $n \geq (N+1)$  refer to points in the source and drain

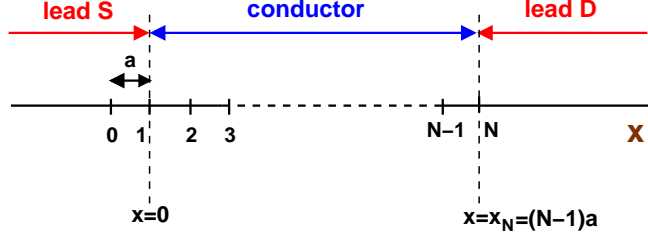


Figure 1.2: A 1D conductor connected to two semi-infinite leads (source (S) and drain (D)) discretized into a lattice.

leads. Now we adopt the method of finite differences to approximate the derivative operators. Assuming  $a$  to be small, the first derivative can be approximated as:

$$\left. \frac{d\Psi}{dx} \right|_{x=x_n} = \frac{\Psi_{n+1} - \Psi_n}{a}, \quad (1.4)$$

where  $\Psi_n = \Psi(x = x_n)$ . The second derivative reads instead:

$$\left. \frac{d^2\Psi}{dx^2} \right|_{x=x_n} = \frac{\Psi_{n+1} + \Psi_{n-1} - 2\Psi_n}{a^2}, \quad (1.5)$$

With this approximation, Eqs. (1.2) and (1.3) become:

$$(H\Psi)_{x=x_n} = -t_0\Psi_{n+1} + (E_C + 2t_0 + U_n)\Psi_n - t_0\Psi_{n-1} = E\Psi_n, \quad (1.6)$$

where  $t_0 = \hbar^2/(2ma^2)$  and  $U_n = U(x = x_n)$ . Eq. (1.6) give us the desired matrix representation for the Hamiltonian operator of a 1D system:

$$\mathbf{H} = \begin{pmatrix} \cdots & -t_0 & 0 & \cdots & \cdots & 0 & 0 \\ -t_0 & \tilde{U}_0 & -t_0 & 0 & \cdots & 0 & 0 \\ 0 & -t_0 & \tilde{U}_1 & -t_0 & 0 & 0 & 0 \\ 0 & 0 & \ddots & \ddots & \ddots & 0 & 0 \\ 0 & 0 & 0 & -t_0 & \tilde{U}_N & -t_0 & 0 \\ 0 & 0 & 0 & 0 & -t_0 & \tilde{U}_{N+1} & -t_0 \\ 0 & 0 & 0 & 0 & 0 & -t_0 & \cdots \end{pmatrix} \quad (1.7)$$

where  $\tilde{U}_n = E_C + 2t_0 + U_n$ .



It is worth noticing the similarity of the discretized Hamiltonian to the tight-binding Hamiltonian. Indeed in the latter model, the wavefunction is expressed in terms of localized atomic orbitals and the coupling between orbitals on neighboring sites is given by the hopping matrix element. In our case the local potential  $\tilde{U}_n$  at each lattice point corresponds to the energy of the orbital localized at the site  $x_n$ , whereas  $t_0$  is the hopping matrix element between orbital on nearest neighboring sites. Note also that the  $N \times N$  central block  $H_0$ :

$$\mathbf{H}_0 = \begin{pmatrix} \tilde{U}_1 & -t_0 & 0 & 0 & 0 \\ -t_0 & \tilde{U}_2 & -t_0 & 0 & 0 \\ 0 & \ddots & \ddots & \ddots & 0 \\ 0 & 0 & \ddots & \ddots & \ddots \\ 0 & 0 & 0 & -t_0 & \tilde{U}_N \end{pmatrix}_{N \times N} \quad (1.8)$$

represents the Hamiltonian of the isolated channel.

### 1.2.2 Self-energies

As can be seen in Eq. (1.7), since the channel is connected to semi-infinite leads,  $H$  is infinite dimensional. In order to properly describe an open system with non-reflecting boundaries, the matrix  $H$  cannot be arbitrarily truncated at some points in the leads. The advantage of the use of the NEGF formalism to solve the transport equation is to truncate the infinite interaction submatrices of source and drain contacts in  $H$  by means of the self-energies [29, 30]. For closed systems there is a little reason to use Green's function. Instead for open systems the Green's function method allows to focus on the device of interest and to replace the effect of all external reservoirs with self-energy functions, which are matrices of the same size as the channel Hamiltonian, even for semi-infinite contacts. This is the key concept of the NEGF method. In the following, we will consider separately the coupling between the channel and the source, and the channel and the drain. Later, we will combine the two results in order to consider the most general situation of coupling with either the source and drain reservoirs.

The self-energy  $\Sigma_S$  accounting for the source leads on the left can be obtained in the following way. We start from the Schrödinger equation for the wavefunction  $\Psi_1 = \Psi(x=0)$ . By means of Eq. (1.6), it reads:

$$(E_C + 2t_0 + U_1) \Psi_1 - t_0 \Psi_2 - t_0 \Psi_0 = E \Psi_1. \quad (1.9)$$

Then we consider an incident plane wave with wavevector  $k_1$  in the source lead. The wave is partially reflected in the source and partially transmitted in the drain, therefore for  $x \leq 0$  the more general wavefunction reads:

$$\Psi(x) = e^{ik_1x} + re^{-ik_1x} \quad x \leq 0 \quad (1.10)$$

where  $r$  is the reflection coefficient. As a consequence:

$$\Psi(x=0) = \Psi_1 = 1 + r \quad (1.11)$$

and

$$\Psi(x=-a) = \Psi_0 = e^{-ik_1a} + re^{ik_1a} \quad (1.12)$$

By exploiting Eqs. (1.11) and (1.12), we can express  $\Psi_0$  as a function of  $\Psi_1$ :

$$\Psi_0 = \Psi_1 e^{ik_1a} - (e^{ik_1a} - e^{-ik_1a}) \quad (1.13)$$

As a result, we can finally eliminate  $\Psi_0$  from Eq. (1.9), by substituting Eq. (1.13) in Eq. (1.9):

$$E\Psi_1 - [(E_C + 2t_0 + U_1 - t_0 e^{ik_1a}) \Psi_1 - t_0 \Psi_2] = t_0 (e^{ik_1a} - e^{-ik_1a}) \quad (1.14)$$

As can be seen in Eq. (1.14), all we need in order to account exactly for the semi-infinite source lead is to put a term  $-t_0 e^{ik_1a}$  to  $(H_0)_{11} = \tilde{U}_1$  in Eq. (1.8) and to add a term  $t_0 (e^{ik_1a} - e^{-ik_1a})$  to the right side of Eq. (1.14).

For the drain lead on the right a similar procedure can be followed. We consider the Schrödinger equation for the wavefunction  $\Psi_N = \Psi(x = (N-1)a)$ :

$$(E_C + 2t_0 + U_N) \Psi_N - t_0 \Psi_{N+1} - t_0 \Psi_{N-1} = E\Psi_N. \quad (1.15)$$

Since the plane wave incident in the source lead is partially transmitted in the drain lead, we can write:

$$\Psi(x) = t' e^{ik_2x} \quad x \geq x_N = (N-1)a \quad (1.16)$$

where  $k_2$  is the wavevector in the drain region and  $t'$  is the source-to-drain transmission coefficient. In order to eliminate  $\Psi_{N+1}$  from Eq. (1.15),  $\Psi_{N+1}$  has to be expressed as a function of  $\Psi_N$ :

$$\Psi_{N+1} = t' e^{ik_2Na} = e^{ik_2a} \Psi_N. \quad (1.17)$$

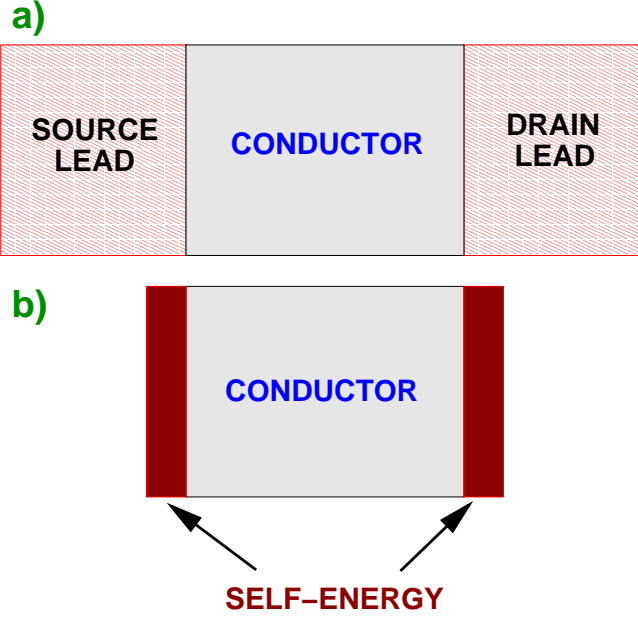


Figure 1.3: The introduction of the self-energy terms allows to replace a conductor connected to semi-infinite leads (a) by an equivalent finite conductor with self-energy terms (b).

By substituting Eq. (1.17) in Eq. (1.15), we finally obtain:

$$E\Psi_N - [(E_C + 2t_0 + U_N - t_0e^{ik_2a})\Psi_N - t_0\Psi_{N-1}] = 0. \quad (1.18)$$

Similar to the case of the source lead, we have just to add the term  $-t_0e^{ik_2a}$  to  $(H_0)_{NN} = \tilde{U}_N$  in order to account for the semi-infinite drain lead. In conclusion, the introduction of the self-energies, which describes the effect of the coupling between leads and conductor, allows us to replace an infinite open system with a finite one (Fig. (1.3)).

The effective Hamiltonian  $N \times N$  accounting for open boundary conditions reads:

$$\mathbf{H} = \mathbf{H}_0 + \Sigma_S + \Sigma_D, \quad (1.19)$$

where  $H_0$  is given in Eq. (1.8), whereas  $\Sigma_S$  reads:

$$\Sigma_S = \begin{pmatrix} -t_0 e^{ik_1 a} & 0 & 0 & 0 & 0 \\ 0 & 0 & 0 & 0 & 0 \\ 0 & \ddots & \ddots & \ddots & 0 \\ 0 & 0 & \ddots & \ddots & \vdots \\ 0 & 0 & 0 & 0 & 0 \end{pmatrix}_{N \times N} \quad (1.20)$$

and  $\Sigma_D$  is:

$$\Sigma_D = \begin{pmatrix} 0 & 0 & 0 & 0 & 0 \\ 0 & 0 & 0 & 0 & 0 \\ 0 & \ddots & \ddots & \ddots & 0 \\ 0 & 0 & \ddots & \ddots & \vdots \\ 0 & 0 & 0 & 0 & -t_0 e^{ik_2 a} \end{pmatrix}_{N \times N} \quad (1.21)$$

Eq. (1.2) can be finally expressed as:

$$[E\mathbf{I} - \mathbf{H}_0 - \Sigma_S - \Sigma_D] \Psi = \mathbf{G}^{-1} \Psi = i\gamma_S, \quad (1.22)$$

where  $\Psi$  reads:

$$\Psi = \begin{pmatrix} \Psi_1 \\ \vdots \\ \vdots \\ \Psi_N \end{pmatrix}_{N \times 1} \quad (1.23)$$

and  $\gamma_S$  is the so-called broadening function, for a reason which will be clear in the following [29, 30]:

$$\gamma_S = \begin{pmatrix} -i t_0 (e^{ik_1 a} - e^{-ik_1 a}) \\ 0 \\ \vdots \\ 0 \end{pmatrix}_{N \times 1} = \begin{pmatrix} i [(\Sigma_S)_{11} - (\Sigma_S)_{11}^*] \\ 0 \\ \vdots \\ 0 \end{pmatrix}_{N \times 1} \quad (1.24)$$

From a theoretical point of view,  $\gamma_S$  can be seen as an external excitation, whereas  $\mathbf{G}$  give us the response to this excitation:  $\Psi = i\mathbf{G}\gamma_S$ . As already

remarked, we have assumed only source injected states. If one considers instead only states injected from the drain, the broadening function for the drain contact  $\gamma_{\mathbf{D}}$  is obtained [30]:

$$\gamma_{\mathbf{D}} = \begin{pmatrix} 0 \\ \vdots \\ 0 \\ -i t_0 (e^{ik_2 a} - e^{-ik_2 a}) \end{pmatrix}_{N \times 1} = \begin{pmatrix} 0 \\ \vdots \\ 0 \\ i [(\Sigma_{\mathbf{D}})_{NN} - (\Sigma_{\mathbf{D}})_{NN}^*] \end{pmatrix}_{N \times 1} \quad (1.25)$$

As a consequence, when the coupling with the drain extensions is taken into account, Eq. (1.22) has to be modified in the following form:

$$[E\mathbf{I} - \mathbf{H}_0 - \Sigma_{\mathbf{S}} - \Sigma_{\mathbf{D}}] \Psi = \mathbf{G}^{-1} \Psi = i\gamma_{\mathbf{D}}. \quad (1.26)$$

We would like also to remark that there are two factors that distinguish  $\Sigma_{\mathbf{S}}$  and  $\Sigma_{\mathbf{D}}$  from ordinary Hamiltonians. First, they are energy dependent. Second, we can write:

$$\begin{aligned} \mathbf{H}_0 + \Sigma_{\mathbf{S}} + \Sigma_{\mathbf{D}} &= \left( \mathbf{H}_0 + \frac{\Sigma_{\mathbf{S}} + \Sigma_{\mathbf{S}}^\dagger}{2} + \frac{\Sigma_{\mathbf{D}} + \Sigma_{\mathbf{D}}^\dagger}{2} \right) \\ &+ \left( \frac{\Sigma_{\mathbf{S}} - \Sigma_{\mathbf{S}}^\dagger}{2} + \frac{\Sigma_{\mathbf{D}} - \Sigma_{\mathbf{D}}^\dagger}{2} \right) \\ &= \tilde{\mathbf{H}}_0 - i \frac{\Gamma_{\mathbf{S}}}{2} - i \frac{\Gamma_{\mathbf{D}}}{2} \end{aligned} \quad (1.27)$$

where

$$\tilde{\mathbf{H}}_0 = \mathbf{H}_0 + \frac{\Sigma_{\mathbf{S}} + \Sigma_{\mathbf{S}}^\dagger}{2} + \frac{\Sigma_{\mathbf{D}} + \Sigma_{\mathbf{D}}^\dagger}{2} \quad (1.28)$$

and

$$\Gamma_{\mathbf{S}} = i [\Sigma_{\mathbf{S}} - \Sigma_{\mathbf{S}}^\dagger], \quad \Gamma_{\mathbf{D}} = i [\Sigma_{\mathbf{D}} - \Sigma_{\mathbf{D}}^\dagger] \quad (1.29)$$

where  $\Gamma_{\mathbf{S}}$  and  $\Gamma_{\mathbf{D}}$  are the  $N \times N$  broadening functions [29, 30]. By comparing Eqs. (1.29) to Eqs. (1.24) and (1.25), we can note that  $\gamma_{\mathbf{S}}$  and  $\gamma_{\mathbf{D}}$  represent the first and the last columns of the matrices  $\Gamma_{\mathbf{S}}$  and  $\Gamma_{\mathbf{D}}$ , respectively.

As can be seen in Eq. (1.27), the self-energy terms have two effects. First, they change the Hamiltonian from  $\mathbf{H}_0$  to  $\tilde{\mathbf{H}}_0$ , which in turn modifies the eigenstates and eigenenergies. Second, and more importantly,

they introduce an imaginary part to the energy determined by the broadening functions  $\Gamma_S$  and  $\Gamma_D$ :  $(\mathbf{H}_0 + \Sigma)$ , where  $\Sigma = \Sigma_S + \Sigma_D$ , is not Hermitian, since in general the self-energies are not Hermitians. As a result, the eigenenergies of  $(\mathbf{H}_0 + \Sigma)$  are complex and this leads to a broadening of the energy levels from delta functions into functions which could have a non-Lorentzian shape, since the imaginary part of the eigenenergies are in general energy dependent [29]. In particular, the eigenenergy of the  $n$ -th eigenstate can be expressed as:

$$\epsilon_n = \epsilon_{n0} - \Delta_n - i \left( \frac{\beta_n}{2} \right) \quad (1.30)$$

where  $\epsilon_{n0}$  is the eigenenergy of the isolate conductor described by  $\mathbf{H}_0$  [Eq. (1.8)]. The time-depending wavefunction of the  $n$ -th eigenlevel of  $(\mathbf{H}_0 + \Sigma)$  reads:

$$\Psi_n(x, t) = e^{-i\epsilon_n t/\hbar} \Psi_n(x, t=0) = e^{-i(\epsilon_{n0} - \Delta_n)t/\hbar} e^{-t\beta_n/(2\hbar)}. \quad (1.31)$$

According to Eq. (1.31),  $\Delta_n$  represents the shift in the energy due a modification of the dynamics of an electron inside the channel by the coupling with the leads, whereas  $\beta_n$  is related to the fact that an electron injected in the channel can eventually disappear through one of the leads going out to infinity [29]. In addition, since  $|\Psi_n(x, t)|^2$  represents the probability to find an electron in the position  $x$  at the time instant  $t$ , according to Eq. (1.31) the quantity  $\hbar/\beta_n$  represents the average time an electron remains in state  $n$  before it escapes out into the leads [29].

### 1.2.3 Computation of the Green Function

Solving Eq. (1.2) is equivalent to solve  $\mathbf{B}\mathbf{G} = \mathbf{I}$ , i.e.

$$\mathbf{G} = \mathbf{B}^{-1}, \quad (1.32)$$

where  $\mathbf{B} = E\mathbf{I} - \mathbf{H}_0 - \Sigma_S - \Sigma_D = E\mathbf{I} - \mathbf{H}_0 - \Sigma$  and  $\Sigma = \Sigma_S + \Sigma_D$ . The straightforward way is to calculate  $\mathbf{G}$  by directly inverting the matrix  $\mathbf{B}$  [Eq. (1.32)] for each energy grid point. From a computational point of view, this can be very expensive. Significant numerical savings can be obtained for systems where the form of  $\mathbf{B}$  is block-tridiagonal [33]. In this case  $\mathbf{G}$  can be computed by a recursive algorithm without inverting the large matrix  $\mathbf{B}$ . In addition, only the evaluation of the diagonal blocks of  $\mathbf{G}$  is required in order to finally compute the electron density of the system [33].

As a final remark, it can be shown that the expression of the Green's function in terms of the eigenstates of the Hamiltonian reads [34]:

$$\mathbf{G}(x, x', E) = \sum_n \frac{\Psi_n(x) \Phi_n^*(x')}{E - \epsilon_n}, \quad (1.33)$$

where  $\Psi_n$  is an eigenstate of the effective Hamiltonian  $(\mathbf{H}_0 + \mathbf{\Sigma})$ , whereas  $\Phi_n$  is an eigenstate of the effective Hamiltonian  $(\mathbf{H} + \mathbf{\Sigma}^\dagger)$ , where  $\{\Psi_n\}$  and  $\{\Phi_n\}$  form a bi-orthonormal set having the property

$$\int \Phi_n(x) \Psi_m^*(x) dx = \delta_{nm}, \quad (1.34)$$

and in general  $\Psi_n \neq \Phi_n$ , since the operator  $(\mathbf{H}_0 + \mathbf{\Sigma})$  is not Hermitian. Note also that, unlike the case of isolate channel, the coupling to the leads make the eigenenergies complex, so that there are no singularities of  $\mathbf{G}(x, x', E)$  for real value of the energy  $E$  [29].

#### 1.2.4 Carrier density and current

Once  $\mathbf{G}$  is computed, the spectral function  $\mathbf{A}$  can be calculated as [29]:

$$\mathbf{A} = i [\mathbf{G} - \mathbf{G}^\dagger]. \quad (1.35)$$

The spectral function plays the role of a generalized density of states inside the conductor accounting for the coupling to the leads. The reason will be clear in the following. In particular, by means of Eqs. (1.29) and (1.32), we can write:

$$\mathbf{G}^{-1} - [\mathbf{G}^\dagger]^{-1} = \mathbf{\Sigma}^\dagger - \mathbf{\Sigma} = i\mathbf{\Gamma}, \quad (1.36)$$

where  $\mathbf{\Gamma} = \mathbf{\Gamma}_S + \mathbf{\Gamma}_D$ .

If one multiplies Eq. (1.36) by  $\mathbf{G}$  from the left and by  $\mathbf{G}^\dagger$  from the right, the following result is obtained:

$$\mathbf{G}^\dagger - \mathbf{G} = i\mathbf{G}\mathbf{\Gamma}\mathbf{G}^\dagger = i^2 [\mathbf{G} - \mathbf{G}^\dagger] = i\mathbf{A}, \quad (1.37)$$

and thus:

$$\mathbf{A} = \mathbf{G}\mathbf{\Gamma}\mathbf{G}^\dagger. \quad (1.38)$$

By means of Eqs. (1.30) and (1.33), the spectral function can be also expressed as:

$$\mathbf{A}(x, x', E) = \sum_n \Psi_n(x) \Phi_n^*(x') \frac{\beta_n}{(E - \epsilon_{n0} + \Delta_n)^2 + \left(\frac{\beta_n}{2}\right)^2}, \quad (1.39)$$

The diagonal elements of the spectral function represents the local Density of States (DOS):

$$D(x, E) = \frac{1}{2\pi} \mathbf{A}(x, x, E). \quad (1.40)$$

This can be easily verified in the limit  $\beta_n \rightarrow 0$ , i.e. in the long-lived eigenstates limit. Indeed, by using Eq. (1.40) and (1.39), we obtain:

$$\begin{aligned} D(x, E) &= \sum_n \frac{1}{2\pi} \Psi_n(x) \Phi_n^*(x) \frac{\beta_n}{(E - \epsilon_{n0} + \Delta_n)^2 + \left(\frac{\beta_n}{2}\right)^2} \rightarrow \\ &\rightarrow \sum_n \delta(E - \epsilon_{n0} + \Delta_n) |\Psi_n(x)|^2 \end{aligned} \quad (1.41)$$

as  $\beta_n \rightarrow 0$ , which represents the expected form for the local DOS of long-lived eigenstate [29].

The total density of states is therefore given by the trace of the spectral function  $\mathbf{A}$ , i.e. by the integration of Eq. (1.40) over the channel:

$$\begin{aligned} D(E) &= \frac{1}{2\pi} \text{Tr} [\mathbf{A}(x, x, E)] = \frac{1}{2\pi} \int \mathbf{A}(x, x, E) dx \\ &= \sum_n \frac{1}{2\pi} \frac{\beta_n}{(E - \epsilon_{n0} + \Delta_n)^2 + \left(\frac{\beta_n}{2}\right)^2}, \end{aligned} \quad (1.42)$$

where we have exploited Eq. (1.34). In the long-lived eigenstates limit  $\beta_n \rightarrow 0$ , Eq. (1.42) reduces to:

$$D(E) = \sum_n \delta(E - \epsilon_{n0} + \Delta_n), \quad (1.43)$$

as we would expect.

Since electron states in the reservoirs are filled according to the Fermi statistics, the total charge density  $n(x)$  within the device is computed by accounting for states injected from both contacts, i.e. by integrating the local density of states of source and drain reservoirs ( $D_S(x, E)$  and  $D_D(x, E)$ , respectively) over energy  $E$ , weighted with the appropriate Fermi function  $f$ :

$$\begin{aligned} n(x) &= \sum_{\alpha=S,D} \left[ -e \int_{E_N}^{+\infty} D_\alpha(x, E) f(E - E_{F\alpha}) dE \right. \\ &\quad \left. + e \int_{-\infty}^{E_N} D_\alpha(x, E) [1 - f(E - E_{F\alpha})] dE \right], \end{aligned} \quad (1.44)$$



where  $e$  is the electron charge,  $E_N$  is the charge neutrality level and  $E_{FS}$  ( $E_{FD}$ ) is the Fermi level in the source (drain) contact.

In order to compute  $n(x)$  self-consistently, the NEGF transport equation (1.32) is solved self-consistently along with the Poisson equation, until convergence is reached. In particular, Eq. (1.32) is solved in order to obtain  $\mathbf{G}$  and thus the carrier density  $n(x)$ . Then the Poisson equation is solved in order to give a better evaluation of the potential. The iteration between the Poisson and the NEGF equations continues until the self-consistency is achieved. Finally, the source-to-drain current is computed by means of the two-terminal Landauer formula [35]:

$$I = \frac{2e}{h} \int \mathcal{T}(E) [f_S(E) - f_D(E)] , \quad (1.45)$$

where  $\mathcal{T}(E) = \text{Tr}(\mathbf{\Gamma}_S \mathbf{G} \mathbf{\Gamma}_D \mathbf{G}^\dagger)$  is the source-to-drain transmission function [29] and the factor 2 in Eq. (1.45) accounts for the spin degeneracy.

### 1.2.5 Quasi-one dimensional systems: Carbon Nanotubes

As a final remark, the method which we have presented in this section for a simply 1D system can be directly generalized to the case of quasi-1D system, such as those composed by CNTs [31, 32]. The first step is to identify a set of atomistic orbitals to describe the physics for carrier transport and then to represent the Hamiltonian matrix  $\mathbf{H}_0$  for the isolated channel in this basis. Generally, a tight-binding approximation accounting for one  $p_z$  orbital per carbon atom as the basis set is used. Therefore, the size of  $\mathbf{H}_0$  is the total number of carbon atoms  $N_C$  in the transistors channel.

It is found that  $\mathbf{H}_0$  is a tridiagonal matrix [31]. In particular, if  $n$  is the number of carbon atoms in each ring, the  $N_C \times N_C$  Hamiltonian matrix for the CNT channel  $\mathbf{H}_0$  is a block tridiagonal matrix with  $n \times n$  submatrix describing the coupling between carbon atoms within a ring or between neighbor rings. Since the self-energies  $\mathbf{\Sigma}_S$  and  $\mathbf{\Sigma}_D$  accounting for open-boundary conditions are sparse with only one diagonal nonzero block, also in this case the effective Hamiltonian  $(\mathbf{H}_0 + \mathbf{\Sigma})$  in the real space is tridiagonal. However, due to the huge dimension of the matrix  $\mathbf{H}$ , the real space approach can be computationally very expensive. Even by applying the recursive method, which is applicable to a tridiagonal matrix, the computational cost is  $O(n^2 \times N_R)$ , where  $N_R$  is the number of carbon rings ( $N_C = n \times N_R$ ) [31]. In order to relieve

---

the computational burden, a mode space approach can be needed. The size of the matrix  $(\mathbf{H}_0 + \mathbf{\Sigma})$  is changed to  $(MN_R) \times (MN_R)$ , where  $M$  is the number of modes contributing to transport. If  $M < n$ , then the size of the problem is reduced from  $(n \times N_R)$  to  $(M \times N_R)$ . Since the transformed Hamiltonian is also block-tridiagonal, the recursive algorithm for computing the Green's function  $\mathbf{G}$  can be applied. Details can be found in Ref. [31].

## Chapter 2

# Statistical theory of shot noise in the presence of electron-electron interaction

As quasi one-dimensional field-effect transistors (FETs), based for example on Carbon Nanotubes (CNTs) or Silicon NanoWires (SNWs), are increasingly investigated as a possible replacement for conventional planar FETs, it is important to achieve complete understanding of the properties of shot noise of one-dimensional conductors electrostatically controlled by a third (gate) electrode. Shot noise is particularly sensitive to carrier-carrier interaction, that in turn can be particularly significant in one-dimensional nanoscale conductors, where electrons are few and screening is limited [36].

Low frequency  $1/f$  noise in quasi one-dimensional conductors has been the subject of interest for several authors [37, 38, 39], whereas few experimental papers on shot noise have recently been published [40, 17].

Due to the small amount of mobile charge in nanoscale one-dimensional FETs, even in strong inversion, drain current fluctuations can heavily

affect device electrical behavior. Of course, noise is an unavoidable and undesirable feature of electron devices, and its effect must be minimized or kept within tolerable levels for the operation of electronic circuits. From a more fundamental point of view, it is also a rich source of information on electron-electron interaction, which cannot be obtained from DC or AC electrical characteristics.

The main sources of noise are injection from the contacts into the device region, through the random occupation of states around the Fermi energy at the contacts, and partial transmission of electrons through the conductor, which gives rise to the so called partition noise. The main types of interaction that have a clear effect on noise are Pauli exclusion, which reduces fluctuations of the rate of injected electrons by limiting the occupancy of injected states, and Coulomb repulsions among electrons, which is the cause of fluctuations of the potential in the device region, that often suppress, but sometimes enhance the effect of fluctuations in the rate of injected electrons.

The combined effect of Pauli exclusion and Coulomb repulsion on shot noise has been investigated in the case of ballistic double gate MOSFETs [41], in planar MOSFETs [42] and in resonant tunneling diodes [43, 44, 45]. There are still few attempts [16] to a complete quantitative understanding of shot noise in ballistic CNT- and SNW-FETs. Indeed, when addressing a resonant tunneling diode one can usually adopt an approach that exploits the fact that the two opaque barriers break the device in three loosely coupled regions (the two contacts and the well), among which transitions can be described by Fermi golden rule, as has been done in Refs. [43, 44, 45]. This is not possible in the case of a transistor, where coupling between the channel and the contacts is very good.

Another important issue is represented by the fact that the widely known Landauer-Büttiker's noise formula [46, 47], does not take into account the effect of Coulomb interaction on shot noise through potential fluctuations. Indeed, recent experiments on shot noise in CNT-based Fabry Perot interferometers [17] show that in some bias conditions many-body corrections might be needed to explain the observed noise suppression. Other experiments show that at low temperature suspended ropes of single-wall carbon nanotubes of length  $0.4\text{ }\mu\text{m}$  exhibit a significant suppression of current fluctuations by a factor smaller than  $1/100$  compared to full shot noise [40]. However, this experimental result is not supported by a convincing interpretation, since possible explanations extend from ballistic transport in a small number of tubes within a rope, to diffusive

transport in a substantial fraction of the CNTs.

In this chapter, we present an expression for the shot noise power spectral density of ballistic quasi-one dimensional channels based on a statistical approach relying on quantities obtained from Monte Carlo (MC) simulations of randomly injected electrons from the reservoirs. This expression, derived within the second quantization formalism, generalizes the Landauer-Büttiker's noise formula including the effects of Coulomb interaction, that is significant for a large class of devices, and in particular for one-dimensional conductors. In the last two sections we present the simulation methodology used to compute the noise power spectrum, based on the self-consistent solution of the 3D Poisson and Schrödinger equations, within the non-equilibrium Green's function (NEGF) formalism [48].

## 2.1 Generalization of the Landauer-Büttiker formula to include Coulomb repulsion

According to Milatz's theorem [49], the power spectral density of the noise current in the zero frequency limit can be written as  $S(0) = \lim_{\nu \rightarrow \infty} [2/\nu \cdot \text{var}(I)]$ , where  $\nu$  is the injection rate of a carrier from a contact and  $\text{var}(I)$  is the variance of the current. According to Ref.[50],  $\nu$  can be expressed as  $\nu = \Delta E/(2\pi\hbar)$  where  $\Delta E$  is the energy discretization step, i.e. the minimum energy separation between injected states. Indeed, the contribution to the current of a transverse mode in the energy interval  $\Delta E$  can be expressed in the zero temperature limit by the Landauer-Büttiker formula as  $\langle dI \rangle = e/(2\pi\hbar) \Delta E$ . On the other hand  $\langle dI \rangle = e\nu$ , from which  $\nu = \Delta E/(2\pi\hbar)$  derives. Finally, the power spectral density of shot noise at zero frequency can be expressed as:

$$S(0) = \lim_{\nu \rightarrow 0} \frac{2}{\nu} \text{var}(I) = \lim_{\Delta E \rightarrow 0} 4\pi\hbar \frac{\text{var}(I)}{\Delta E}. \quad (2.1)$$

The variance of the current can be derived by means of the second quantization formalism, which allows a concise treatment of the many-electron problem.

Let us consider a mesoscopic conductor connected to two reservoirs [source (S) and drain (D)], where electron states are populated according to their Fermi occupation factors (Fig. 2.1). For simplicity, we assume that the conductor is sufficiently short as to completely neglect inelastic scattering events. Thermalization occurs only in the reservoirs. At zero

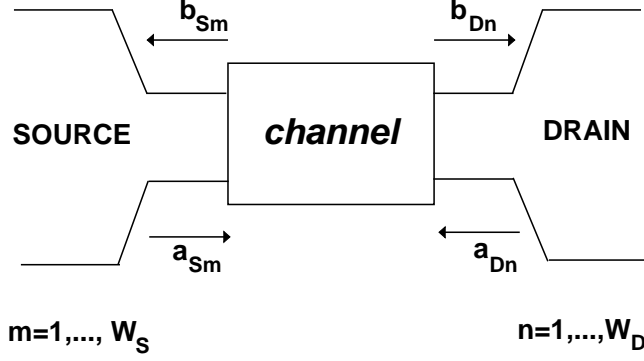


Figure 2.1: Annihilation operators for ingoing ( $a_{Sm}$ ,  $a_{Dn}$ ) and outgoing electron states ( $b_{Sm}$ ,  $b_{Dn}$ ) in a two terminal scattering problem ( $m = 1, \dots, W_S$ ;  $n = 1, \dots, W_D$ ).

magnetic field and far from the interacting channel, the time-dependent current operator at the source can be expressed as the difference between the occupation number of carriers moving inward ( $N_{Sm}^+$ ) and outward ( $N_{Sm}^-$ ) in each quantum channel  $m$  [46]:

$$I(t) = \frac{e}{h} \sum_{m \in S} \int dE [N_{Sm}^+(E, t) - N_{Sm}^-(E, t)] , \quad (2.2)$$

where

$$\begin{aligned} N_{Sm}^+(E, t) &= \int d(\hbar\omega) a_{Sm}^\dagger(E) a_{Sm}(E + \hbar\omega) e^{-i\omega t} , \\ N_{Sm}^-(E, t) &= \int d(\hbar\omega) b_{Sm}^\dagger(E) b_{Sm}(E + \hbar\omega) e^{-i\omega t} . \end{aligned} \quad (2.3)$$

The introduced operators  $a_{Sm}^\dagger(E)$  and  $a_{Sm}(E)$  create and annihilate, respectively, incident electrons in the source lead with total energy  $E$  in the channel  $m$  (Fig. 2.1). In the same way, the creation  $b_{Sm}^\dagger(E)$  and annihilation  $b_{Sm}(E)$  operators refer to electrons in the source contact for outgoing states. The channel index  $m$  runs over all the transverse modes and different spin orientations.

The operators  $a$  and  $b$  are related via an unitary transformation ( $n =$

$1, \dots, W_S)$  [46]:

$$b_{Sn}(E) = \sum_{m=1}^{W_S} \mathbf{r}_{nm}(E) a_{Sm}(E) + \sum_{m=1}^{W_D} \mathbf{t}'_{nm}(E) a_{Dm}(E), \quad (2.4)$$

where  $W_S$  and  $W_D$  represent the number of quantum channels in the source and drain leads, respectively, while the blocks  $\mathbf{r}$  (size  $W_S \times W_S$ ) and  $\mathbf{t}'$  (size  $W_S \times W_D$ ), describe electron reflection at the source ( $\mathbf{r}$ ) and transmission from drain to source ( $\mathbf{t}'$ ) and are included in the scattering matrix  $\mathbf{s}$  as [51]:

$$\mathbf{s} = \begin{pmatrix} \mathbf{r} & \mathbf{t}' \\ \mathbf{t} & \mathbf{r}' \end{pmatrix}. \quad (2.5)$$

The dimensions of  $\mathbf{s}$  are  $(W_S + W_D) \times (W_S + W_D)$ . Blocks  $\mathbf{t}$  and  $\mathbf{r}'$  in Eq. (2.5) are related to source-to-drain transmission and reflection back to the drain, respectively. In the following, time dependence will be neglected, since we are interested to the zero frequency case.

If we denote with  $|\sigma\rangle$  a many-particle (antisymmetrical) state, the occupation number in the reservoir  $\alpha$  in the channel  $m$  can be expressed as  $\sigma_{\alpha m}(E) = \langle a_{\alpha m}^\dagger(E) a_{\alpha m}(E) \rangle_\sigma$ . Pauli exclusion principle does not allow two electrons to occupy the same spin orbital, therefore  $\sigma_{\alpha m}(E)$  can be either 0 or 1. In addition, since fluctuations of the potential profile along the channel due to Coulomb interaction between randomly injected carriers affect the transmission of electrons, the scattering matrix elements have to depend on the occupation numbers of all states in both reservoirs:  $\mathbf{s}(E) = \mathbf{s}[\sigma_{S1}(E), \sigma_{S2}(E), \dots, \sigma_{D1}(E), \sigma_{D2}(E), \dots]$ . Let us stress the fact that, as pointed out in Ref. [46], whenever a finite channel is connected to semi-infinite leads, the channel can be considered as a small perturbation to the equilibrium regime of the contacts, and independent random statistics can be used for both reservoirs.

According to Ref. [46], current fluctuations can be evaluated by introducing an ensemble of many electrons states  $\{|\sigma_1\rangle, |\sigma_2\rangle, |\sigma_3\rangle, \dots, |\sigma_N\rangle\}$  and by weighting each state properly, i.e. by finding its statistical average, denoted by  $\langle \rangle_s$ . Each reservoir  $\alpha$  ( $\alpha = S, D$ ) is assumed to be at thermal equilibrium, so that its average occupancy can be described by the Fermi-Dirac statistics  $f_\alpha$ . As a consequence, the statistical average of  $\sigma_{\alpha m}(E)$  reads [46]:

$$\langle \sigma_{\alpha m}(E) \rangle_s = \langle \langle a_{\alpha m}^\dagger(E) a_{\alpha m}(E) \rangle_\sigma \rangle_s = f_\alpha(E). \quad (2.6)$$

Neglecting correlations between the occupation numbers of the same quantum channel at different energies, or between different channels at the same energy, we obtain [46]:

$$\langle \sigma_{\alpha m}(E) \sigma_{\beta n}(E') \rangle_s = f_{\alpha}(E) f_{\beta}(E') \quad (2.7)$$

for  $\alpha \neq \beta$  or  $m \neq n$  or  $E \neq E'$ . Including Eq. (2.6) in Eq. (2.7) and exploiting the relation  $\sigma_{\alpha m}(E)^2 = \sigma_{\alpha m}(E)$ , the average of the product of two occupation numbers can be expressed as:

$$\begin{aligned} \langle \sigma_{\alpha m}(E) \sigma_{\beta n}(E') \rangle_s &= f_{\alpha}(E) f_{\beta}(E') + \delta(E-E') \delta_{\alpha\beta} \delta_{mn} \\ &\quad [f_{\alpha}(E) - f_{\alpha}(E) f_{\beta}(E')] , \end{aligned} \quad (2.8)$$

where  $\delta(E-E')$ ,  $\delta_{\alpha\beta}$ ,  $\delta_{mn}$  are Kronecker delta functions.

In order to compute the average current along the channel and the power spectral density of the current fluctuations, we need to write the expectation values of the products of two and four operators [46]:

$$\langle a_{\alpha m}^{\dagger}(E) a_{\beta n}(E') \rangle_{\sigma} = \delta(E-E') \delta_{\alpha\beta} \delta_{mn} \sigma_{\alpha m}(E); \quad (2.9)$$

$$\begin{aligned} \langle a_{\alpha m}^{\dagger}(E) a_{\beta n}(E') a_{\gamma k}^{\dagger}(E'') a_{\delta l}(E''') \rangle_{\sigma} &= \\ \delta(E-E''') \delta(E'-E'') \delta_{\alpha\delta} \delta_{ml} \delta_{\beta\gamma} \delta_{nk} \sigma_{\alpha m}(E) [1 - \sigma_{\gamma k}(E'')] &+ \\ \delta(E-E') \delta(E''-E''') \delta_{\alpha\beta} \delta_{nm} \delta_{\gamma\delta} \delta_{kl} \sigma_{\alpha m}(E) \sigma_{\gamma k}(E'') & \end{aligned} \quad (2.10)$$

where the first contribution in Eq. (2.10) refers to exchange pairing ( $\alpha = \delta$ ,  $\beta = \gamma$ ,  $m = l$ ,  $n = k$ ), while the second to normal pairing ( $\alpha = \beta$ ,  $\gamma = \delta$ ,  $m = n$ ,  $k = l$ ) [46]. For the sake of simplicity, in the following we denote the expectation  $\langle \langle \rangle_{\sigma} \rangle_s$  as  $\langle \rangle$ .

By means of Eqs. (2.4) and (2.9) the average current reads:

$$\begin{aligned} \langle I \rangle &= \frac{e}{h} \int dE \left\{ \sum_{n \in S} \langle [\mathbf{t}^{\dagger} \mathbf{t}]_{nn} \sigma_{Sn} \rangle_s - \sum_{k \in D} \langle [\mathbf{t}'^{\dagger} \mathbf{t}']_{kk} \sigma_{Dk} \rangle_s \right\} \\ &= \frac{e}{h} \int dE \left\{ \sum_{n \in S} \langle [\tilde{\mathbf{t}}]_{S;nn} \sigma_{Sn} \rangle_s - \sum_{k \in D} \langle [\tilde{\mathbf{t}}]_{D;kk} \sigma_{Dk} \rangle_s \right\}, \end{aligned} \quad (2.11)$$

where  $[\tilde{\mathbf{t}}]_{\alpha;lp} \equiv [\mathbf{t}^{\dagger} \mathbf{t}]_{lp}$  if  $\alpha = S$  and  $[\mathbf{t}'^{\dagger} \mathbf{t}']_{lp}$  if  $\alpha = D$  ( $l, p \in \alpha$ ). The unitarity of the matrix  $\mathbf{s}$  has also been exploited, from which the relation  $\mathbf{r}^{\dagger} \mathbf{r} + \mathbf{t}^{\dagger} \mathbf{t} = \mathbf{1}$  follows. It is easy to show that for a non-interacting



channel, i.e. when occupancy of injected states does not affect transmission and reflection probabilities, Eq. (2.11) reduces to the two-terminal Landauer's formula [35]:

$$\langle I \rangle = \frac{e}{h} \int dE \text{Tr} [\mathbf{t}^\dagger \mathbf{t}] (f_S(E) - f_D(E)) , \quad (2.12)$$

where the relation  $\mathbf{s} = \mathbf{s}^\dagger$  has been exploited, so that  $\mathbf{t}' = \mathbf{t}^\dagger$  and  $\text{Tr} [\mathbf{t}'^\dagger \mathbf{t}'] = \text{Tr} [\mathbf{t}^\dagger \mathbf{t}]$ . In general, we can observe that for an interacting channel Eq. (2.11) provides a different result with respect to Landauer's formula, because fluctuation of transmission probabilities induced by random injection in the device, is responsible for rectification of the current. The effect is often very small, but not always [52]. However, it cannot be captured by Landauer's formula, as other many-particle processes affecting device transport properties [53, 54].

The mean squared current reads:

$$\begin{aligned} \langle I^2 \rangle &= \left( \frac{e}{h} \right)^2 \int dE \int dE' \sum_{m,n \in S} \{ \langle N_{Sm}^+(E) N_{Sn}^+(E') \rangle - \langle N_{Sm}^+(E) N_{Sn}^-(E') \rangle \\ &\quad - \langle N_{Sm}^-(E) N_{Sn}^+(E') \rangle + \langle N_{Sm}^-(E) N_{Sn}^-(E') \rangle \} \\ &= F_{++} + F_{+-} + F_{-+} + F_{--} . \end{aligned} \quad (2.13)$$

This expression consists of four terms, related to states at the source contacts, that can be evaluated by means of Eqs. (2.9) and (2.10): the first one ( $F_{++}$ ) represents the correlation of fluctuations in two ingoing streams, the second and the third ones ( $F_{+-}$ ,  $F_{-+}$ ) describe the correlations of the fluctuations of the ingoing and outgoing streams, the fourth one ( $F_{--}$ ) refers to two outgoing streams.

The first term  $F_{++}$  can be expressed as:

$$F_{++} = \left( \frac{e}{h} \right)^2 \int dE \int dE' \sum_{m,n \in S} \langle \sigma_{Sm}(E) \sigma_{Sn}(E') \rangle_s , \quad (2.14)$$

since  $\langle \sigma_{Sm}^2(E) \rangle_s = \langle \sigma_{Sm}(E) \rangle_s = f_S(E) \forall m \in S$ . Correlations between ingoing states are established through the statistical expectation values of each couple of occupancies of states injected from the source. The

second contribution  $F_{+-}$  reads:

$$F_{+-} = -\left(\frac{e}{h}\right)^2 \int dE \int dE' \left\{ \sum_{m,l \in S} \langle (1 - [\tilde{\mathbf{t}}(E')]_{S;ll}) \sigma_{Sm}(E) \sigma_{Sl}(E') \rangle_s \right. \\ \left. + \sum_{m \in S} \sum_{k \in D} \langle [\tilde{\mathbf{t}}(E')]_{D;kk} \sigma_{Sm}(E) \sigma_{Dk}(E') \rangle_s \right\}, \quad (2.15)$$

since  $\sigma_{\alpha l}^2(E) = \sigma_{\alpha l}(E) \forall l \in \alpha$  ( $\alpha = S, D$ ), due to the Pauli exclusion principle. In Eq. (2.15) correlations between ingoing and outgoing states are obtained by summing on each statistical average of the product of two occupation numbers of injected states, weighted with the reflection  $(1 - [\tilde{\mathbf{t}}(E')]_{S;ll} = [\mathbf{r}^\dagger \mathbf{r}(E')]_{ll})$  or transmission probability  $([\tilde{\mathbf{t}}(E')]_{D;kk})$  of outgoing channels.

By exploiting the anticommutation relations of the fermionic operators  $a$ , it is simple to demonstrate that the third term  $F_{-+}$  is identical to  $F_{+-}$ . Indeed:

$$\langle N_{Sm}^-(E) N_{Sn}^+(E') \rangle = \langle N_{Sn}^+(E') N_{Sm}^-(E) \rangle. \quad (2.16)$$

Finally, the fourth term  $F_{--}$  reads:

$$F_{--} = \left(\frac{e}{h}\right)^2 \Delta E \int dE \sum_{\alpha=S,D} \sum_{l \in \alpha} \langle [\tilde{\mathbf{t}}]_{\alpha;ll} (1 - [\tilde{\mathbf{t}}]_{\alpha;ll}) \sigma_{\alpha l} \rangle_s \\ - \left(\frac{e}{h}\right)^2 \Delta E \int dE \sum_{\alpha=S,D} \sum_{\substack{l,p \in \alpha \\ l \neq p}} \langle [\tilde{\mathbf{t}}]_{\alpha;lp} [\tilde{\mathbf{t}}]_{\alpha;pl} \sigma_{\alpha l} \sigma_{\alpha p} \rangle_s \\ - 2 \left(\frac{e}{h}\right)^2 \Delta E \int dE \sum_{k \in D} \sum_{p \in S} \langle [\mathbf{t}'^\dagger \mathbf{r}]_{kp} [\mathbf{r}^\dagger \mathbf{t}']_{pk} \sigma_{Dk} \sigma_{Sp} \rangle_s \\ + \left\langle \left[ \frac{e}{h} \int dE \left( \sum_{l \in S} [\tilde{\mathbf{t}}]_{S;ll} \sigma_{Sl} - \sum_{k \in D} [\tilde{\mathbf{t}}]_{D;kk} \sigma_{Dk} \right) \right]^2 \right\rangle_s \\ + 2 \left(\frac{e}{h}\right)^2 \int dE \int dE' \sum_{l \in S} \sum_{k \in D} \langle [\tilde{\mathbf{t}}(E')]_{D;kk} \sigma_{Sl}(E) \sigma_{Dk}(E') \rangle_s \\ - 2 \left(\frac{e}{h}\right)^2 \int dE \int dE' \sum_{l,p \in S} \langle [\tilde{\mathbf{t}}(E)]_{S;ll} \sigma_{Sl}(E) \sigma_{Sp}(E') \rangle_s \\ + \left(\frac{e}{h}\right)^2 \int dE \int dE' \sum_{l,p \in S} \langle \sigma_{Sl}(E) \sigma_{Sp}(E') \rangle_s. \quad (2.17)$$

Equation (2.17) contains all correlations between outgoing electron states in the source lead, where outgoing carriers at the source can be either reflected carriers incident from  $S$  or transmitted carriers injected from  $D$ . By means of the Eqs. (2.14), (2.15) and (2.17), we find the mean squared current:

$$\begin{aligned}
 \langle I^2 \rangle = & \left( \frac{e}{h} \right)^2 \Delta E \int dE \sum_{\alpha=S,D} \sum_{l \in \alpha} \langle [\tilde{\mathbf{t}}]_{\alpha;ll} (1 - [\tilde{\mathbf{t}}]_{\alpha;ll}) \sigma_{\alpha l} \rangle_s \\
 & - \left( \frac{e}{h} \right)^2 \Delta E \int dE \sum_{\alpha=S,D} \sum_{\substack{l,p \in \alpha \\ l \neq p}} \langle [\tilde{\mathbf{t}}]_{\alpha;lp} [\tilde{\mathbf{t}}]_{\alpha;pl} \sigma_{\alpha l} \sigma_{\alpha p} \rangle_s \\
 & - 2 \left( \frac{e}{h} \right)^2 \Delta E \int dE \sum_{k \in D} \sum_{p \in S} \langle [\mathbf{t}'^\dagger \mathbf{r}]_{kp} [\mathbf{r}^\dagger \mathbf{t}']_{pk} \sigma_{Dk} \sigma_{Sp} \rangle_s \\
 & + \left\langle \left[ \frac{e}{h} \int dE \left( \sum_{l \in S} [\tilde{\mathbf{t}}]_{S;ll} \sigma_{Sl} - \sum_{k \in D} [\tilde{\mathbf{t}}]_{D;kk} \sigma_{Dk} \right) \right]^2 \right\rangle_s.
 \end{aligned} \tag{2.18}$$

Finally, from Eqs. (2.1), (2.11) and (2.18) the noise power spectrum can be expressed as:

$$\begin{aligned}
 S(0) = & \left( \frac{e^2}{\pi h} \right) \int dE \sum_{\alpha=S,D} \sum_{l \in \alpha} \langle [\tilde{\mathbf{t}}]_{\alpha;ll} (1 - [\tilde{\mathbf{t}}]_{\alpha;ll}) \sigma_{\alpha l} \rangle_s \\
 & - \left( \frac{e^2}{\pi h} \right) \int dE \sum_{\alpha=S,D} \sum_{\substack{l,p \in \alpha \\ l \neq p}} \langle [\tilde{\mathbf{t}}]_{\alpha;lp} [\tilde{\mathbf{t}}]_{\alpha;pl} \sigma_{\alpha l} \sigma_{\alpha p} \rangle_s \\
 & - 2 \left( \frac{e^2}{\pi h} \right) \int dE \sum_{k \in D} \sum_{p \in S} \langle [\mathbf{t}'^\dagger \mathbf{r}]_{kp} [\mathbf{r}^\dagger \mathbf{t}']_{pk} \sigma_{Dk} \sigma_{Sp} \rangle_s \\
 & + \frac{4\pi\hbar}{\Delta E} \text{var} \left\{ \frac{e}{h} \int dE \left( \sum_{n \in S} [\tilde{\mathbf{t}}]_{S;nn} \sigma_{Sn} - \sum_{k \in D} [\tilde{\mathbf{t}}]_{D;kk} \sigma_{Dk} \right) \right\}.
 \end{aligned} \tag{2.19}$$

Equation (2.19) is the main theoretical result of this chapter: the power spectral density of the noise current is expressed in terms of transmission ( $\mathbf{t}$ ,  $\mathbf{t}'$ ), reflection ( $\mathbf{r}$ ) amplitude matrices, and properties of the leads, such

as random occupation numbers of injected states. Let us point out that, although our derivation starts from Eq. (2.2), which is valid only far from the mesoscopic interacting sample, Eq. (2.19) allows to take into account both Pauli and Coulomb interactions through the dependence of  $\mathbf{t}$ ,  $\mathbf{t}'$  and  $\mathbf{r}$  on actually injected states. Let us note that we go beyond the Hartree approximation by considering different random configuration of injected electron states for different many-particle systems [55, 52].

There is a crucial difference with respect to Landauer-Büttiker's formula, since Eq. (2.19) enables to consider fluctuations in time of the potential profile along the channel induced by the electrostatic repulsion between randomly injected electrons from the leads. Essentially, for each random configuration of injected states from both reservoirs, we consider a *snapshot* of device operation at a different time instant. All statistical properties — in the limit of zero frequency — can be obtained by considering a sufficient ensemble of snapshots.

Let us discuss some physical limits of interest. First, we consider the case of zero temperature. In such condition the Fermi factor for populating electron states in the reservoirs is either 0 or 1, and all snapshots are identical, so the fourth term in Eq. (2.19) disappears. In addition, we can remove the statistical averaging in Eq. (2.19) and the first three terms lead to the following expression of the noise power spectrum:

$$S(0) = \frac{2e^2}{\pi\hbar} \int_{E_{FD}}^{E_{FS}} dE \left( \text{Tr} [\mathbf{t}^\dagger \mathbf{t}] - \text{Tr} [\mathbf{t}^\dagger \mathbf{t} \mathbf{t}^\dagger \mathbf{t}] \right), \quad (2.20)$$

where  $E_{FS}$  and  $E_{FD}$  are the Fermi energies of the source and drain contacts, respectively. Such terms can be identified with partition noise (PN) contribution. More in detail, the first term of Eq. (2.19) is associated to the quantum uncertainty of whether an electron injected in the mode  $l$  from the reservoir  $\alpha$  is transmitted through or reflected by the barrier.

The second term of Eq. (2.19) contains instead ( $l \neq p$ ):

$$[\mathbf{t}^\dagger \mathbf{t}]_{lp} [\mathbf{t}^\dagger \mathbf{t}]_{pl} = \sum_{k,q \in D} \mathbf{t}_{kl}^* \mathbf{t}_{kp} \mathbf{t}_{qp}^* \mathbf{t}_{ql}. \quad (2.21)$$

Each term of the sum can be interpreted as the coupling between a transmission event from channel  $p \in S$  into channel  $k \in D$  and from channel  $l \in S$  into channel  $q \in D$ : such a coupling is due to time-reversed transmissions from  $k$  into  $l$  and from  $q$  into  $p$ .

In the same way, the third term of Eq. (2.19) contains

$$[\mathbf{t}'^\dagger \mathbf{r}]_{kp} [\mathbf{r}^\dagger \mathbf{t}']_{pk} = \sum_{l, n \in S} \mathbf{t}_{kl}^* \mathbf{r}_{lp} \mathbf{r}_{np}^* \mathbf{t}_{kn}, \quad (2.22)$$

that represents the coupling between carriers transmitted from  $n \in S$  into  $k \in D$  and reflected from  $p \in S$  into  $l \in S$ . The second and third terms provide insights on exchange effects. Indeed, in such terms, contributions with  $k \neq q$  and  $l \neq n$ , respectively, are complex and they represent exchange interference effects (fourth-order interference effects) in the many-particle wave-function due to the quantum-mechanical impossibility to distinguish identical carriers [50]. In the Results section, we will be concerned with identical reservoirs, i.e. identical injected modes from the contacts. In this case the diagonal terms of the partition noise (first term and part of the third term in Eq. (2.19)) will be referred as on-diagonal Partition Noise (PN ON), while the off-diagonal ones (second term and part of the third term in Eq. (2.19)) will be denoted as off-diagonal contribution to the partition noise (PN OFF).

Now let us assume that the number of quantum channel in the source is smaller than the one in the drain ( $W_S \leq W_D$ ) and let us consider the case of potential barrier wide with respect to the wavelength, so that one may neglect tunneling. In such a situation, the reflection amplitude matrix  $\mathbf{r}$  is equal to zero for energies larger than the barrier maximum  $E_C$ , whereas the transmission amplitude matrix is zero for energies smaller than  $E_C$ . By means of the unitarity of the scattering matrix  $\mathbf{s}$ , follows  $\mathbf{t}^\dagger \mathbf{t} = \mathbf{I}_S$  for  $E > E_C$ , where  $\mathbf{I}_S$  is the identity matrix of order  $W_S$ . Due to reversal time symmetry, there are  $W_S$  completely opened quantum channels in the drain contact and  $W_D - W_S$  completely closed. In this situation only the fourth term in Eq. (2.19) survives and the noise power spectral density becomes:

$$\begin{aligned} S(0) &= \frac{2e^2 W_S}{\pi \hbar} \int_{E_C}^{+\infty} dE [f_S(1-f_S) + f_D(1-f_D)] \\ &= \frac{2e^2 kT W_S}{\pi \hbar} [f_S(E_C) + f_D(E_C)]. \end{aligned} \quad (2.23)$$

When  $E_{FS} = E_{FD}$  such term obviously reduces to the thermal noise spectrum  $4kTG$ , where  $G = (e^2 W_S f_S(E_C))/(\pi \hbar)$  is the channel conductance at equilibrium. The fourth term in Eq. (2.19) can be therefore identified with the Injection Noise (IN) contribution.

Equation (2.19) describes correlations between transmitted states coming from the same reservoirs [second term in Eq. (2.19)] and between

transmitted and reflected states in the source lead (third term), with a contribution of opposite sign with respect to the first term. The negative sign derives from Eq. (2.10), in which exchange pairings include a minus sign due to the fermionic nature of electrons. Note that Eq. (2.19) can be expressed in a symmetric form with respect to an exchange between the source and the drain contacts. Indeed, by exploiting the unitarity of the scattering matrix, the third term becomes:

$$\begin{aligned} & - \left( \frac{e^2}{\pi\hbar} \right) \int dE \sum_{k \in D} \sum_{p \in S} \langle [\mathbf{t}'^\dagger \mathbf{r}]_{kp} [\mathbf{r}^\dagger \mathbf{t}']_{pk} \sigma_{Dk} \sigma_{Sp} \rangle_s \\ & - \left( \frac{e^2}{\pi\hbar} \right) \int dE \sum_{k \in D} \sum_{p \in S} \langle [\mathbf{r}'^\dagger \mathbf{t}]_{kp} [\mathbf{t}^\dagger \mathbf{r}']_{pk} \sigma_{Dk} \sigma_{Sp} \rangle_s, \end{aligned} \quad (2.24)$$

which establishes correlations between transmitted and reflected states in the source and drain leads.

Now let us consider the limit when transmission and reflection matrices do not depend on random occupation numbers of injected states, i.e. a non fluctuating potential profile is imposed along the channel. By exploiting the reversal time symmetry ( $\mathbf{s} = \mathbf{s}^\dagger$ , so that  $\mathbf{t}' = \mathbf{t}^\dagger$ ), the unitarity of the scattering matrix, Eq. (2.19) reduces to:

$$\begin{aligned} S(0) = & \frac{2e^2}{\pi\hbar} \left\{ \int dE \sum_{\alpha=S,D} (\text{Tr} [\mathbf{t}^\dagger \mathbf{t}] - \text{Tr} [\mathbf{t}^\dagger \mathbf{t} \mathbf{t}^\dagger \mathbf{t}] + T_\alpha) f_\alpha \right. \\ & - \int dE \sum_{\alpha=S,D} T_\alpha f_\alpha^2 \\ & - 2 \int dE (\text{Tr} [\mathbf{t}^\dagger \mathbf{t}] - \text{Tr} [\mathbf{t}^\dagger \mathbf{t} \mathbf{t}^\dagger \mathbf{t}]) f_S f_D \\ & \left. + \int dE \sum_{\alpha=S,D} (\text{Tr} [\mathbf{t}^\dagger \mathbf{t} \mathbf{t}^\dagger \mathbf{t}] - T_\alpha) [f_\alpha (1 - f_\alpha)] \right\}, \end{aligned} \quad (2.25)$$

where  $T_\alpha = \sum_{l \neq p \in \alpha} [\tilde{\mathbf{t}}]_{\alpha;lp} [\tilde{\mathbf{t}}]_{\alpha;pl}$  and the sum does not run on the spin. Equation (2.25) then reduces to:

$$\begin{aligned} S(0) = & \frac{2e^2}{\pi\hbar} \int dE \{ [f_S(1-f_S) + f_D(1-f_D)] \text{Tr} [\mathbf{t}^\dagger \mathbf{t} \mathbf{t}^\dagger \mathbf{t}] + \\ & [f_S(1-f_D) + f_D(1-f_S)] (\text{Tr} [\mathbf{t}^\dagger \mathbf{t}] - \text{Tr} [\mathbf{t}^\dagger \mathbf{t} \mathbf{t}^\dagger \mathbf{t}]) \}, \end{aligned} \quad (2.26)$$

which is the well-known *Landauer-Büttiker noise formula* [46]. Let us note that Eq. (2.20) can be recovered as well from Eq. (2.26). Indeed at zero temperature the stochastic injection vanishes since random statistics coincides to the Fermi factor. In the same way, Eq. (2.23) might be derived from Eq. (2.26), since in this case noise is only due to the thermionic emission contribution and fluctuations of the potential profile do not play any role in noise.

## 2.2 Computational methodology

In order to properly include the effect of Coulomb interaction, we self-consistently solve the 3D Poisson equation, coupled with the Schrödinger equation with open boundary conditions, within the NEGF formalism, which has been implemented in our in-house open source simulator *NanoTCAD ViDES* [56]. For what concerns the boundary conditions of Poisson equations, Dirichlet boundary conditions are imposed in correspondence of the metal gates, whereas null Neumann boundary conditions are applied on the ungated surfaces of the 3D simulation domain. In particular the 3D Poisson equation reads

$$\vec{\nabla} \cdot [\epsilon \vec{\nabla} \phi(\vec{r})] = -(\rho(\vec{r}) + \rho_{fix}(\vec{r})), \quad (2.27)$$

where  $\phi$  is the electrostatic potential,  $\rho_{fix}$  is the fixed charge which accounts for ionized impurities in the doped regions, and  $\rho$  is the charge density per unit volume

$$\begin{aligned} \rho(\vec{r}) = & -e \int_{E_i}^{+\infty} dE \sum_{\alpha=S,D} \sum_{n \in \alpha} DOS_{\alpha n}(\vec{r}, E) \sigma_{\alpha n}(E) \\ & + e \int_{-\infty}^{E_i} dE \sum_{\alpha=S,D} \sum_{n \in \alpha} DOS_{\alpha n}(\vec{r}, E) [1 - \sigma_{\alpha n}(E)], \end{aligned} \quad (2.28)$$

where  $E_i$  is the mid-gap potential,  $DOS_{\alpha n}(\vec{r}, E)$  is the local density of states associated to channel  $n$  injected from contact  $\alpha$  and  $\vec{r}$  is the 3D spatial coordinate.

From a computational point of view, modeling of the stochastic injection of electrons from the reservoirs has been performed by means of statistical simulations taking into account an ensemble of many electron states, i.e. an ensemble of random configurations of injected electron states, from both contacts [52, 55]. The whole procedure is sketched

in Fig. 2.2 in the form of a flow diagram. In particular, the whole energy range of integration (Eqs. (2.19) and (2.28)) has been uniformly discretized with energy step  $\Delta E$ . Then, in order to obtain a random injection configuration, a random number  $\mathfrak{R}$  uniformly distributed between 0 and 1 has been extracted for each electron state represented by energy  $E$ , reservoir  $\alpha$  and quantum channel  $n$  [57]. More in detail, the state is occupied if  $\mathfrak{R}$  is smaller than the Fermi-Dirac factor, i.e.  $\sigma_{Sn}(E)$  [ $\sigma_{Dn}(E)$ ] is 1 if  $\mathfrak{R} < f_S(E)$  [ $f_D(E)$ ], and 0 otherwise (Fig. 2.3).

The random injection configuration generated in this way has been then inserted in Eq. (2.28) and self-consistent solution of Eqs. (2.27) and (2.28) and the Schrödinger equations has been performed. Once convergence has been reached, the transmission ( $\mathbf{t}, \mathbf{t}'$ ) and reflection ( $\mathbf{r}$ ) matrices are computed. The procedure is repeated several times in order to gather data from a reasonable ensemble. In our case, we have verified that an ensemble of 500 random configurations represents a good trade-off between computational cost and accuracy. Finally, the power spectral density  $S(0)$  has been extracted by means of Eq. (2.19).

In the following, we will refer to self-consistent Monte Carlo simulations (SC-MC), when statistical simulations using the procedure described above, i.e. inserting random occupations  $\sigma_{Sn}(E)$  and  $\sigma_{Dn}(E)$  in Eq. (2.28), are performed. Instead we will refer to self-consistent (SC) simulations when the Poisson-Schrödinger equations are solved considering  $f_S$  and  $f_D$  in Eq. (2.28). SC-MC simulations of randomly injected electrons allow to consider both the effect of Pauli and Coulomb interaction on noise.

From a numerical point of view, particular attention has to be posed on the choice of the energy step  $\Delta E$ . As a test, we have verified that if we perform MC simulations, keeping the potential profile along the channel fixed and exploiting the one obtained by means of SC simulation, the noise power spectrum computed in this way reduces to the Landauer-Büttiker's limit, as already proved in an analytical way [Eq. (2.26)]: we refer to such simulations as non-self consistent Monte Carlo simulations (non SC-MC). In Fig. 2.4 the noise power spectrum computed by keeping fixed the potential profile along the channel and performing statistical non SC-MC simulations of randomly injected electrons is shown for four energy steps. As already proved in Eq. (2.25), the convergence to Landauer-Büttiker's limit is ensured for all the considered energy steps: as can be seen,  $\Delta E = 5 \times 10^{-4}$  eV provides faster convergence as compared to the other values with a relative error close to 0.16%.

Let us point out that the NEGF formalism computes directly the



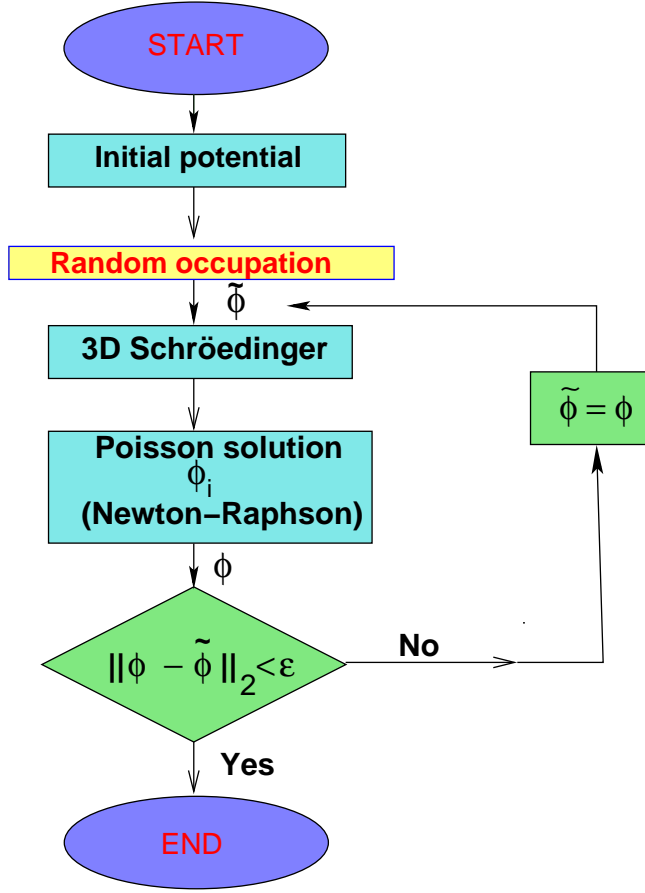


Figure 2.2: Flow diagram showing the procedure used in the statistical simulations. Starting from the self-consistent potential  $\tilde{\phi}$  achieved by modelling the occupancy in the reservoirs by means of the Fermi statistics, we extract random occupation numbers for all states in the source and drain contacts. Then the Schrödinger and Poisson equations are solved self-consistently until convergence of the potential  $\phi$  is reached, obtaining a sample to include in the ensemble, from which the noise power spectrum has been extracted by means of Eq. (2.19).

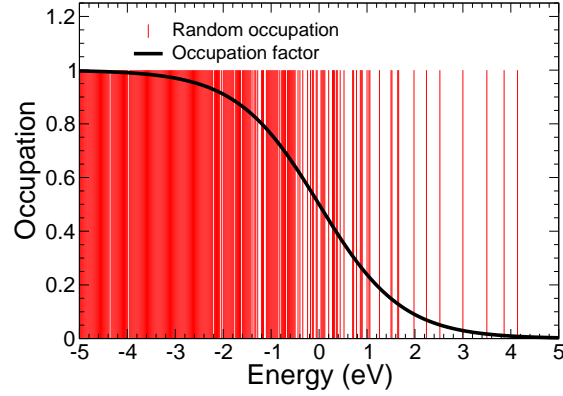


Figure 2.3: Random occupation compared to the occupation factor  $f(E)$ .

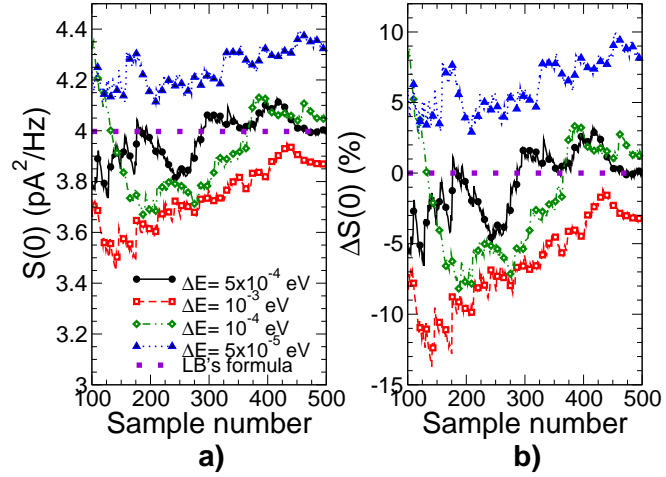


Figure 2.4: a) Noise power spectral density  $S(0)$  obtained from Eq. (2.19) for a given potential as a function of current sample number for four different energy steps. b) Relative deviation of  $S(0)$  with respect to Landauer-Büttiker's limit (2.26). The simulated structure is the SNW-FET shown in Fig. 3.1.

total Green's function  $\mathbf{G}$  of the channel and the broadening function of the source ( $\mathbf{\Gamma}_S$ ) and drain ( $\mathbf{\Gamma}_D$ ) leads, rather than the scattering matrix  $\mathbf{s}$ , that relates the outgoing waves amplitudes to the incoming waves amplitudes at different reservoirs. In order to obtain the matrix  $\mathbf{s}$ , we have exploited the *Fisher-Lee relation* [58], which expresses the elements of the  $\mathbf{s}$ -matrix in terms of the Green's function  $\mathbf{G}$  and transverse mode eigenfunctions (see Appendix B).

## 2.3 Concluding remarks

In this chapter we have described a novel and general approach to study shot noise in ballistic quasi one-dimensional CNT-FETs and SNW-FETs. By means of a statistical approach within the second quantization formalism, we have shown that the Landauer-Büttiker noise formula [Eq. (2.26)] can be generalized to include also Coulomb repulsion among electrons. This is possible via the dependence of the transmission and reflection matrices upon the actual occupation of injected states in the device, through the potential fluctuations in the device region. This point is crucial, since we will show in chapter 3 that by only using Landauer-Büttiker noise formula, i.e. by neglecting such dependence and therefore considering only Pauli exclusion principle, one can overestimate shot noise by as much as 180 %.

In the last section we have instead presented the methodology followed in order to quantitatively evaluate shot noise in CNT-FETs and SNW-FETs. In particular, Monte Carlo simulations are performed by self-consistently solving the electrostatics and the transport equations within the NEGF formalism, for a large ensemble of snapshots of device operation, each corresponding to a different configuration of the occupation of injected states.



## Chapter 3

# On the shot noise in quasi-1D FETs computed by means of Monte Carlo simulations

The progressive miniaturization of electron devices has led to a very limited number of carriers in the channel [36] down to few units. Signal-to-noise ratio can rapidly degrade, as noise power scales more slowly than signal power with size reduction, and can therefore be critical for nanoscale device operation. In the last decade, efforts have been addressed towards the investigation of electrical noise in nanoscale devices, focusing on diffusive mesoscopic conductors [59, 60, 61, 62, 63], nanoscale Metal-Oxide-Semiconductor Field-Effect Transistors (MOS-FETs) [42, 64, 65] and on carbon-based electronic devices [66, 17, 57, 52, 55].

When carriers are highly correlated, either sub- or super-poissonian noise can be observed. In particular, noise enhancement has been observed in resonant tunneling diodes [43, 44], due to the positive correlation between electrons tunneling into the quantum well caused by the

interplay between the density of states in the well and electrostatics.

In the first part of this chapter, by using the methodology based on statistical Monte Carlo simulations with states randomly injected from the contacts [52, 55] presented in chapter 2, a shot noise suppression is computed in (13,0) CNT-FETs and SNW-FETs [52, 55]. In particular, by comparing the noise power spectrum calculated by means of Monte Carlo simulations to that computed by means of the Landauer-Büttiker noise formula, i.e. considering only Pauli exclusion principle, a comprehensive understanding of the effect of Coulomb repulsion on noise emerges. The partition and the injection noise components are also calculated, as well as the importance of exchange interference noise contribution is highlighted [55, 67]. In addition, a comparison between shot noise and thermal noise is also performed and the effect of scaling of device length and oxide thickness on noise is predicted [52].

In the second part of this chapter, we instead predict a shot noise enhancement in (25,0) CNT-FETs [68, 69]. Unlike resonant tunneling diodes, the noise enhancement in (25,0) CNT-FETs is due to a different mechanism, i.e. the modulation of electron injection from the source due to the transfer of holes between the drain and the channel. The temperature and frequency ranges where the noise enhancement would be measurable are also investigated.

### 3.1 Simulated devices

The approach described in the previous chapter has been used to study the behavior of shot noise in quasi-1D channel of CNT-FETs and SNW-FETs with identical reservoirs (Fig. 3.1). We consider a (13,0) CNT embedded in SiO<sub>2</sub> with oxide thickness equal to 1 nm, an undoped channel of 10 nm and n-doped CNT extensions 10 nm long, with a molar fraction  $f = 5 \times 10^{-3}$ . The SNW-FET has an oxide thickness ( $t_{ox}$ ) equal to 1 nm and the channel length ( $L$ ) is 10 nm. The channel is undoped and the source and drain extensions (10 nm long) are doped with  $N_D = 10^{20} \text{ cm}^{-3}$ . The device cross section is  $4 \times 4 \text{ nm}^2$ . From a numerical point of view, a  $p_z$ -orbital tight-binding Hamiltonian has been assumed for CNTs [70, 71], whereas an effective mass approximation has been considered for SNWs [72, 73] by means of an adiabatic decoupling in a set of two-dimensional equations in the transversal plane and in a set of one-dimensional equations in the longitudinal direction for each 1D subband. For both devices, we have developed a quantum ballistic

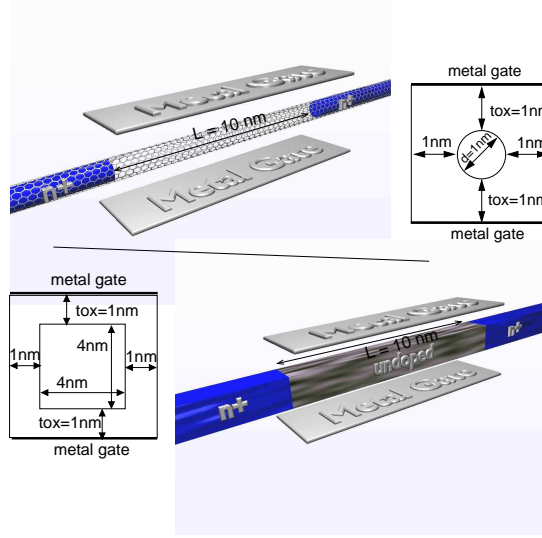


Figure 3.1: 3-D structures and transversal cross sections of the simulated CNT (top) and SNW-FETs (bottom).

transport model with semi-infinite extensions at their ends. A mode space approach has been adopted, since only the lowest subbands take part to transport. In particular, we have verified that four modes are enough to compute the mean current both in the ohmic and saturation regions. All calculations have been performed at room temperature ( $T = 300 \text{ K}$ ).

## 3.2 DC Characteristics

In Fig. 3.2, the transfer characteristics for different drain-to-source biases  $V_{DS}$  computed performing SC and SC-MC simulations are plotted as a function of the gate overdrive  $V_{GS} - V_{th}$  in the logarithmic scale, both for CNT and SNW devices. In particular the threshold voltage  $V_{th}$  for the CNT-FET at  $V_{DS} = 0.05 \text{ V}$  and  $0.5 \text{ V}$  is  $0.43 \text{ V}$ , whereas we obtain  $V_{th} = 0.13 \text{ V}$  for  $V_{DS} = 0.05 \text{ V}$  and  $0.5 \text{ V}$  for the SNW-FET. As can be noted, SC and SC-MC simulations give practically the same results for CNT-FET, except in the subthreshold region where an interesting rectifying effect of the statistics emerges in the Monte Carlo simulations

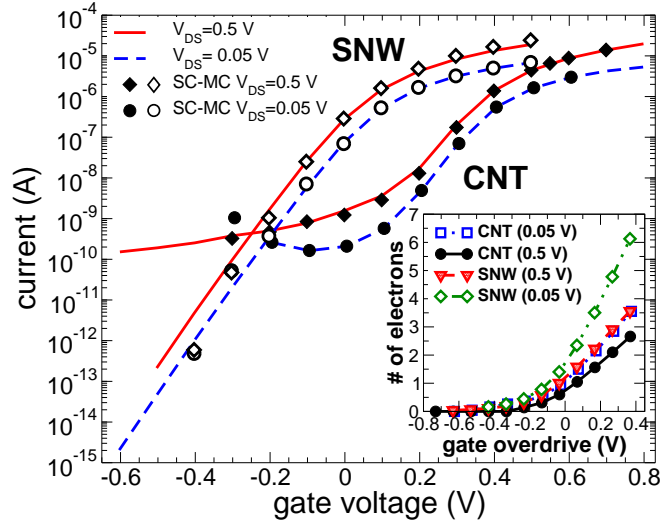


Figure 3.2: Transfer characteristics computed for  $V_{DS} = 0.5$  V and 0.05 V, obtained by SC-MC and SC simulations, for CNT and SNW-FET. Full dots refer to CNT, empty dots to SNW. Inset: average number of electrons in CNT-FETs and SNW-FETs channel, evaluated for  $V_{DS} = 0.5$  V and 0.05 V.

for a drain-to-source bias  $V_{DS} = 0.5$  V.

Instead, the rectifying effect is larger for SNW-FET, differences up to 30 % between the drain current  $\langle I \rangle$  computed by means of SC-MC and SC simulations can be also observed in the above threshold regime. In particular, for a gate voltage  $V_{GS} = 0.5$  V and a drain-to-source voltage  $V_{DS} = 0.5$  V, the drain current  $\langle I \rangle$  holds  $2.42 \times 10^{-5}$  A applying Eq. (2.11), and  $1.89 \times 10^{-5}$  A applying Landauer's formula (2.12). Current in the CNT-FET transfer characteristics increases for negative gate voltages due to the interband tunneling. Indeed, the larger the negative gate voltage, the higher the number of electrons that tunnel from bound states in the valence band to the drain, leaving positive charge in the channel, which eventually lowers the barrier and increases the off current [74].

In the inset of Fig. 3.2 the average number of electrons inside the channel of a CNT and SNW-FET for two different biases  $V_{DS} = 0.5$  V



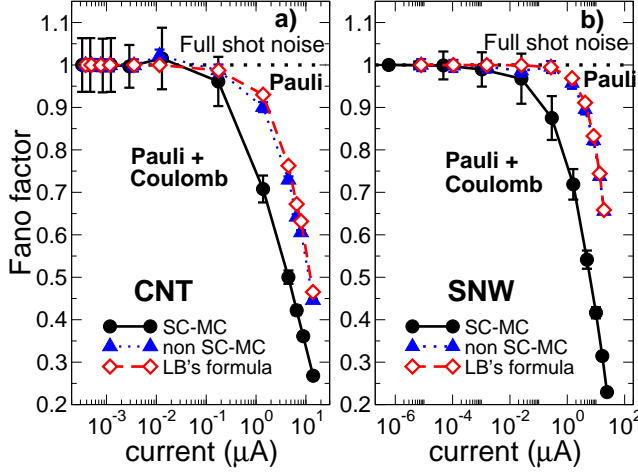


Figure 3.3: Fano factor as a function of the drain current  $\langle I \rangle$  for a) CNT- and b) SNW-FETs for  $V_{DS} = 0.5$  V. Solid line refers to the Fano factor  $F$  obtained by means of SC-MC simulations, dashed line (diamonds) applying Eq. (2.26) and dotted line (triangles) by means of non SC-MC simulations.

and 0.05 V is shown. As can be seen, only very few electrons contribute to transport at any give instant, which requires us to attently evaluate the sensitivity of such devices to charge fluctuations: the smaller the drain-to-source voltage, the larger the average number of electrons in the channel, since, for low  $V_{DS}$ , carriers are injected from both contacts.

### 3.3 Shot noise suppression in (13,0) CNT-FETs and SNW-FETs

Let us now focus our attention on the Fano factor  $F$ , defined as the ratio of the computed noise power spectral density  $S(0)$  and the full shot noise  $2e\langle I \rangle$ ,  $F = S(0)/(2e\langle I \rangle)$ . In Fig. 3.3, the Fano factor for both CNT-FETs and SNW-FETs is shown for  $V_{DS} = 0.5$  V as a function of drain-to-source current  $\langle I \rangle$ . Let us discuss separately the effects of Pauli exclusion alone and concurrent Pauli and Coulomb interactions. Triangles in Fig. 3.3 refer to  $F$  computed by means of non SC-MC simulations on  $10^4$  samples, while diamonds to results obtained by means

of Landauer-Büttiker's formula, applying Eq. (2.26). As expected the two approaches give the same results for both structures. Solid lines refer to  $S(0)$  computed by means of Eqs. (2.19) and (2.1) and SC-MC simulations, i.e. Pauli and Coulomb interactions simultaneously taken into account.

In the sub-threshold regime ( $\langle I \rangle < 10^{-9}$  A,  $V_{GS} - V_{th} < -0.2$  V), drain current noise is very close to the full shot noise, since electron-electron correlations are negligible due to the very small amount of mobile charge in the channel.

From the point of view of Eq. (2.26), for energies larger than the top of the barrier, we have  $f_D(E) \ll f_S(E) \ll 1$  and the integrand in Eq. (2.26) reduces to  $\text{Tr} [\mathbf{t}^\dagger \mathbf{t}(E)] f_S(E)$ . Instead, for energies smaller than the high potential profile along the channel,  $[\mathbf{t}^\dagger \mathbf{t}(E)]_{nm} \ll 1 \forall n, m \in S$ , so that we can neglect  $\text{Tr} [\mathbf{t}^\dagger \mathbf{t} \mathbf{t}^\dagger \mathbf{t}]$  in Eq. (2.26), with respect to  $\text{Tr} [\mathbf{t}^\dagger \mathbf{t}]$ . Since  $f_D(E) \ll f_S(E)$ , the integrand in Eq. (2.26) still reduces to  $\text{Tr} [\mathbf{t}^\dagger \mathbf{t}(E)] f_S(E)$ . The Fano factor then becomes

$$F = \frac{S(0)}{2e\langle I \rangle} \approx \frac{\frac{2e^2}{\pi\hbar} \int dE \text{Tr} [\mathbf{t}^\dagger \mathbf{t}(E)] f_S(E)}{2e \frac{e}{\pi\hbar} \int dE \text{Tr} [\mathbf{t}^\dagger \mathbf{t}(E)] f_S(E)} = 1 \quad (3.1)$$

In the strong inversion regime instead ( $\langle I \rangle > 10^{-6}$  A,  $V_{GS} - V_{th} > 0$  V), the noise is strongly suppressed with respect to the full shot value. In particular for a SNW-FET, at  $\langle I \rangle \approx 2.4 \times 10^{-5}$  A ( $V_{GS} - V_{th} \approx 0.4$  V), combined Pauli and Coulomb interactions suppress shot noise down to 22% of the full shot noise value, with a significant reduction with respect to the value predicted without including space charge effects as in Ref. [75], while for CNT-FET the Fano factor is equal to 0.27 at  $\langle I \rangle \approx 1.4 \times 10^{-5}$  A ( $V_{GS} - V_{th} \approx 0.3$  V). Indeed, an injected electron tends to increase the potential barrier along the channel, leading to a reduction of the space charge and to a suppression of charge fluctuation. Let us stress that an SC-MC simulation exploiting Eq. (2.19) is mandatory for a quantitative evaluation of noise. Indeed, by only considering Pauli exclusion principle through formula (2.26), one would have overestimated shot noise by 180 % for SNW-FET ( $\langle I \rangle \approx 2.4 \times 10^{-5}$  A,  $V_{GS} - V_{th} \approx 0.4$  V) and by 70 % for CNT-FET ( $\langle I \rangle \approx 1.4 \times 10^{-5}$  A,  $V_{GS} - V_{th} \approx 0.3$  V) [57, 52].

Now let us focus our attention on the partition PN (first three terms in Eq. (2.19)) and injection IN (fourth term in Eq. (2.19)) noise components of the Fano factor  $F$ . In Figs. 3.4 and 3.5 the contributions to  $F$  of PN and IN noises are shown, as a function of the gate overdrive  $V_{GS} - V_{th}$

for a drain-to-source bias  $V_{DS} = 0.5$  V for CNT-FETs and SNW-FETs, respectively: results have been obtained by means of SC-MC simulations. In particular, Figs. 3.4a and 3.5a refer to the on-diagonal contribution to the partition noise (open squares), to the injection noise (solid triangles up) and to the complete Fano factor (solid circles) obtained by means of Eq. (2.19), i.e. Pauli and Coulomb interactions simultaneously considered. We present also the Fano factor (open diamonds) computed by applying Eq. (2.26) on the self-consistent potential profile, i.e. when only Pauli exclusion principle is included. In Figs. 3.4b and 3.5b we show the contribution of the off-diagonal partition noise to  $F$ , which provides a measure of mode-mixing and of exchange interference effects [55, 67].

As shown in Fig. 3.4a, the dominant noise source in ballistic CNT-FETs is the on-diagonal partition noise and the noise due to the intrinsic thermal agitations of charge carriers in the contacts (injection noise), which is at most the 36 % of the partition noise ( $V_{GS} - V_{th} \approx -0.1$  V). Nearly identical results are shown for SNW-FETs, with the exception of a stronger contribution given by the injection noise, up to the 86 % of the on-diagonal partition term ( $V_{GS} - V_{th} \approx -0.2$  V). Moreover, the behavior of the two noise components, as a function of  $V_{GS} - V_{th}$ , is very similar for both CNT- and SNW-FETs:  $F$  tends to 1 in the subthreshold regime, while in strong inversion regime shot noise is strongly suppressed.

It is also interesting to observe that the off-diagonal contribution to partition noise, due to exchange correlations between transmitted states and between transmitted and reflected states, has a strong dependence on the height of the potential profile along the channel (variation of 5 orders of magnitude for CNT-FETs) and is negligible for quasi one-dimensional FETs. In particular, for CNT-FETs such term is at most 5 orders of magnitude smaller than the on-diagonal partition noise or injection noise in the strong inversion regime ( $V_{GS} - V_{th} \approx 0.3$  V), while in the subthreshold regime its magnitude still reduces (about  $10^{-11}$  for  $V_{GS} - V_{th} \approx -0.4$  V). For SNW-FETs we have obtained similar results: the off-diagonal partition noise is indeed at most 5 orders of magnitude smaller than the other two contributions.

In such conditions, transmission occurs only along separate quantum channels and an uncoupled mode approach is also accurate. Indeed, off-diagonal partition noise provides an interesting information on the strength of the mode-coupling which, as already seen, is very small. In particular, neglecting this term, results obtained from Eq. (2.19) can be recovered as well.

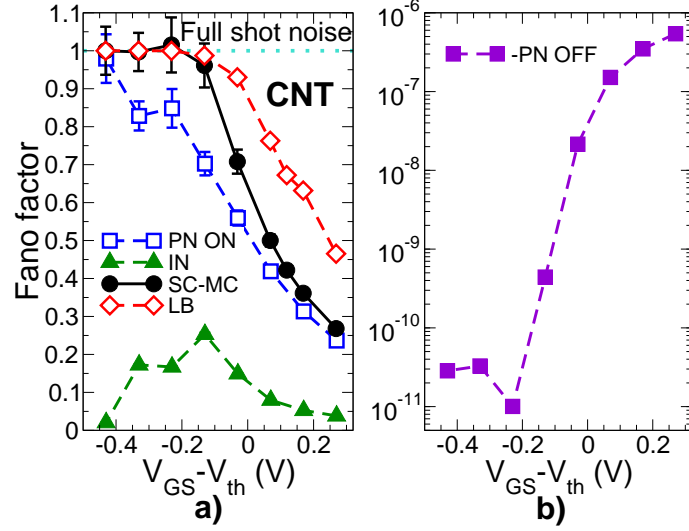


Figure 3.4: Contributions to the Fano factor in a CNT-FET of the on-diagonal and off-diagonal partition noise and of the injection noise (respectively on-diagonal and off-diagonal part of the first three terms, and fourth term in Eq. (2.19)) as a function of the gate overdrive  $V_{GS} - V_{th}$  for a drain-to-source bias  $V_{DS} = 0.5$  V. a) The on-diagonal partition (PN ON, open squares), the injection (IN, solid triangles up) and the full noise (solid circles) computed by means of SC-MC simulations are shown. The Fano factor computed by exploiting Landauer-Büttiker's formula (2.26) and SC simulations (open diamonds) is also shown. b) Off-diagonal partition noise contribution (PN OFF) to  $F$  due to correlation between transmitted states and between transmitted and reflected states.

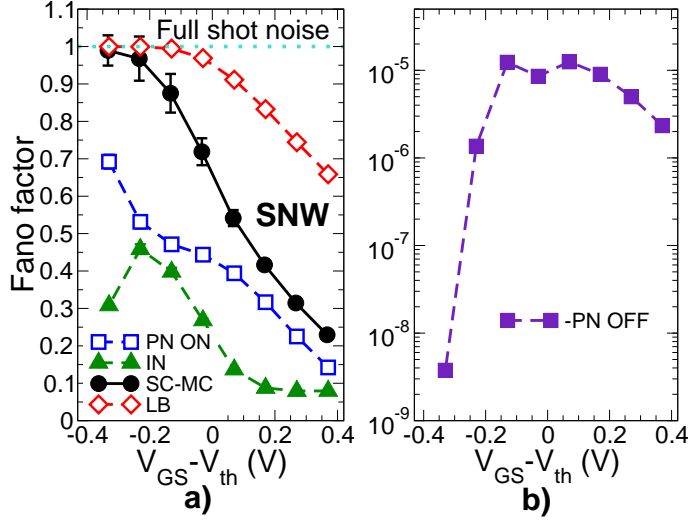


Figure 3.5: Contributions to the Fano factor in a SNW-FET of the on-diagonal and off-diagonal partition noise and of the injection noise, obtained for  $V_{DS} = 0.5$  V, as a function of the gate overdrive  $V_{GS} - V_{th}$  in a SNW-FET. In a) the on-diagonal partition, the injection and the full noise computed by means of SC-MC simulations (both Pauli and Coulomb interactions taken into account) are shown together with results obtained by means of Eq. (2.26). b) Off-diagonal partition noise due to correlation between transmitted states and between transmitted and reflected states.

### 3.3.1 On the importance of exchange interference effects on current fluctuations

In the previous discussion, carriers from different quantum channels do not interfere. However, since we deal with a many indistinguishable particle system, such effects can come into play. To this purpose, we investigate in more detail two examples in which exchange pairings, that include also exchange interference effects, give a non negligible contribution to drain current noise. In the past exchange interference effects have been already predicted for example in ballistic conductor with an elastic scattering center in the channel [76], in diffusive four-terminal conductors of arbitrary shape [77] and in quantum dot in the quantum Hall regime [78], connected to two leads via quantum point contacts.

In the first case we discuss, mode-mixing does not appear, i.e. the non-diagonal elements of the matrices  $\mathbf{t}^\dagger \mathbf{t}$  and  $\mathbf{t}^\dagger \mathbf{r}$  are negligible with respect to the diagonal ones. Since the off-diagonal partition noise is negligible and since in the third term in Eq. (2.19) only contributions with indices  $l = n = k = p$  survive, exchange interference effects do not contribute to electrical noise. We consider a CNT-FET at low bias condition:  $V_{DS} = 50$  mV. In Fig. 3.6a the on-diagonal partition noise, the injection noise and correlations due to the off-diagonal partition noise, evaluated performing statistical SC-MC simulations, are shown. In this case, on-diagonal correlations between transmitted and reflected states in the source lead (in the same quantum channel) extremely affect noise. Indeed, at the energies at which reflection events in the source lead are allowed, also electrons coming from D can be transmitted into the injecting contact S, since the corresponding energy states in D are occupied and the barrier height is small. Instead the exchange correlations represented by the off-diagonal partition noise are negligible, since they are at least 5 order of magnitude smaller than the other three terms in Eq. (2.19). Note that the noise enhancement obtained both in the inversion and subthreshold regimes is due to the fact that at low bias the current  $\langle I \rangle$  becomes small, while the noise power spectrum  $S(0)$  tends to a finite value, because of the thermal noise contribution.

Let now consider the situation in which modes are coupled and exchange interference effects, through the off-diagonal partition noise, contribute to drain current fluctuations. We consider the interesting case in which a vacancy, i.e. a missing carbon atom, is placed at the center of the channel of a (13,0) CNT-FET. From a numerical point of view, this defect can be modelled by introducing a strong repulsive po-

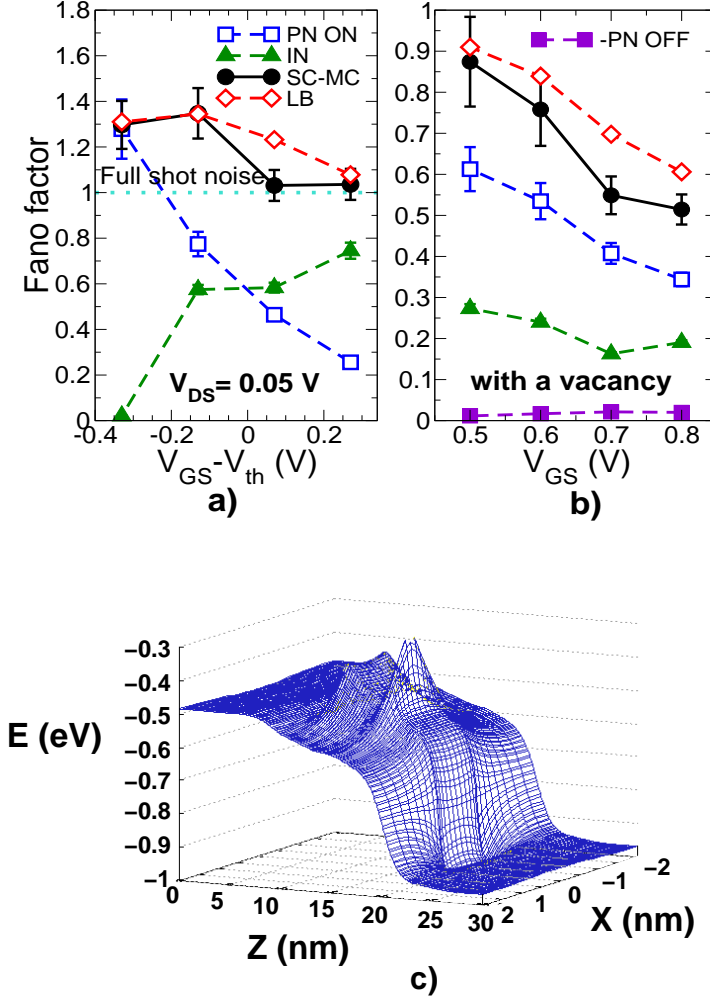


Figure 3.6: a): Contributions to the Fano factor  $F$  by the on-diagonal partition noise (open squares), and the injection noise (solid triangles up) as a function of the gate overdrive  $V_{GS} - V_{th}$ , for a drain-to-source bias  $V_{DS} = 50$  mV. The simulated device is a CNT-FET. The full noise computed by means of SC-MC simulations (solid circles, both Pauli and Coulomb interactions taken into account) and applying Eq. (2.26) (open diamonds, only Pauli exclusion considered) is also shown. b): Contributions to  $F$  by the on-diagonal and off-diagonal partition noise and by the injection noise (exploiting Eq. (2.19)) as a function of the gate overdrive for a CNT-FET with a vacancy in a site at the center of the channel. The drain-to-source bias is 0.5 V. c): Self-consistent midgap potential obtained by using the Fermi statistics for a gate voltage  $V_{GS} = 0.7$  V and a bias  $V_{DS} = 0.5$  V.  $Z$  is the transport direction along the channel,  $X$  is a transversal direction. The simulated device is the same of b).

tential (i.e. +8 eV, much larger than the energy gap of a (13,0) CNT:  $E_{gap} \approx 0.75$  eV) in correspondence of such site, thus acting as a barrier for transmission in the middle of the channel (Fig. 3.6c).

In Fig. 3.6b the three noise sources in Eq. (2.19) (on- and off-diagonal partition noise, injection noise) are plotted as a function of the gate voltage  $V_{GS}$  in the above threshold regime for  $V_{DS} = 0.5$  V, along with the full Fano factor computed performing SC and SC-MC simulations. Remarkably, in this case a mode space approach taking into account all modes (i.e. 13) is mandatory in order to reproduce all correlation effects on noise. As can be seen, off-diagonal exchange correlations gives rise to a not negligible correction to the Fano factor [55] ( $\approx 4$  % of the full Fano factor at  $V_{GS} = 0.8$  V). We observe that such correlations are only established between transmitted electrons states (second term in Eq. (2.19)), while correlations between reflected and transmitted electron states (third term in Eq. (2.19)) are negligible since almost all electrons injected from the receiving contact  $D$  are reflected back because of the high bias condition. In this chapter we have assumed phase-coherent quantum transport at room temperature. Our tools cannot include electron-phonon interaction, that a room temperature may play a role even in nanoscale devices. Ref. [79] has considered the effect of electron-phonon scattering and has neglected Coulomb interaction: they find that electron-phonon scattering increase shot noise in the above threshold regime, due to the broadening of the energy range of electron states contributing to transport.

### 3.3.2 Shot noise versus thermal channel noise

According to the classical approach for the formulation of drain current noise, channel noise is typically described in terms of a “modified” thermal noise, as  $S(0) = \gamma S_T$ , where  $S_T = 4K_B T g_{d0}$  is the thermal noise power spectrum at zero drain-to-source bias  $V_{DS}$ ,  $k_B$  is the Boltzmann constant,  $\gamma$  is a correction parameter and  $g_{d0} = (\partial \langle I \rangle / \partial V_{DS})_{V_{DS}=0}$  is the source-to-drain conductance at zero  $V_{DS}$ .

Although the classical formulation accurately predicts drain current noise in long channel MOSFETs, where  $\gamma$  is equal to 1 in the ohmic region and 2/3 in saturation [49], it underestimates noise in short channel devices. In particular, experimental evidences [80] of an excess noise in short channel MOSFET have been explained in terms of the limited number of scattering events inside the channel which is ineffective in suppressing the non-equilibrium noise component [81], or in terms of a



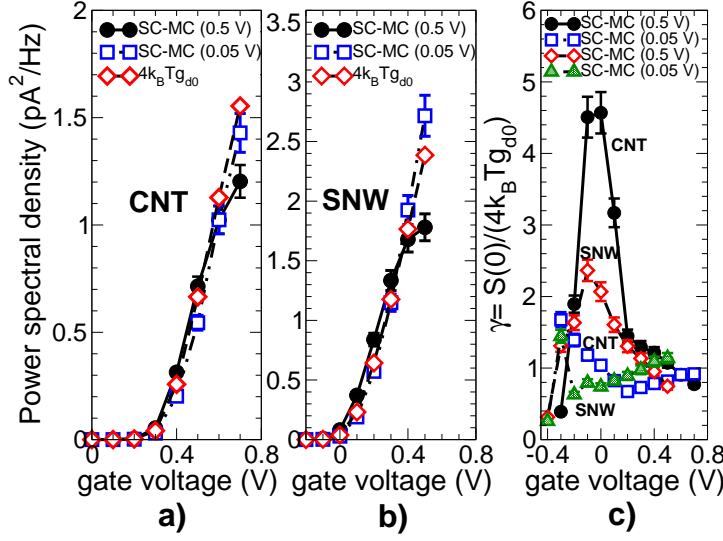


Figure 3.7: (a) noise power spectral density obtained by SC-MC simulations and thermal noise spectral density as functions of the gate voltage for a) CNT-FETs and b) SNW-FETs: the considered drain-to-source biases ( $V_{DS} = 0.5$  V, 0.05 V) are shown in brackets; c) ratio between the noise power obtained by SC-MC simulations and the thermal noise density as a function of the gate voltage.  $g_{d0}$  is the conductance evaluated for  $V_{DS} = 0$  V:  $g_{d0} = \left( \frac{\partial \langle I \rangle}{\partial V_{DS}} \right)_{V_{DS}=0}$ .

revised classical formulation by considering short channel effects, such as the carrier heating effect above the lattice temperature [82].

Actually, it can clearly be seen that non equilibrium transport easily provides  $\gamma > 1$  and that the cause of  $\gamma > 1$  is simply due to the fact that channel noise can be more properly interpreted as shot noise. For example, in the particular case of ballistic transport considered here, we can plot  $\gamma$  as  $S(0)/S_T$  as a function of the gate voltage in Fig. 3.7c. As can be seen, values of  $\gamma$  larger than 1 can be easily observed in weak and strong inversion. The strange behavior of  $\gamma$  as a function of the gate voltage is simply due to the fact that one uses an inadequate model (thermal noise) corrected with the  $\gamma$  parameter to describe a qualitatively different type of noise, i.e. shot noise.

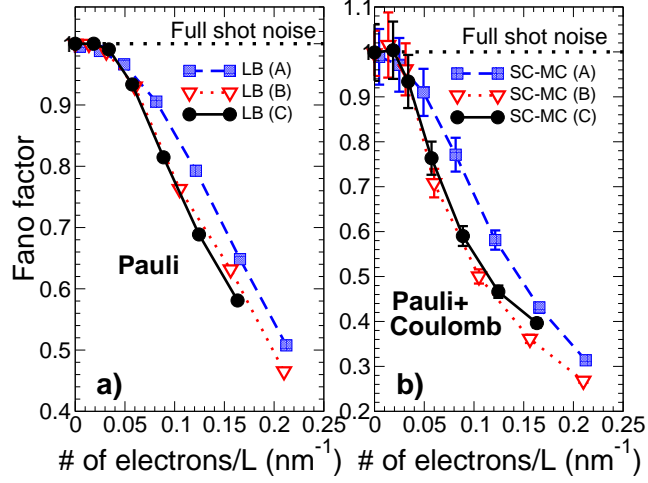


Figure 3.8: Fano factor as a function of the average number of electrons inside the channel per unit length for three different (13,0) CNT-FETs: (A)  $t_{ox}=1$  nm,  $L=6$  nm, (B)  $t_{ox}=1$  nm,  $L=10$  nm and (C)  $t_{ox}=2$  nm,  $L=10$  nm. In a) only the effect of the Pauli principle is shown [Eq. (2.26)]; in b) the effect of both Pauli and Coulomb interactions is considered. The drain-to-source bias  $V_{DS}$  is 0.5 V.

### 3.3.3 Effect of scaling on noise

Let us now discuss the effect of scaling on noise, focusing our attention on a (13,0) CNT-FET. One would expect that an increase of the oxide thickness would reduce the screening induced by the metallic gate, so that the Coulomb interaction would be expected to produce a larger noise suppression. For example, in the limit of a multimode ballistic conductor without a gate contact, significantly suppression of about two order of magnitude with respect to the full shot value has been shown by Bulashenko et al [16].

However, Ref. [16] exploits a semiclassical approach assuming a large number of modes and the conservation of transversal momentum, i.e. the role of the transversal electric field induced by the gate voltage is completely neglected. In our case only four modes contribute to transport, while the top and bottom gates of the simulated devices partially screen the electrostatic repulsion induced by the space charge in the channel on each injected electron, so that a smaller noise suppression than the one

achieved in Ref. [16] can be expected.

The Fano factor as a function of the average number of electrons inside the channel for unit length, computed by means of SC simulation and applying Eq. (2.26), for three CNTs with different oxide thickness  $t_{ox}$  and channel length  $L$  is shown in Fig. 3.8a: it shows results for CNT with  $t_{ox}=1$  nm,  $L=6$  nm (A), CNT with  $t_{ox}=1$  nm,  $L=10$  nm (B), and CNT with  $t_{ox}=2$  nm,  $L=10$  nm (C). Fig. 3.8b shows the Fano factor computed by performing SC-MC simulations and applying Eqs. (2.19) and (2.1). As can be seen, if the Fano factor is plotted as a function of the number of electrons per unit length, as in Fig. 3.8, curves are very close to one another, and effects of scaling are predictable.

### 3.4 Enhanced shot noise in CNT-FETs

A  $p_z$ -orbital tight-binding Hamiltonian has been adopted, considering four transversal modes [70]. All simulations have been performed at room temperature, self-consistently solving the 3D Poisson and Schrödinger equations within the Non-Equilibrium Green's Functions (NEGF) formalism by means of our open-source simulator NanoTCAD ViDES [56] and considering almost 1000 statistical configurations of incoming states of the many-particle system. In order to evaluate the zero-frequency noise power spectrum  $S(0)$ , we have exploited the statistical approach derived in Refs. [52, 55] and presented in Chapter II, that extends Landauer-Buttiker's approach by including the effect of Coulomb interaction.

Noise current power spectral density at zero frequency  $S(0)$  can be expressed as  $S(0) = S_{PN}(0) + S_{IN}(0)$ , where  $S_{PN}$  and  $S_{IN}$  represent the partition and the injection noise contributions, respectively.

A measure of correlation between charge carriers is the so-called Fano factor  $F \equiv S(0)/(2eI) \equiv F_{PN} + F_{IN}$ , where the term  $2eI$  corresponds to the full shot noise spectrum, whereas  $F_{PN} \equiv S_{PN}(0)/(2eI)$  and  $F_{IN} = S_{IN}(0)/2eI$ .

By neglecting the effect on noise of Coulomb interaction among electrons, and in particular the dependence of the transmission and reflection matrices upon the actual occupation of injected states in the device [52, 55],  $S(0)$  reduces to the result from Landauer [47] and Büttiker [46]  $S_{LB}(0)$ , that only includes the correlation among charge carriers due to their fermionic nature (Pauli exclusion principle). In a similar way, we introduce  $F_{LB} \equiv S_{LB}(0)/(2eI)$ .

The considered device is a double gate CNT-FET (Fig. 3.9a): the nanotube is a 2 nm diameter zig-zag (25,0) CNT with a band gap  $E_g = 0.39$  eV. The oxide thickness is 1 nm, the channel is undoped and has a length  $L_C$  of 10 nm. Source (S) and Drain (D) extensions are 10 nm long and doped with a molar fraction  $f = 5 \times 10^{-3}$ . For comparison purposes, we also consider a (13,0) CNT-FET ( $E_g = 0.75$  eV) with the same device geometry and doping profile [52, 55]. In Fig. 3.9b the tunneling current component and the total current are reported as a function of the gate overdrive  $V_{GS} - V_{th}$  for a (25,0) CNT-FET ( $V_{th} = 0.36$  V). As can be observed, the tunneling component is at least two orders of magnitude smaller than the total current, which therefore is almost equal to the thermionic component.

The Fano factors for a (25,0) and a (13,0) zig-zag CNT are plotted as a function of gate overdrive in Figs. 3.10a-b. Noise enhancement occurs only in the case of the (25,0) CNT ( $F > 1$ ) [68, 69]. If one neglects Coulomb interaction among carriers, the Fano factor ( $F_{LB}$ ) is smaller than one. *The whole shaded area in Fig. 3.10a indicates the shot noise enhancement due to the Coulomb interaction.*

For (13,0) CNTs, instead, Coulomb interaction suppresses noise below the value predicted by only including Pauli exclusion, as already observed in Refs. [52, 55]. The different behavior is strictly associated to the different amplitude of the injection noise ( $F_{IN}$  in Fig. 1), that is much larger for (25,0) CNTs. For both CNTs, in the deep sub-threshold regime, full shot noise is obtained, since carriers are so scarce in the channel that correlations are irrelevant.

Shot noise enhancement in the (25,0) CNT-FET can be explained with the help of Fig. 3.11 [68, 69].  $E_C$  and  $E_V$  are the conduction and valence band edge profiles in the channel, respectively, whereas  $E_{CS}$  ( $E_{CD}$ ) is the conduction band edge at the source (drain), and  $E_{BS}$  is the energy level of the quasi-bound state in the valence band. When the drain Fermi level  $E_{FD}$  roughly aligns with  $E_{BS}$ , holes in the conduction band in correspondence of the drain can tunnel into the bound state shifting downwards  $E_C$  in the channel by  $-e^2/(C_T L_C)$ , where  $C_T$  is the total geometrical capacitance of the channel per unit length. As a result, thermionic electrons injected from the source can more easily overcome the barrier. Instead, when a hole leaves the bound state, the barrier increases by the same amount, reducing thermionic injection. The noise enhancement is fully due to current modulation due to trapping/detrapping of holes in the bound state.

Since (13,0) CNTs have a much wider gap ( $E_g = 0.75$  eV),  $E_V$  in

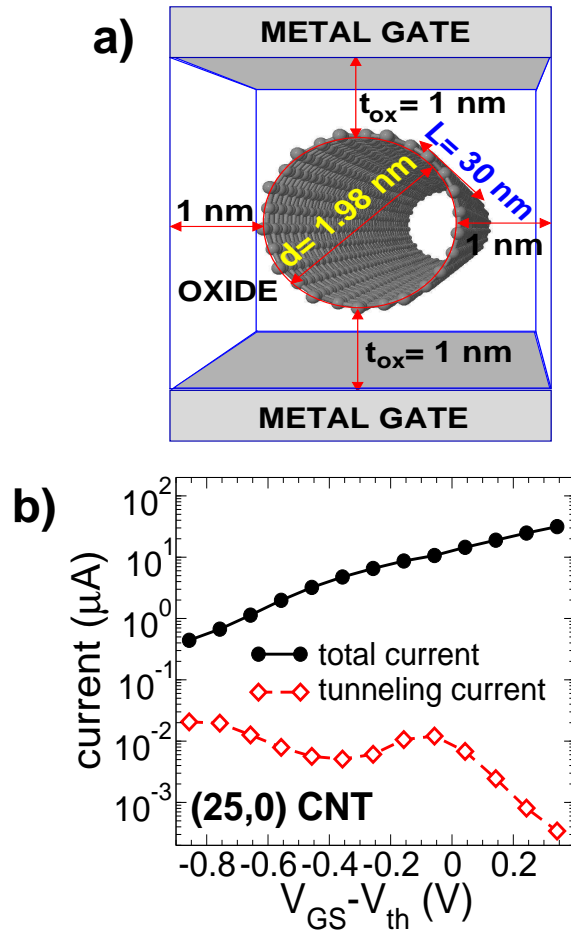


Figure 3.9: (a) Sketch of the simulated (25,0) double gate CNT Field Effect Transistor. (b) Transfer characteristics and tunneling current for (25,0) CNT-FETs.

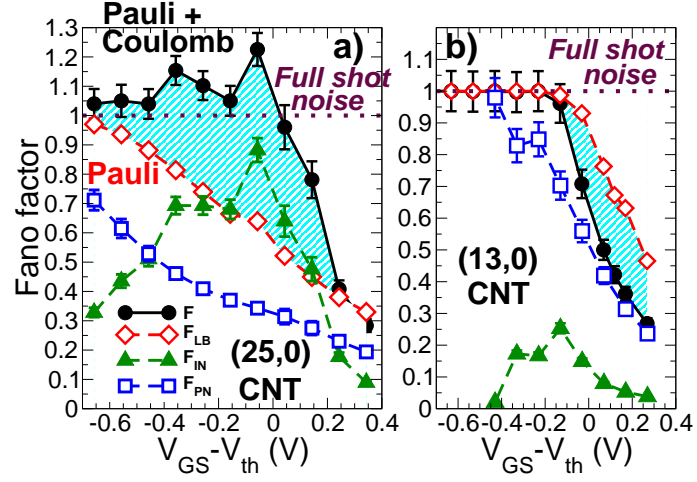


Figure 3.10: Fano factor as a function of the gate overdrive for a) (25,0) and b) (13,0) CNT-FETs for  $V_{DS} = 0.5$  V. The different contributions  $F_{LB}$ ,  $F_{IN}$ ,  $F_{PN}$  and the total Fano factor  $F$  are shown.

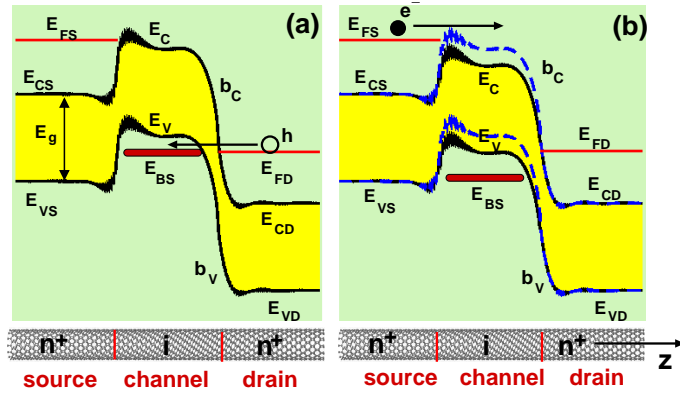


Figure 3.11: If an excess hole tunnels from the drain into a bound state in the intrinsic channel (a), the conduction band  $b_C$  and valence band  $b_V$  edge profiles are shifted downwards and more thermionic electrons can be injected in the channel, enhancing current fluctuations (b).

the channel is always below  $E_{CD}$  in the drain, and hole injection is completely inhibited, as well as noise enhancement.

The effect just illustrated resembles generation-recombination noise in semiconductors [83], since bound states in the valence band act like traps. Three remarkable differences can however be found: (i) the channel in this case is defect-free, and the trap-like behavior depends on the particular bias condition; (ii) the generation-recombination process in this case is associated to a spatial movement of charge (drain-channel) and is therefore similar to what observed in Refs. [64, 65] for MOS capacitors; (iii) in classical generation-recombination noise current fluctuations are due to fluctuations of the number of charge carriers, whereas here transport is elastic and current fluctuations are due to fluctuations in the occupation of injected states for electrons and holes and to the induced fluctuations of the potential barrier.

To justify our assertion, let us focus on the local density of states (LDOS) computed for the (25,0) CNT. In Figs. 3.12a-b the LDOS averaged on each carbon ring is shown as a function of the coordinate along the transport direction  $z$  for two gate voltages in correspondence of the peaks in Fig. 3.10a, i.e.  $V_{GS} = 0$  V and 0.3 V, and a drain-to-source bias  $V_{DS} = 0.5$  V: two localized states appear in the valence band, due to the local confinement. Since the energy of the highest quasi-bound state is close to the drain Fermi energy, hole tunneling in and out of the channel can occur, with a zero net current flow. As shown in Fig. 3.10a, shot noise enhancement ( $F = 1.22$ ) is observed whenever the applied gate voltage roughly aligns  $E_{BS}$  with  $E_{FD}$ , i.e. in the range  $-0.4$  V  $< V_{GS} - V_{th} < 0.1$  V.

In Figs. 3.13 and 3.14, we show the scatter plots obtained from Monte Carlo simulations. In particular, Figs. 3.13a-b show  $E_C$  as a function of the number of injected thermionic electrons for  $V_{DS} = 0.5$  V and  $V_{GS} = 0.7$  V for (13,0) CNTs ( $F = 0.27$ ) and 0 V for (25,0) CNTs ( $F = 1.15$ ). As can be noted in Fig. 3.13a, the net result of an electron entering the channel of the (25,0) CNT is a decrease of the conduction band in the channel, that is at first counterintuitive, and opposite to the trend observed in (13,0) CNTs [52, 55] (Fig. 3.13b). The different behavior is not due to a different screening of the gate field, since the quantum capacitance in the channel  $e \partial Q_{tot} / \partial E_C$  ( $Q_{tot}$  is the net charge in the channel) is expected to be positive in both cases (Figs. 3.14a-b). However, it is fully consistent with the interpretation proposed above for the noise enhancement in (25,0) CNT. Actually, the apparently strange behavior of Fig. 3.13a is due to the positive correlation between holes in the

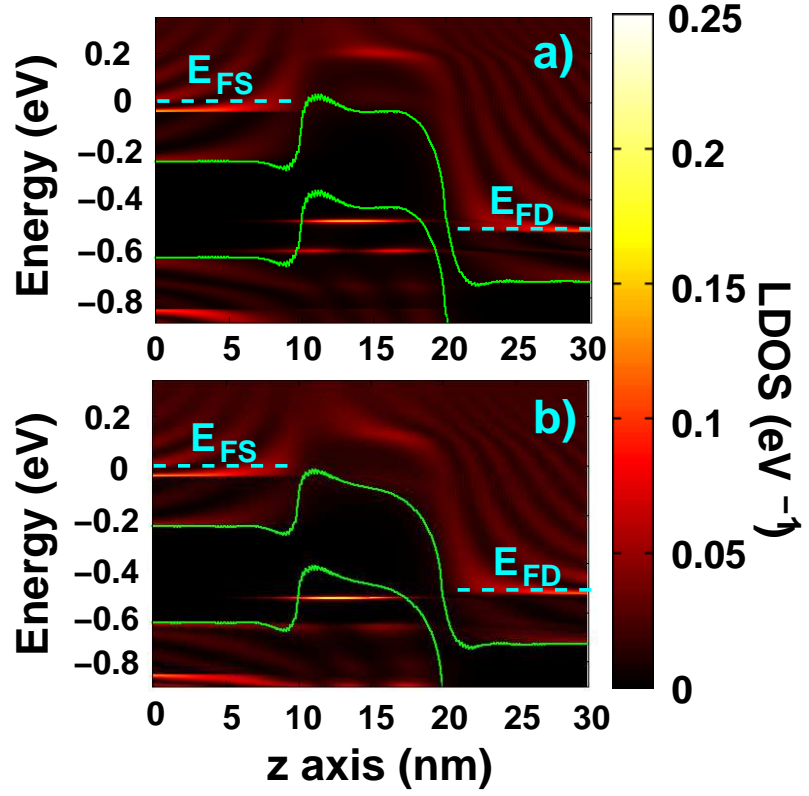


Figure 3.12: Local density of states [LDOS ( $\text{eV}^{-1}$ )] as a function of the longitudinal direction  $z$  for two different  $V_{GS}$ : 0 V (a) and 0.3 V (b). The bias  $V_{DS}$  is 0.5 V. Conduction band maximum  $E_C$  as a function of the number of electrons transmitted in the channel for (a) (25,0) and (b) (13,0) CNTs.



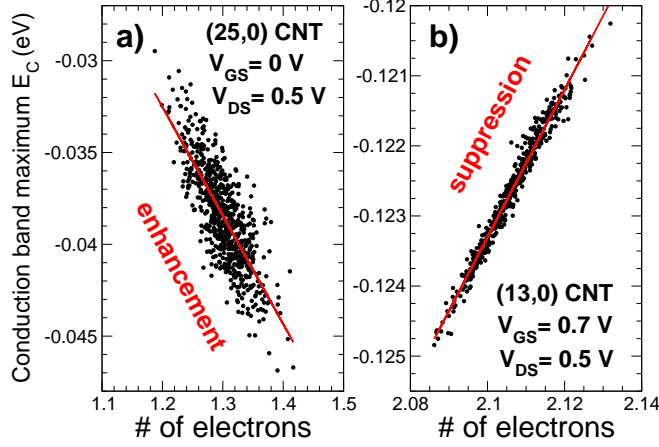


Figure 3.13: Conduction band maximum  $E_C$  as a function of the number of electrons transmitted in the channel for (a) (25,0) and (b) (13,0) CNTs.

quasi-bound state and thermionic electrons. This is further confirmed by Fig. 3.14c, which highlights a strong correlation between statistical fluctuations of holes and electrons in the channel, as proved by the almost unity correlation factor ( $R = 0.96$ ). In addition the slope of the line is close to 0.5, which means that for every two holes that are injected in the channel, electron count in the channel roughly increases by one.

To highlight the correlation between electrons and holes we can divide the states injected from the reservoirs in 4 regions: regions I ( $E > E_{CS}$ ) and II ( $E \leq E_{CS}$ ) refer to source injected states, whereas regions III ( $E > E_V$ ) and IV ( $E \leq E_V$ ) to drain injected states. Regions II and III of course do not contribute neither to transport, nor to charge fluctuations. Instead turning on random injection of states only for region I or IV, the enhancement disappears (Fig. 3.15), pointing out that the positive correlation between hole interband tunneling from the drain and thermionic electron injection from the source is key to enhancement. In addition, the total injection noise obtained by randomizing the statistics everywhere can be roughly expressed as the sum of the injection noise contributions obtained by separately randomizing the statistics in regions I and IV. Partition noise is instead not affected by the considered statistics (Fig. 3.15), because it is fully taken into account by the shot noise formula [52, 55].

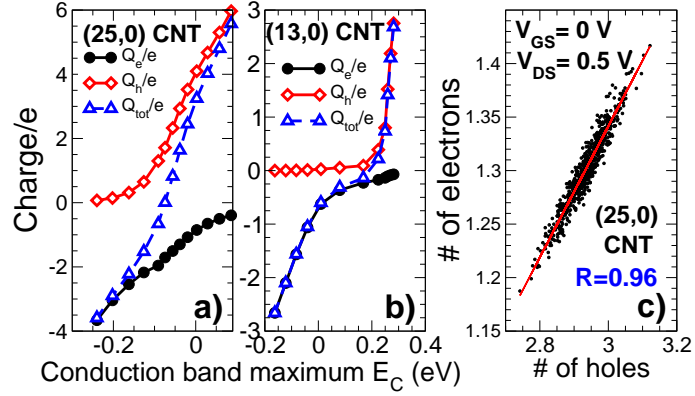


Figure 3.14: Electron, hole and total charge as a function of  $E_C$  for (a) (25,0) and (b) (13,0) CNTs. (c) Number of electrons transmitted in the channel as a function of the number of holes tunneling from the drain.

Significantly, lowering the temperature (Fig. 3.16a) suppresses shot noise enhancement by reducing the injection noise, due to the suppression of the hole trapping-detrapping process. Therefore, at  $T=77$  K (Fig. 3.16b) noise enhancement disappears, although a maximum in the injection noise can still be observed when  $E_{BS}$  almost aligns with  $E_{FD}$ .

It is also interesting to evaluate the cutoff frequency  $f_H$  of shot noise enhancement, which in this case is limited by the process of charging and discharging channel with holes: it is therefore the cutoff frequency of an  $R$ - $C$  circuit, where  $C$  is the total capacitance of the channel, and  $R$  is the quasi-equilibrium resistance between drain and channel [68, 69]. In order to do that, we need to evaluate  $C$  from Fig. 3.14a, obtaining  $C \approx 5.5$  aF.

Then we need to compute the conductance  $G = 1/R$  between the channel and the drain due to interband tunneling. Following Bardeen [84], tunneling can be treated as an electronic transition between energy levels in different regions. The matrix element for a transition at energy  $E$  from a state in the conduction band  $b_C$  at the drain into a state in the valence band  $b_V$  in the channel can be expressed as [85]:

$$M(E) = \hbar^2 T(E) J_V(E) J_C(E) \quad (3.2)$$

where  $J_V(E)$  ( $J_C(E)$ ) is the current probability incident on the barrier from  $S$  ( $D$ ) (Fig. 3.17a), while  $T(E)$  is the transmission probability of

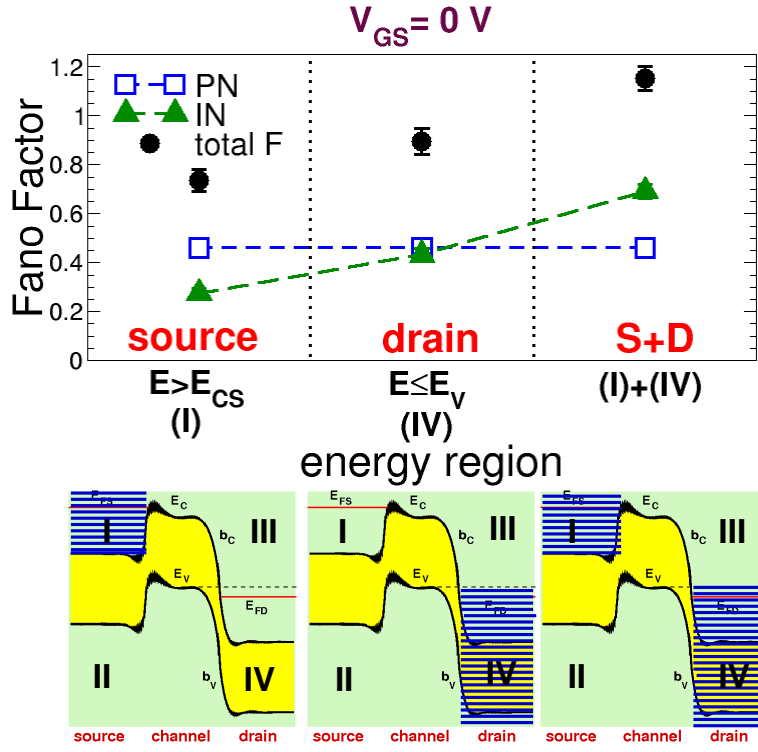


Figure 3.15:  $F$ ,  $F_{PN}$  and  $F_{IN}$  when randomizing the occupancy at different energy regions and at different reservoirs (source (S): I,II; drain (D): III, IV) for  $V_{GS} = 0$  V. Blue shaded areas indicate energy regions where the occupancy is randomized.

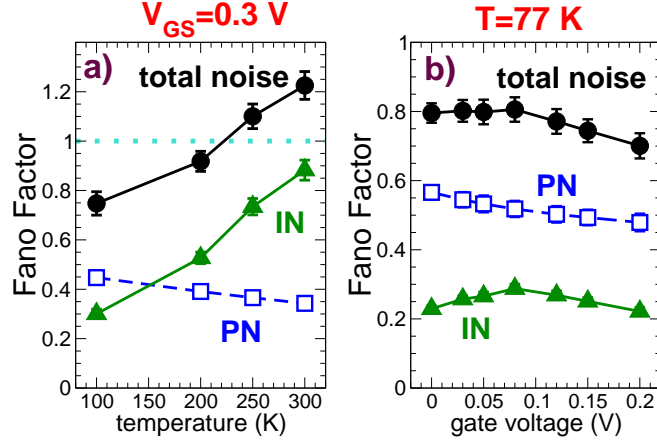


Figure 3.16: a)  $F$ ,  $F_{PN}$  and  $F_{IN}$  at  $V_{GS} = 0.3 \text{ V}$  as a function of temperature and b) as a function of  $V_{GS}$  for  $T = 77 \text{ K}$ .

the interband barrier, which has been evaluated by considering the band profile in correspondence of the source constant and equal to the value assumed at source/channel interface (Fig. 3.17b), as in Ref. [86].

The transition probability per unit time is given by the Fermi's golden rule:

$$\nu(E) = \frac{2\pi}{\hbar} |M(E)|^2 \rho_V(E) \quad (3.3)$$

where  $\rho_V(E)$  is the density of states in  $b_V$  in the channel. The tunneling frequency  $g$  can be obtained by summing on all empty states in  $b_C$  at the drain and on all occupied states in  $b_V$  in the channel:

$$g = 4\pi\hbar \int_{E_{VS}}^{E_V} dE T(E) J_V(E) J_C(E) \rho_V(E) \rho_C(E) f_D(E) (1 - f_D(E)) \quad (3.4)$$

where  $\rho_C(E)$  is the density of states in  $b_C$  at the drain and the occupancy in  $b_V$  in the channel has been approximated to  $f_D(E)$ . By exploiting  $J_C(E) \rho_C(E) = 2\pi\hbar$  [85, 64], we finally obtain  $G$  as:

$$G = \left( \frac{e^2}{KT} \right) g. \quad (3.5)$$

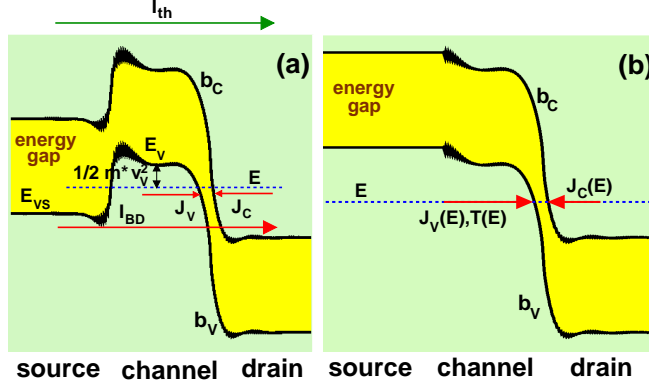


Figure 3.17: a) Conduction and valence band edge profiles for  $V_{DS} = 0.5$  V and  $V_{GS} = 0$  V. b) Band profile used to evaluate the transmission coefficient  $T(E)$ .

In addition, the product  $J_V(E)\rho_V(E)$  has been approximated as

$$J_V(E)\rho_V(E) \approx \frac{v_V(z_{middle}, E)}{2L_C} \int_{channel} \rho_V(z, E) dz, \quad (3.6)$$

where  $L_C$  is the channel length,  $v_V(z_{middle}, E)$  is the velocity of a carrier with energy  $E$  coming from the left and computed at the longitudinal coordinate  $z_{middle}$  (in the middle of the channel), whereas  $\rho_V(z, E)$  is the mean DOS computed at  $E$  and  $z$ .  $v_V(z, E)/(2L_C)$  instead represents the attempt frequency in the device region [85].

Instead the electron velocity can be derived through the effective mass approximation. The effective mass for a CNT [87] reads  $m^* = (4\hbar^2) / (9a_{CC}dt_0)$ , where  $a_{CC} = 0.144$  nm is the carbon-carbon (CC) bond length,  $t_0 = 2.7$  eV is the nearest neighbor CC tight binding overlap energy,  $d = 1.98$  nm is the diameter of the carbon nanotube. The kinetic energy  $1/2 m^* v_V(z, E)^2$  is instead given by the difference between the valence band edge in the channel at the longitudinal coordinate  $z$  and the total energy  $E$  (see Fig. 3.17a). We obtain  $G \approx 4.7 \times 10^{-5}$  S. Note that  $G$  and  $C$  are such that we are at the limit of the Coulomb blockade regime: the charging energy is comparable to the thermal energy, but we can still consider  $f_H = G/(2\pi C) \approx 1.36$  THz.

In conclusion, we predict that shot noise enhancement can be observed in CNT-FETs biased in the weak subthreshold regime, due to the

modulation of thermionic current caused by interband tunneling of holes between the drain and the channel. In (25,0) CNT-FETs, the enhancement is expected to be observable down to a temperature of 200 K and up to THz frequencies.

### 3.5 Concluding remarks

In this chapter we have quantitatively evaluated shot noise in ballistic quasi one-dimensional CNT-FETs and SNW-FETs by self-consistently solving the electrostatics and the transport equations within the NEGF formalism, within a statistical approach which manages to include also Coulomb repulsion among electrons and presented in chapter 2.

In the first part, we focus on (13,0) CNT-FETs and SNW-FETs, obtaining a shot noise suppression. In particular, we show that by only using Landauer-Büttiker noise formula, i.e. considering only Pauli exclusion principle, one can overestimate shot noise by as much as 180 %. Furthermore, with our approach we are able to observe a rectification of the DC characteristics due to fluctuations of the channel potential, and to identify and evaluate quantitatively the different contributions to shot noise. We are also able to consider the exchange interference effects, which are often negligible but can be measurable when a defect, introducing significant mode mixing, is inserted in the channel.

In the second part, we instead predict that shot noise enhancement can be observed in (25,0) CNT-FETs biased in the weak subthreshold regime, due to the modulation of thermionic current caused by interband tunneling of holes between the drain and the channel. In (25,0) CNT-FETs, the enhancement is expected to be observable down to a temperature of 200 K and at frequencies well above those in which flicker noise is dominant.

## Chapter 4

# Atomistic investigation of low-field mobility in graphene nanoribbons

Two-dimensional (2D) graphene sheets have demonstrated really attractive electrical properties like high carrier mobility [3, 4] and large coherence length [7]. However, experimental data of mobility available in the literature show huge dispersion, ranging from  $10^2$  to  $10^5$   $\text{cm}^2/\text{Vs}$  at room temperature, signaling that the fabrication process is still poorly optimized and not fully repeatable. To guide process optimization, an exhaustive interpretation of physical mechanisms limiting mobility would be extremely useful. For Graphene NanoRibbons (GNRs) a comprehensive experimental characterization of mobility is still lacking, mainly due to the difficulty in patterning in a repeatable way very narrow ribbons. Few recent interesting experiments are reported in [12] and [18]. GNRs may also suffer significant degradation of mobility due to additional scattering mechanisms, such as edge roughness.

The single most important aspect that makes graphene interesting for nanoscale electronics is its very high mobility. It is therefore of paramount importance to understand if also nano structured graphene

can preserve the high mobility (often) measured in graphene sheets, much larger than that of conventional semiconductors. In addition, one would need to understand the effect on mobility of different options for graphene functionalization, which could be required to open a semiconducting gap in graphene.

In the current situation, theoretical investigations [21, 88] and numerical simulations [89, 90, 91, 92] can represent a useful tool to assess the relative impact of different sources of non-idealities on mobility and consequently on device performance, to provide guidelines for the fabrication process and a realistic evaluation of the perspectives of graphene in nanoelectronics.

An analytical method and a Monte Carlo approach have for example been adopted in order to study line-edge roughness (LER) and phonon scattering-limited mobility in Ref. [21] and Ref. [88], respectively. However, due to the reduced width of the considered devices, effects at the atomistic scale are relevant, therefore accurate simulation approaches like semi-empirical tight-binding are needed.

In this chapter we present atomistic simulations of GNR-FETs, considering GNR widths ranging from 1 to 10 nm, and including scattering due to LER, single defects, ionized impurities, acoustic and optical phonons. A direct comparison with recently fabricated devices [12] will also be performed. Statistical simulations performed on a large ensemble of nanoribbons with different occurrences of the spatial distribution of non-idealities show that phonons, LER and defects scattering can likely explain the few available experimental data [12], where mobility is down to the level of mundane semiconductors (order of  $10^2$ - $10^3$  cm<sup>2</sup>/Vs).

## 4.1 Methodology

A long GNR-FET channel, where mobility is properly defined, is given by a series of  $N$  GNR segments of length  $L$  like those we have considered in the simulation (Fig. 4.1). For the  $i$ -th GNR segment, the resistance  $R_i = V_{DS}/I_i$  is the sum of two contributions, the channel resistance  $R_{ch,i}$  and the contact (ballistic) resistance  $R_B = V_{DS}/I_B$  ( $R_i = R_{ch,i} + R_B$ ), where  $V_{DS}$  is the drain-to-source voltage, whereas  $I_i$  and  $I_B$  are the total current and the ballistic current in the  $i$ -th segment, respectively. Assuming phase coherence is lost at the interface between segments, the resistance  $R_{tot}$  of the long channel GNR is therefore the sum of  $N$  channel resistances and one contact resistance, i.e.:



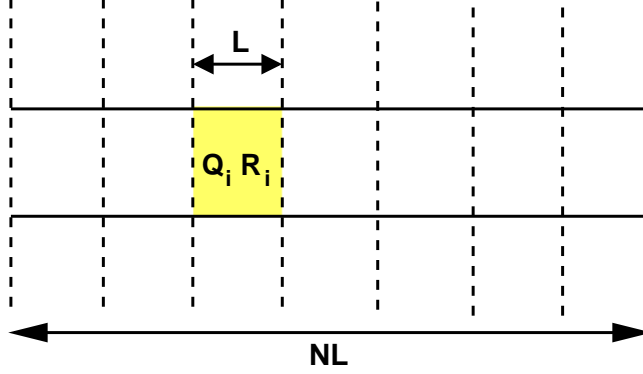


Figure 4.1: GNR-FET channel with length  $NL$  and the simulated GNR segment with length  $L$ .

$$R_{tot} = \left( \sum_{i=1}^N R_{ch,i} \right) + R_B = N \langle R \rangle - (N-1) R_B, \quad (4.1)$$

where  $\langle R \rangle = (1/N) \sum_{i=1}^N R_i$  is the mean resistance evaluated on the ensemble of nanoribbon segments. Therefore, the mobility of a long channel would read:

$$\mu_n = \frac{L_{tot}^2 G_{tot}}{Q_{tot}} = \frac{L_{tot}^2}{Q_{tot}} \frac{1}{N \langle R \rangle - (N-1) R_B}, \quad (4.2)$$

where the index  $n$  denotes each type of scattering mechanism limiting mobility (defects, edge-roughness or impurities),  $L_{tot} = NL$  is the total GNR length,  $Q_{tot} = \sum_{i=1}^N Q_i = N \langle Q \rangle$  is the total charge in the channel and  $\langle Q \rangle$  is the mean mobile charge in a segment.

For large values of  $N$ , one can discard 1 with respect to  $N$  in Eq. (4.2) so that we obtain the formula we use in this chapter:

$$\mu_n = \frac{L^2}{(\langle R \rangle - R_B) \langle Q \rangle}, \quad (4.3)$$

The root mean square error of mobility  $\sigma_\mu$  has been computed by means of a Taylor expansion up to the first order of Eq. (4.3) with respect to

statistical fluctuations of the resistance  $R = R_{ch} + R_B$ :

$$\Delta\mu = \left| \frac{\partial\mu}{\partial R} \right| \Delta R = \frac{L^2}{\langle Q \rangle} \frac{\Delta R}{(\langle R \rangle - R_B)^2} = \mu \frac{\Delta R}{\langle R \rangle - R_B}, \quad (4.4)$$

and therefore

$$\sigma_\mu^2 = \left( \frac{\mu}{\langle R \rangle - R_B} \right)^2 \sigma_R^2 \quad (4.5)$$

where  $\Delta R = \sqrt{\sigma_R^2/N}$  and

$$\sigma_R^2 = 1/(N-1) \sum_{i=1}^N (R_i - \langle R \rangle)^2 \quad (4.6)$$

is the variance of  $R$ .

Statistical simulations of resistance on a large ensemble of nanoribbon segments with different actual distribution of non-idealities have been performed. In particular, the mobility  $\mu_n$  has been computed in the linear transport regime, for large gate voltages ( $V_{GS}$ ) and small drain-to-source bias  $V_{DS} = 10$  mV. Mobility has been extracted by means of Eq. (4.3) considering an ensemble of  $N = 600$  nanoribbon segments with different disorder realizations for 1.12 nm-wide GNRs. Due to the computational cost, at least 40 nanoribbons segments have been instead simulated for 10.10 nm-wide GNRs.

Statistical simulations of random actual distributions of defects, LER and ionized impurities have been computed through the self-consistent solution of 3D Poisson and Schrödinger equations within the NEGF formalism, with a  $p_z$  tight-binding Hamiltonian [91, 92], extensively exploiting our open-source simulator NanoTCAD ViDES [56]. In particular, we have imposed at both ends of the segments null Neumann boundary conditions on the potential, and open boundary conditions for the transport equation.

In order to compute the LER-limited mobility  $\mu_{LER}$ , statistical simulations have been performed considering a given fraction  $H$  of single vacancy defects at the edges.  $H$  is defined as the probability for each carbon atom at the edges to be vacant. In practice, each sample of nanoribbon with edge disorder is randomly generated assuming that each carbon site at the edges has a probability  $H$  to be replaced by a vacancy. Null hopping parameter has been imposed in correspondence of a defect at the edge.

Defects have been modeled using the on-site energy and the hopping parameter extracted from DFT calculations [93]. In particular, for a

fixed defect concentration  $n_d$ , each sample of defected nanoribbon with defects is randomly generated assuming that each carbon atom has a probability  $n_d$  to be replaced by a vacancy.

As previously assumed in ab-initio calculations [94], we have considered a surface impurity distribution of positive charges equal to  $+0.4 q$  placed at a distance of 0.2 nm from the GNR surface, where  $q$  is the elementary charge. Again, if  $n_{IMP}$  is the impurity fraction, a sample with surface impurities is randomly generated by assuming that each carbon atom has a probability  $n_{IMP}$  to be at 0.2 nm from an impurity in the dielectric layer.

In Figs. 4.2a-b, we show the distributions of  $Q$  when considering line-edge roughness ( $H = 5\%$ ) and defects ( $n_d = 2.5\%$ ) for  $W = 1.12$  nm. In each picture we show the mean value  $\langle Q \rangle$  and the standard deviation  $\sigma_Q$  of the random variable  $Q$ . For comparison, the corresponding normal distribution is shown.

The effect of phonons (both acoustic and optical) on carrier transport is addressed by means of a full band (FB) approach based on a tight-binding description [95] of the electronic structure and of the phonon spectrum [96, 97]. Scattering rates are computed within the first-order perturbation theory and the deformation potential approximation (DPA), whereas the low-field intrinsic phonon-limited mobility  $\mu_{in}$  has been derived using the Kubo-Greenwood formula modified for 1D transport [98]. According to theory [99] and Raman spectroscopy [100], out-of-plane ZA and ZO modes (flexural modes) have been demonstrated to be negligible down to 130 K, therefore they are neglected in this chapter. Instead, all the in-plane longitudinal acoustic modes (LA) and in-plane optical modes (LO, TO) are considered. Details on this approach will be given in the next chapter.

As a final remark, the effective mobility including all type of scattering sources has been extracted by means of Mathiessen's rule  $1/\mu_{tot} = 1/\mu_{LER} + 1/\mu_d + 1/\mu_{IMP} + 1/\mu_{in}$ , where  $\mu_d$  and  $\mu_{IMP}$  are the defect and impurity limited mobilities, respectively. We have verified the validity of Mathiessen's rule considering samples with more sources of non-idealities (i.e. LER, ionized impurities and defects) at the same time. Then we have compared the computed mobility with that obtained by adding single contributions with Mathiessen's rule, observing a relative error smaller than 3%, which lies within the statistical error [92].

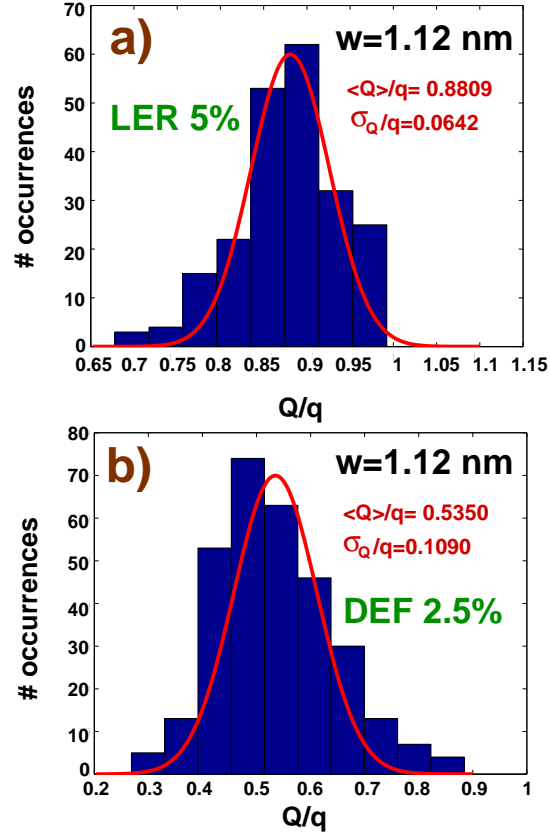


Figure 4.2: The distributions of charge  $Q$  in each GNR segment ( $W = 1.12$  nm) obtained from statistical simulations of random distributions of (a) LER ( $H = 5\%$ ) and (b) defects ( $n_d = 2.5\%$ ).

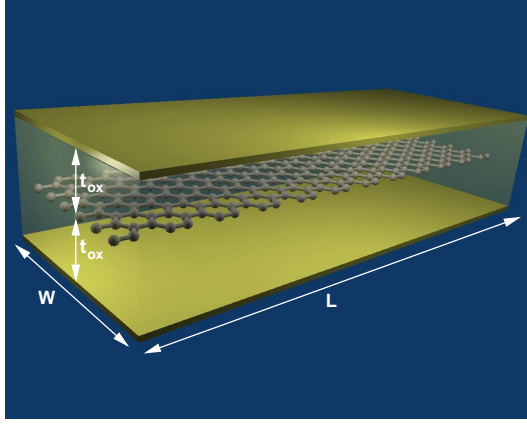


Figure 4.3: 3D structure of the simulated GNR segment.

## 4.2 Results and Discussions

The simulated segment is a double-gate GNR, embedded in  $\text{SiO}_2$  with an oxide thickness  $t_{ox}$  of 2 nm, 10 nm-long (Fig. 4.3). The segment length has been chosen to satisfy the assumption of loss of phase coherence at the segment ends. Indeed, according to recent experiments [101], the phase coherence length is close to 11 nm in graphene. From a computational point of view, different widths  $W$  have been considered, ranging from 1 to 10 nm: 1.12 nm, 2.62 nm, 4.86 nm and 10.10 nm. All simulations have been performed at room temperature  $T = 300$  K.

### 4.2.1 Line-edge roughness limited mobility

LER-limited mobility as a function of  $W$  for different edge-defect concentrations  $H$  is shown in Fig. 4.4a in the above-threshold regime, for a 2D carrier density  $n_{2D}$  of  $9 \times 10^{12} \text{ cm}^{-2}$ . As in all figures in this chapter, the error bars represent the estimated root mean squared error  $\sigma_\mu$  of the average of the statistical sample (4.5).

As predicted by the analytical model in Ref. [21],  $\mu_{LER}$  scales as  $W^4$ . Such behavior holds for large  $H$  ( $\approx 20\%$ ) and narrow GNRs ( $W < 5$  nm), when scattering from edge defects is expected to be heavier, while, for wider GNRs and for smaller  $H$ , such a law is not obeyed. In particular, for GNR width larger than 5 nm,  $\mu_{LER}$  tends to saturate, since the in-

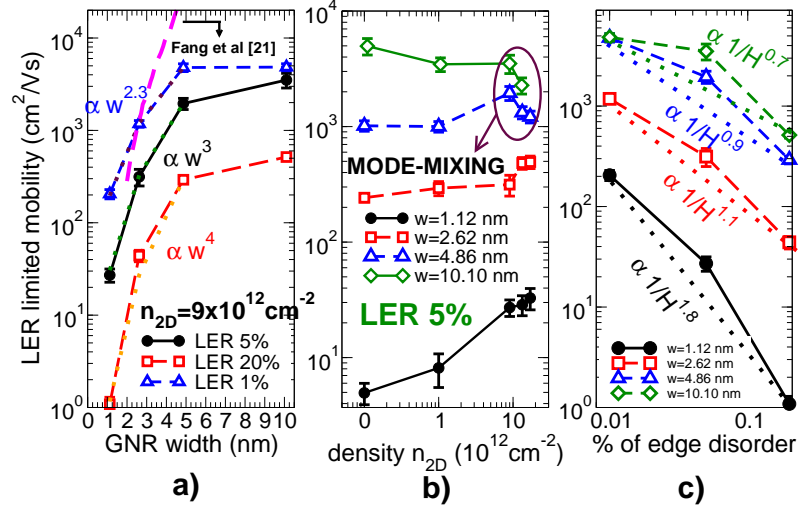


Figure 4.4: a) LER-limited mobility as a function of  $W$  for  $n_{2D} = 0.9 \times 10^{13} \text{ cm}^{-2}$  and for different  $H$ . Data extracted from Ref. [21] are also reported. b) LER-limited mobility as a function of  $n_{2D}$  for  $H = 5\%$ . c) LER-limited mobility as a function of edge disorder concentration  $H$  for  $n_{2D} = 0.9 \times 10^{13} \text{ cm}^{-2}$  and for different GNR width  $W$ .

creasing number of subbands contributing to transport counterbalance the number of final states available for scattering, enhancing scattering rates. As shown in Fig. 4.4b, in narrower GNRs, the higher the electron density, the larger the effective mobility, because of stronger screening.  $\mu_{LER}$  decreases for high  $n_{2D}$  and wider GNRs, due to mode-mixing, as already observed in Silicon Nanowire FETs [102]. Indeed, for wider GNRs biased in the inversion regime, more transverse modes are able to propagate in the channel due to the reduced energy separation between different subbands. This leads edge defects to become a source of intermode scattering, thus reducing  $\mu_{LER}$  [91, 92].

Fig. 4.4c shows  $\mu_{LER}$  as a function of  $H$ , where  $\mu_{LER} \propto 1/H$  for wide GNRs, consistent with the Drude model, and also observed in graphene in the presence of defects [19]. However, as soon as  $W$  decreases, quantum localization becomes relevant [103], and the Anderson insulator-like behavior [90] is recovered ( $\mu_{LER} \propto 1/L^2$ ), in agreement with analytical predictions [21].

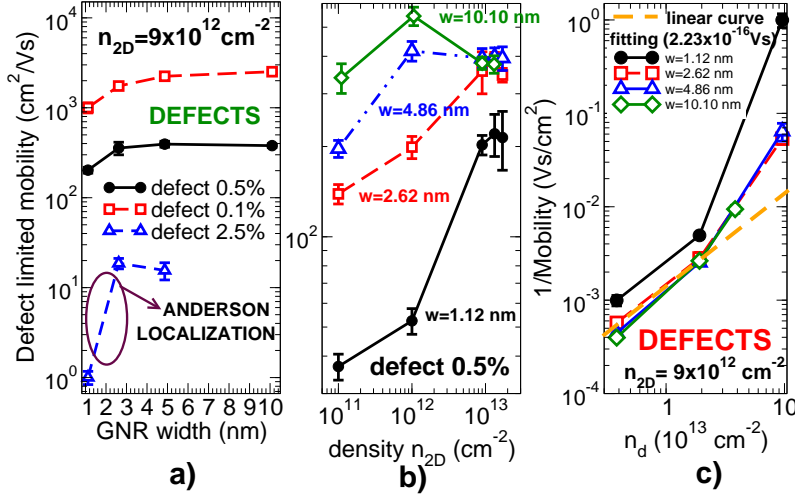


Figure 4.5: a) Defect-limited mobility as a function of  $W$  for  $n_{2D} = 9 \times 10^{12} \text{ cm}^{-2}$  and for different defect fraction  $n_d$ . b) Mobility as a function of  $n_{2D}$  for a defect fraction  $n_d = 0.5\%$ . c) Inverse of the mobility as a function of  $n_d$  for  $n_{2D} = 9 \times 10^{12} \text{ cm}^{-2}$  and for different GNR widths  $W$ .

#### 4.2.2 Defect-limited mobility

Defect-limited mobility is plotted in Fig. 4.5a as a function of  $W$  for different defect concentrations. Even in this case, localization affects mobility in narrower ribbons, especially for higher  $n_d$  (2.5%).

For a fixed defect density, mobility slightly increases with electron density, due to the larger screening (Fig. 4.5b) and, for larger GNRs biased in the inversion regime, it saturates with increasing  $W$ , for the same reason discussed above for LER scattering [91, 92]. In Fig. 4.5c,  $\mu_d$  is plotted as a function of  $n_d$ . The wider the ribbons the closer mobility follows the simple Drude model ( $\mu_d \propto 1/n_d$ ), as expected for strong disorder and uncorrelated scatterers in 2D graphene sheets [104]. For  $W = 10.10 \text{ nm}$  atomistic simulations are in agreement with experimental results: a linear curve fitting ( $\mu = C/n_d$ ) leads to a proportionality factor of  $2.23 \times 10^{-16} \text{ Vs}$ , similar to those extracted in the case of  $\text{Ne}^+$  and  $\text{He}^+$  irradiated graphene samples ( $7.9 \times 10^{-16} \text{ Vs}$  and  $9.3 \times 10^{-16} \text{ Vs}$ , respectively) [19].

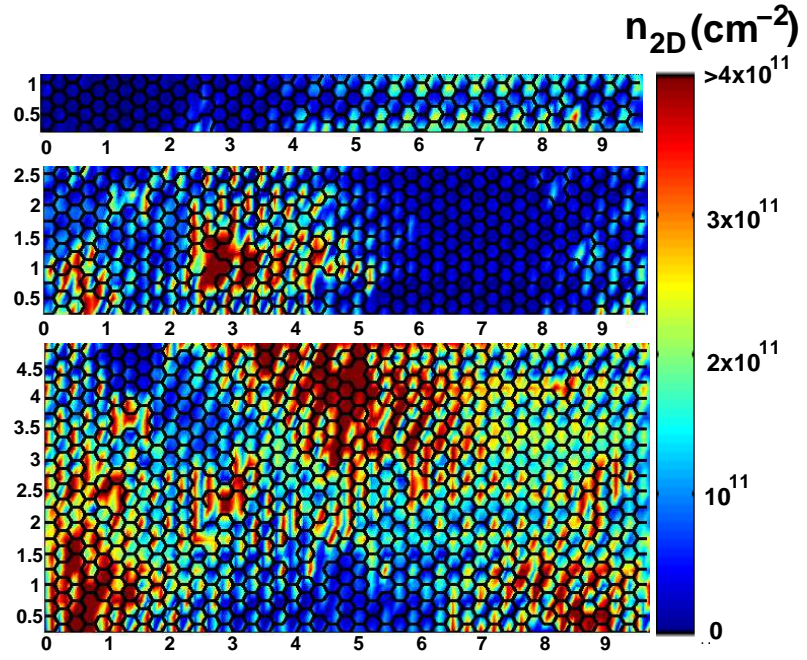


Figure 4.6: Carrier density  $n_{2D}$  in the GNR channel for different GNR width:  $W = 1.12$  nm,  $2.62$  nm and  $4.86$  nm (from top to bottom).



In Fig. 4.6, the GNR carrier density for widths ranging from 1.12 nm to 4.86 nm is shown. As can be seen, in Fig. 4.6, Anderson localization strongly degrades electron mobility [103], creating percolating paths in wider GNRs and blocking conduction in the narrower ones [92].

### 4.2.3 Ionized impurities limited mobility

Impurity-limited mobility  $\mu_{IMP}$ , as a function of  $W$ , is shown in Fig. 4.7a for  $n_{2D} = 9 \times 10^{12} \text{ cm}^{-2}$ , and for different impurity charge concentrations. As can be noted, even a high impurity concentration of  $10^{12} \text{ cm}^{-2}$  yields large mobility for  $0.4e$  impurity charge. However, no indications are present in literature regarding the amount of unintentional doping charge [105, 20]. Therefore, in order to check also the effect of impurity ionization on the electron transport, statistical simulations have been performed by increasing the impurity charge up to  $+2e$ . Mobility as a function of the impurity charge is plotted in Fig. 4.7b for different  $W$  and for  $n_{2D} = 9 \times 10^{12} \text{ cm}^{-2}$ . In this case smaller values of  $\mu$  ( $1700 \text{ cm}^2/\text{Vs}$ ) are obtained for very narrow GNRs, due to the strongly non-linear impact on screening in the channel. Even in this case localization strongly degrades mobility for narrower ribbons [91, 92].

To further test the importance of unintentional doping in limiting mobility, we have considered excess charge densities up to  $10^{13} \text{ cm}^{-2}$ , which have been encountered in experiments [105]. As shown in Fig. 4.7a, in this case mobility decreases down to  $10^2 \text{ cm}^2/\text{Vs}$  for narrower GNRs. In Fig. 4.7c impurity-limited mobility is plotted as a function of  $n_{2D}$  for  $n_{IMP} = 10^{12} \text{ cm}^{-2}$  and impurity charge  $+0.4e$  and for different  $W$ . According to [106, 6],  $\mu_{IMP}$  in graphene does not depend on the electron density. The behavior is different in GNRs because up to an electron density of  $10^{12} \text{ cm}^{-2}$ , only the ground state is occupied, so that the Size Quantum Limit approximation is verified [107, 21]. Since the scattering rate  $1/\tau \propto \epsilon^{-2}$  [106] and the static dielectric function  $\epsilon$  increases with  $n_{2D}$  [107], the screening becomes stronger with increasing  $n_{2D}$ . As a consequence,  $\mu_{IMP} \propto \tau$  in GNRs has the increasing monotonic behavior shown in Fig. 4.7c. In Fig. 4.7d, we compare experimental results available in literature [20] for graphene, showing the inverse of the impurity-limited mobility as a function of  $n_{IMP}$  for  $W = 10.10 \text{ nm}$  and by considering an impurity charge of  $+0.4e$ : as expected for uncorrelated scatterers,  $\mu_{IMP} \propto 1/n_{IMP}$  and, as can be seen, experiments and simulations show quite good agreement.

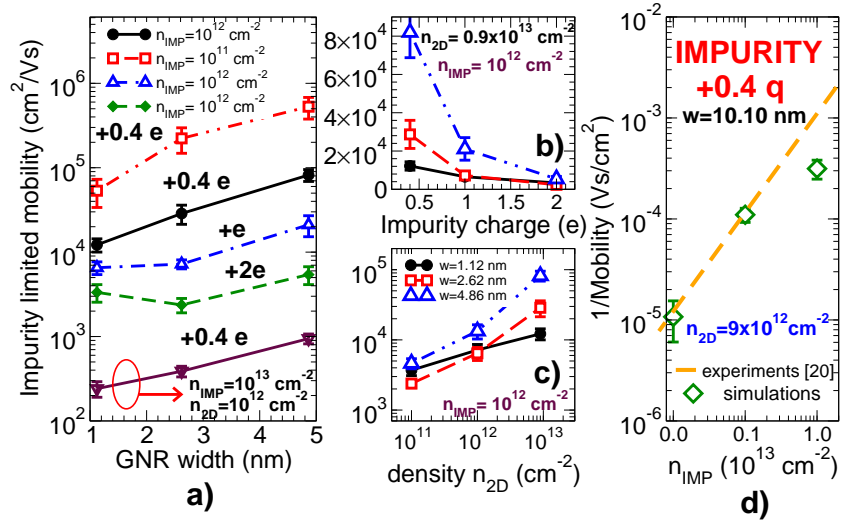


Figure 4.7: a) Impurity-limited mobility as a function of  $W$  for different impurity concentrations  $n_{\text{IMP}}$  and impurity charges. b) Mobility as a function of the impurity charge for  $n_{\text{IMP}} = 10^{12} \text{ cm}^{-2}$  and for different  $W$ . In a) and b)  $n_{2D} = 0.9 \times 10^{13} \text{ cm}^{-2}$ , except otherwise specified. c) Impurity-limited mobility as a function of  $n_{2D}$  for different  $W$  ( $n_{\text{IMP}} = 10^{12} \text{ cm}^{-2}$  and the impurity charge is  $+0.4e$ ). d) Inverse mobility as a function of  $n_{\text{IMP}}$  for  $W = 10.10 \text{ nm}$ . The carrier density is  $n_{2D} = 0.9 \times 10^{13} \text{ cm}^{-2}$ . The experimental slope  $2 \times 10^{-16} \text{ Vs}$  extracted in Ref. [20] is also reported.

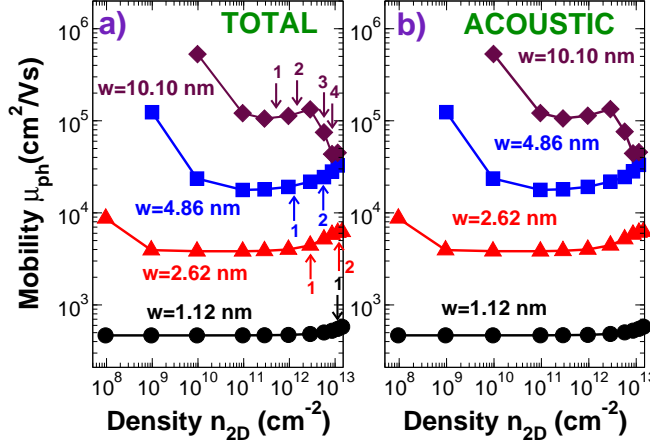


Figure 4.8: (a) total phonon-limited mobility  $\mu_{in}$  and (b) acoustic phonon-limited mobility as a function of  $n_{2D}$  for different  $W$ . In (a) the threshold densities at which the different subbands are activated are sketched.

#### 4.2.4 Acoustic and optical phonon-limited mobility

Our study has also been directed towards the investigation of the impact of phonon scattering, through the Kubo-Greenwood formalism [98, 108]. A wide range of phonon parameter values (i.e. acoustic ( $D_{AC}$ ) and optical ( $D_{OP}$ ) deformation potentials) is currently present in the literature [3, 24, 21, 6]. Actually, in the literature, only LA modes are taken into account [21, 88], since DPA formally leads to a zero coupling of the TA modes, while ZA modes (flexural modes) have been demonstrated both by theory [99] and Raman spectroscopy [100] to be negligible down to 130 K. Recent ab-initio calculations [24] have anyway demonstrated that TA modes play a role in degrading  $\mu_{in}$ , and they can be included within the DPA by means of an effective  $D_{AC}$ , computed through the fitting with ab-initio simulations. However, a physical description of graphene taking into account long-range interaction between carbon atoms has shown an off-diagonal coupling to the TA modes through the modulation of the hopping parameters, which is smaller than the on-diagonal deformation potential contribution [109]. On this basis, we choose to adopt a physically consistent approach and use DPA consid-

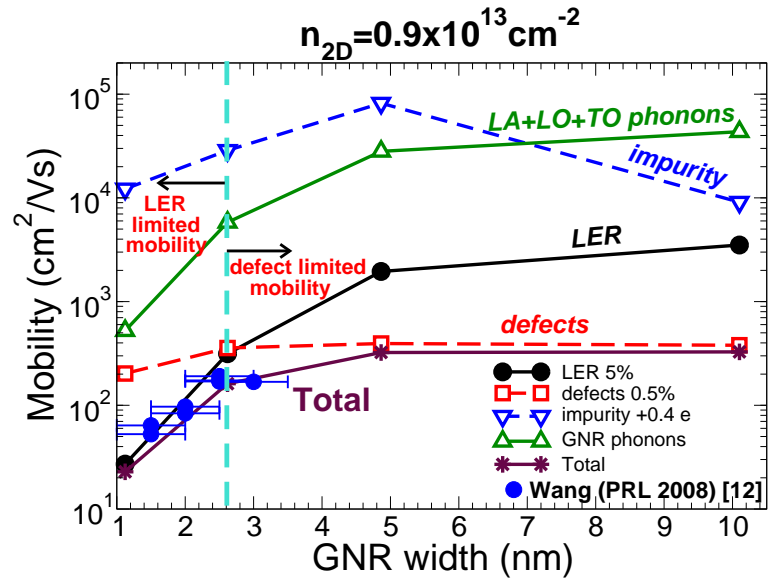


Figure 4.9: Mobility limited by GNR phonons, LER, defect and impurity scattering in the inversion regime for a LER concentration  $H=5\%$ ,  $n_d = 0.5\%$ . Intrinsic phonon-limited mobility  $\mu_{in}$  computed through a full band approach is also shown. The experimental mobility from [12] is also reported.  $n_{2D} = 0.9 \times 10^{13} \text{ cm}^{-2}$ ,  $n_{IMP} = 10^{12} \text{ cm}^{-2}$ .

ering electron coupling only with LA, LO and TO modes, rather than euristically reintroduce the contribution of TA modes [96, 97]. In particular, we use  $D_{AC} = 10.9$  eV, extracted from DFT calculation for the GNR family  $3l+1$  [110], rather than fitting experiments which are affected by uncontrolled mechanisms and actually lead to a large spread of the considered values for  $D_{AC}$  [21, 6, 24].

In Figs. 4.8a-b the total phonon-limited mobility  $\mu_{in}$  and the acoustic phonon-limited mobility are shown as a function of  $n_{2D}$ . As expected, emission scattering rates are found to be larger than absorption scattering rates, due to their higher Bose-Einstein occupation numbers. In addition, as also observed in graphene [25], we have verified that the contribution of optical phonons is negligible also in GNRs, and  $\mu_{in}$  is dominated by (intravalley) acoustic phonon scattering [21, 88] (Fig. 4.8b). Note also that, unlike in graphene where  $\mu_{in} \propto 1/n_{2D}$  [26], in GNRs the transverse confinement leads to a non-monotonic  $n_{2D}$ -dependence as in CNTs [111]. As can be seen,  $\mu_{in}$  slightly increases due to the reduced number of available states for scattering.

We observe that several recent studies [26, 27, 22] have demonstrated that surface phonons of the substrate represent a severe source of scattering, which strongly limits transport in graphene. However, according to previous works for graphene [26, 27, 22] and to our results for GNRs shown in the next chapter, this effect is expected to be much larger in high- $k$  dielectrics like  $\text{HfO}_2$ , rather than in  $\text{SiO}_2$ , which is the insulator considered in this chapter.

Finally, we compare the total mobility with experiments from Wang et al [12] (Fig. 4.9). In particular, we show the mobility limited by different scattering mechanisms as well as the total mobility computed by means of Mathiessen's rule. As can be seen, LER is the most limiting mechanism ( $H = 5\%$ ) for very narrower GNRs, while for wider GNRs defect scattering is predominant, if a  $n_d = 0.5\%$  is considered. As an additional remark, we have checked that the same conclusion holds even if we consider higher deformation potentials for phonons, that increase the impact of phonon scattering, such as those provided in Refs. [21, 88].

### 4.3 Concluding remarks

We have defined a simulation methodology based on atomistic simulations on statistically significant ensembles of GNR segments to understand the functional dependence of GNR mobility upon different factors,

and to quantitatively assess the importance of different scattering mechanisms.

We used such methodology to investigate mobility in GNRs of width ranging from 1 to 10 nm. First, we find that, unlike in 2D graphene, electron-impurity scattering in GNRs is far too weak to affect low-field mobility. In addition, using well established parameters for electron-phonon coupling, we find that phonon scattering is hardly the limiting factor of GNR mobility. For narrower GNRs, line-edge roughness is the main scattering mechanism. This result is consistent with the findings in [18], where wider nanoribbons with very rough edges are characterized. Finally, for a fixed defect density or LER, mobility tends to decrease with the GNR width for narrower devices, suggesting the occurrence of localization effects.

## Chapter 5

# Strong mobility degradation in graphene nanoribbons due to phonon scattering

Graphene has demonstrated really impressive physical properties, making its study one of the hottest topics in nanoelectronics. In particular, graphene monolayers exhibit very high mobility close to  $10^5 \text{ cm}^2/\text{Vs}$  [6] near room temperature, which further increases down to liquid helium temperatures, approaching the ballistic limit [5]. However, from a technological point of view, graphene is a zero-gap semiconductor [112], and this aspect prevents its use in digital electronic applications. In order to open a bandgap, efforts have been directed towards defining lateral confinement by patterning graphene [8, 113] in nano stripes, the so called Graphene NanoRibbons (GNRs), with width smaller than few tens of nanometers.

While interesting effects like quantum localization [103], or Coulomb blockade [114] have been observed in GNRs, understanding mobility is an important issue to assess the real potential for electronic applications. Electron mobility has been predicted to be mainly limited by line-edge roughness (LER) in sub-60 nm GNRs [18, 21, 91, 92].

Electron-phonon coupling [27, 26, 22, 21] is of primary importance, since it provides information regarding the ultimate *intrinsic* mobility

limit ( $\mu_{in}$ ) of a material, i.e., when all *extrinsic* scattering sources have been removed. This is especially important for new materials or nanostructured ones, such as graphene nanoribbons, where many questions regarding the main scattering mechanisms still remain open.

While recent experiments have found large mobility degradation in graphene deposited on high- $k$  gate insulators [3, 27, 26, 22], very few indications are available on mobility degradation in GNRs [115]. As of now,  $\mu_{in}$  in sub-10 nm GNRs cannot be extracted from experiments since line-edge roughness is the most limiting scattering mechanism in state-of-the-art GNRs [12, 18, 92]. On the other hand, a theoretical approach allows to individually evaluate the impact of each scattering mechanism on mobility.

So far, there are only few theoretical models addressing this topic in suspended GNRs [21, 88, 116]. In Ref. [88] for example the importance of electron-phonon interaction has been remarked, but a critical dependence on the proper choice of phonon parameters has also been recognized. Ref. [116] presents an investigation of electron-optical phonon interaction in metallic armchair GNRs, showing that it is dominant only far from the bottom of the lowest conduction subband, leading to a negligible contribution to low-field transport [92, 21].

The main assumption behind these works is that flexural acoustic phonons ZA and transversal acoustic phonons TA can be neglected, so that the Deformation Potential Approximation (DPA) can be assumed, which leads to a zero coupling for TA and ZA modes. This is in agreement with Raman spectroscopy [100], which have shown that ZA modes are negligible down to 130 K.

However, results based on a tight-binding description of electron-phonon coupling [117] and recent ab-initio calculations [24] have demonstrated that TA modes play a comparable role as that of LA modes in degrading  $\mu_{in}$ .

On the other hand, a physical description of graphene taking into account long-range interaction between carbon atoms highlights an off-diagonal coupling to the TA modes through the modulation of the hopping parameters, which is smaller than the on-diagonal deformation potential contribution [109]. In addition, through a simple two-band (conduction and valence bands) model based on local variations in the bond lengths induced by phonons [118], TA modes have been demonstrated to induce only interband transitions in zigzag GNRs. According to Ref. [110], TA modes are expected to play a softer role in GNRs with respect to 2D graphene, due to their quasi-one dimensional characteris-



tics. As a consequence, we will consider only LA, LO and TO modes.

Unlike two-dimensional graphene, momentum along the confined direction is not conserved in low-dimensional materials [119], which in turn leads to increased intrasubband scattering. We note that this consideration has been rarely taken into account in the literature [120, 119] and the strong inelasticity caused by transverse momentum conservation uncertainty has not yet been considered adequately in graphene-based materials.

In addition, the two-component nature (spinor) of the nanoribbon wavefunction cannot be ignored, since it leads to an energy-dependent overlap factor and which has been as well neglected in 2D models for GNRs [88].

In this chapter, we investigate the effect of intrinsic phonons and surface optical (SO) phonons on carrier transport in GNRs by means of a full-band (FB) approach [96, 97], including intersubband scattering, which is expected to significantly reduce mobility in the wider nanoribbons with respect to previous calculations [21]. Our approach is based on a tight-binding description of the electronic structure and a force-constant dynamic-matrix approach for the computation of the phonon dispersion curves [95]. We consider both intrasubband and intersubband scattering of in-plane LA, LO and TO modes within the DPA. According to symmetry-based considerations [121], density functional study [122, 123] and Raman spectroscopy [100], out-of-plane vibrations are much weaker than in-plane vibrations and are not therefore discussed here. Moreover, we take rigorously into account conservation uncertainty of the transverse momentum. We finally compute low-field mobility using the Kubo-Greenwood formula for 1D channels [98].

In Sections 5.1 and 5.2 we present the theoretical background and the methodology used in the full-band approach. For comparison purpose, we present also in Appendix C a broad overview of approximate approaches [21, 88, 92], which have been used in the past in order to estimate scattering rates and low-field intrinsic mobility in GNRs. In Section 5.3, we discuss the full-band results, making a quantitative comparison with results obtained through approximate descriptions of electron-phonon coupling. Finally, in Section 5.4, we summarize the main results of this chapter.

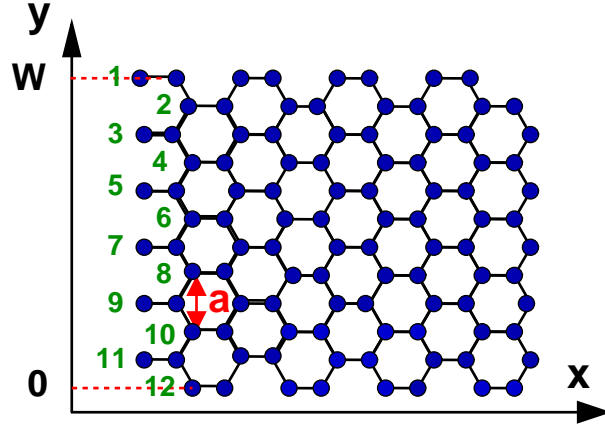


Figure 5.1: A portion of an armchair nanoribbon with width  $W$  and  $l = 12$  dimer lines.

## 5.1 Full-band approach

### 5.1.1 GNR phonons

The considered Armchair Graphene NanoRibbon (A-GNR) is sketched in Fig. 5.1, where  $x$  and  $y$  denote the longitudinal and the transverse directions, respectively. Imposing Dirichlet boundary conditions at the edges  $y = -a/2$  and  $y = W + a/2$  of a GNR with  $l$  dimer lines, we get  $l$  subbands (Figs. 5.2a-b), with transverse wavevector:

$$k_{y\eta} = \frac{2\pi\eta}{(l+1)a}, \text{ where } \eta = 1, \dots, l. \quad (5.1)$$

For GNR length  $L$  much larger than the GNR width  $W = a/2(l-1)$ , where  $a = \sqrt{3}a_{CC}$  ( $a_{CC} = 0.144$  nm) is the graphene lattice constant, the longitudinal wavevector  $k_x$  can be treated as continuous ( $-k_F \leq k_x \leq k_F$ , where  $k_F = \pi/(\sqrt{3}a)$ ). Figs. 5.2a-b show the electron dispersion curves calculated including edge relaxation [124] for  $W = 1.12$  nm and 4.86 nm.

Imposing the same boundary conditions for phonon wavefunctions, each of the 6 phonon branches of graphene — labelled by the quantum number  $j$  ( $j = 1 - 3$  for acoustic (AC) and  $j = 4 - 6$  for optical (OP) branches, respectively) — is splitted into  $l$  subbranches of the GNR,

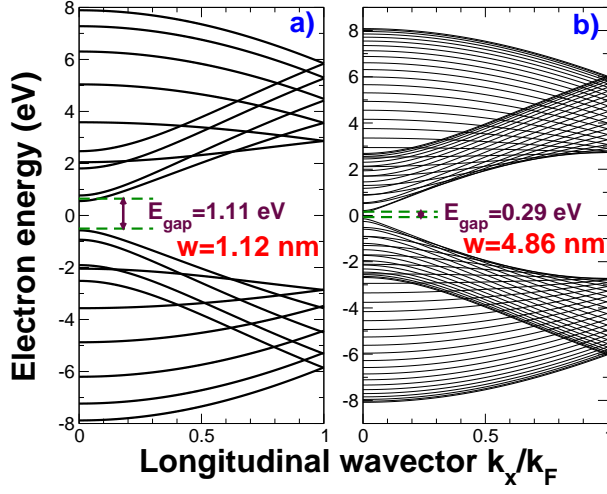


Figure 5.2: Electron dispersion curves calculated including edge relaxation [124] for different GNR widths: (a)  $W = 1.12$  nm and (b)  $W = 4.86$  nm.

with transverse wavevector

$$\begin{aligned}
 q_{y\beta} &= \frac{2\pi\beta}{(l+1)a} & \text{for } \beta = 0, \dots, \frac{l}{2} - 1, \\
 q_{y\beta} &= \frac{2\pi(\beta+2)}{(l+1)a} & \text{for } \beta = \frac{l}{2}, \dots, l-1.
 \end{aligned} \tag{5.2}$$

In the following, for convenience, we will describe phonon subbranches by means of two quantum numbers  $(j, \beta)$ . In Figs. 5.3a-d GNR phonon dispersion curves, computed by means of the force-constant dynamic-matrix approach, including contributions up to the fourth nearest neighbor interactions (4NNFC approach) [95] and using force constant parameters extracted from first-principles calculations [125], are shown for four different values of  $W$  ranging from 1 nm to 10 nm. As an important remark, we note that our calculated sound velocities for the LA and TA modes of order  $\beta = 0$ , LA(0) and TA(0) respectively, agree very well with those generally reported in the literature for graphene-based devices [126, 127]. In particular  $v_{LA} = 20700$  m/s and  $v_{TA} = 13900$  m/s, respectively.

The two-component electronic eigenfunction corresponding to the  $\eta$ -th conduction subband, consistent with the tight-binding approach and

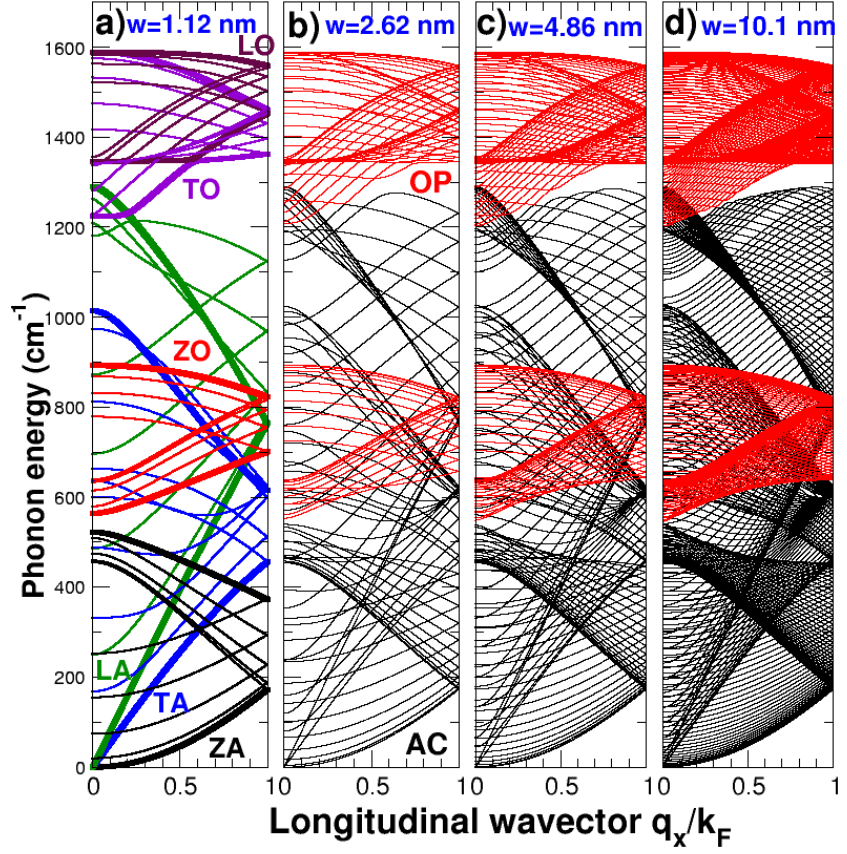


Figure 5.3: Phonon dispersion curves calculated by means of the 4NNFC approach for four different GNR widths:  $W = 1.12$  nm (a),  $W = 2.62$  nm (b),  $W = 4.86$  nm (c),  $W = 10.10$  nm (d). In (a) different colors correspond to different types of in-plane and of out-of-plane vibrations. In addition, the lowest and the highest subbranches of each symmetry are shown in bold. In (b)-(d) black (red) curves refer to acoustic (optical) subbranches.

hard-wall boundary conditions, has to be a mixture of the two valleys  $\mathbf{K}$  and  $\mathbf{K}'$  of the underlying 2D graphene band structure [128]:

$$\Psi_{\mathbf{k}}(x, y) = \frac{1}{\sqrt{2L}} \Psi_{\perp, \eta}(y) e^{ik_x x} \begin{pmatrix} 1 \\ -e^{-i\theta_{\mathbf{k}}} \end{pmatrix}, \quad (5.3)$$

where  $W+a$  is the width of the transverse region where the eigenfunction is defined, according to zero-boundary condition [128], whereas

$$e^{i\theta_{\mathbf{k}}} = \frac{t_{\mathbf{k}}}{|t_{\mathbf{k}}|}, \quad (5.4)$$

$\Psi_{\perp, \eta}(y)$  is the transverse wavefunction

$$\Psi_{\perp, \eta}(y) = \sqrt{\frac{2}{W+a}} \sin \left[ k_{y\eta} \left( y + \frac{a}{2} \right) \right], \quad (5.5)$$

and

$$t_{\mathbf{k}} = t \left[ 1 + 2 \exp \left( -ik_x a \frac{\sqrt{3}}{2} \right) \cos \left( k_{y\eta} \frac{a}{2} \right) \right], \quad (5.6)$$

with  $t = 2.7$  eV is the graphene hopping parameter. The lattice displacement at point  $(x, y)$  at time  $t$  is given by:

$$\begin{aligned} \mathbf{u}(x, y, t) = & \sum_{j, \beta} \sum_{q_x} \left( \frac{\hbar^2}{2\rho L W E_{ph}^{j\beta}(\mathbf{q})} \right)^{1/2} e_{\mathbf{q}} \{ a_{\mathbf{q}} \exp[i(q_x x + q_{y\beta} y)] + \\ & + a_{\mathbf{q}}^{\dagger} \exp[-i(q_x x + q_{y\beta} y)] \}, \end{aligned} \quad (5.7)$$

where  $\rho \approx 7.6 \cdot 10^{-8}$  g/cm<sup>2</sup> is the 2D graphene mass density per unit surface [21],  $a_{\mathbf{q}}^{\dagger}$  and  $a_{\mathbf{q}}$  are the quantum operators which create and annihilate, respectively, a phonon with wavevector  $\mathbf{q} = (q_x, q_{y\beta})$  and energy  $E_{ph}^{j\beta}(q_x, q_{y\beta})$ , and  $e_{\mathbf{q}}$  is the unit polarization vector.

The dominant electron-phonon coupling arises from the deformation potential interaction, due to local change in the electron energy spectrum arising from lattice distortions induced by phonons [99, 129]. Within the DPA, the interaction potential for optical phonons is assumed to be proportional to the optical displacement  $\mathbf{u}$  [130]:

$$V_{OP}(x, y, t) = D_{OP} \mathbf{u}(x, y, t), \quad (5.8)$$

where  $D_{OP} = 1.4 \times 10^{11}$  eV/m is the optical deformation potential. Therefore the matrix element for the perturbation potential (5.8) averaged on the many-phonon states (with  $n_{\mathbf{q}}$  phonons) can be expressed as:

$$\langle n_{\mathbf{q}} \mp 1 | V_{OP} | n_{\mathbf{q}} \rangle = \sqrt{\frac{n_{\mathbf{q}}^{\mp} \hbar^2}{2\rho L W E_{ph}^{j\beta}}} D_{OP} \exp[\pm i(q_x x + q_y y)] , \quad (5.9)$$

where  $n_{\mathbf{q}}$  is the Bose-Einstein occupation number at thermal equilibrium,  $n_{\mathbf{q}}^- = n_{\mathbf{q}}$ ,  $n_{\mathbf{q}}^+ = n_{\mathbf{q}}^- + 1$  and the upper sign in Eq. (5.9) is for phonon absorption (ABS) and the lower for phonon emission (EM). The matrix element of the perturbation potential averaged on the electron wavefunction  $\Psi_{\mathbf{k}}$  reads:

$$\begin{aligned} \widetilde{V_{OP}} &= \langle \Psi_{\mathbf{k}'}, n_{\mathbf{q}} \mp 1 | V_{OP} | \Psi_{\mathbf{k}}, n_{\mathbf{q}} \rangle \\ &= \sqrt{\frac{n_{\mathbf{q}}^{\mp} \hbar^2}{8\rho L W E_{ph}^{j\beta}}} D_{OP} (1 + e^{-i\theta_{\mathbf{k}\mathbf{k}'}}) \times \\ &\quad \times [G(k_{y\eta}, k_{y\eta'}, q_{y\beta})]^{1/2} \delta(-k'_x + k_x \pm q_x) , \end{aligned} \quad (5.10)$$

where  $\theta_{\mathbf{k}\mathbf{k}'} = \theta_{\mathbf{k}} - \theta_{\mathbf{k}'}$  is due to the spinor nature of the GNR wavefunction (5.3),  $\theta_{\mathbf{k}}$  is defined in Eq. (5.8) and  $G(k_{y\eta}, k_{y\eta'}, q_{y\beta})$  is the form factor [119]:

$$\begin{aligned} G(k_{y\eta}, k_{y\eta'}, q_{y\beta}) &= \left[ \int_{-a/2}^{W+a/2} dy \Psi_{\perp, \eta'}^*(y) e^{iq_{y\beta} y} \Psi_{\perp, \eta}(y) \right]^2 \\ &= \frac{2[(2\pi)^2 q_{y\beta} (W+a) \eta \eta']^2 [1 - (-1)^{\eta+\eta'} f_{y\beta}]}{\left[ (f_{y\beta})^4 - 2\pi^2 (f_{y\beta})^2 (\eta^2 + \eta'^2) + \pi^4 (\eta^2 - \eta'^2)^2 \right]^2} , \end{aligned} \quad (5.11)$$

In Eq. (5.11)  $f_{y\beta} = \cos[q_{y\beta}(W+a)]$  and the integration is performed in the transverse region, where the electron eigenfunction is defined. As can be observed in Eq. (5.10), the exact conservation of the longitudinal momentum is explicitly indicated by the Kronecker delta function. Instead, due to the lack of translational invariance along the confined  $y$  direction, the transverse momentum is not conserved and, for narrow ribbons, the form factor  $G$  [Eq. (5.11)] significantly deviates from the Kronecker delta function. In particular,  $G$  has the absolute maximum

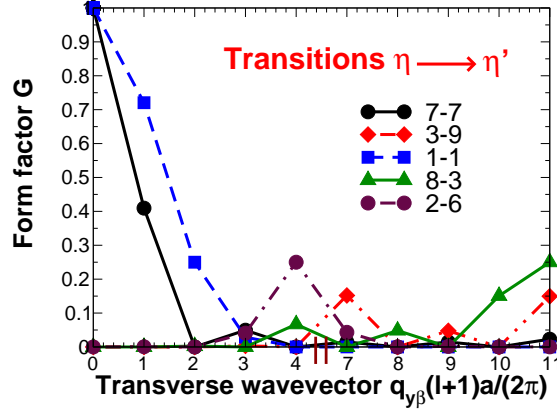


Figure 5.4: The form factor  $G$  [Eq. (5.11)] as a function of the normalized transverse phonon wavevector  $q_{y\beta}(l+1)a/(2\pi)$  for  $W = 1.12$  nm and considering few intrasubband and intersubband transitions. In the legend the electron quantum numbers  $\eta-\eta'$  are shown, i.e. 3-9 means  $\eta = 3$  and  $\eta' = 9$ . Note that  $\eta = 7$  and  $\eta = 8$  correspond to the first and second subbands, respectively.

for intrasubband scattering ( $\eta' = \eta$  and  $q_{y\beta} = 0$ ):

$$G = \left( \frac{2}{W+a} \right)^2 \left[ \int_0^{W+a} \sin^2 \left( \frac{\eta \pi y}{W+a} \right) dy \right]^2 = 1, \quad (5.12)$$

whereas the other maxima are for

$$\beta = \pm (\eta \pm \eta') \quad (5.13)$$

and are  $G = 1/4$ , except the  $\eta' = \eta$  case and  $\beta = 0$ , when a strong constructive interference occurs between the events  $q_{y\beta} \rightarrow 0^+$  and  $q_{y\beta} \rightarrow 0^-$ , yielding  $G = 1$  [131]. The form factor  $G$  is shown in Fig. 5.4 as a function of the normalized transverse phonon wavevector  $q_{y\beta}(l+1)a/(2\pi)$  for a 1.12 nm-wide GNR and considering few intrasubband and intersubband transitions. As can be seen, even for intrasubband scattering (transition  $1 \rightarrow 1$  or  $7 \rightarrow 7$  in Fig. 5.4),  $G$  is significantly larger than 0 not only when the transverse momentum is conserved ( $q_{y\beta} = 0$ ).

It is worth noticing that in the case of Carbon NanoTubes (CNTs) the crystal momentum  $\mathbf{k} = (k_x, k_{y\eta})$  is conserved, as in the 2D graphene

sheet, because of the cyclic boundary conditions [132]. This does not hold in A-GNRs, due to the imposed Dirichlet boundary conditions. Obviously, in the limit  $W \rightarrow +\infty$ , the form factor  $G$  tends to the Kronecker delta, i.e. the transverse momentum is conserved as in 2D graphene.

The electron-phonon scattering rate for an electron in the initial state  $\mathbf{k}=(k_x, k_{y\eta})$  to the final state  $\mathbf{k}'=(k'_x, k_{y\eta'})$ , via a phonon with momentum  $q_x$  in the subbranch  $(j, \beta)$  can be expressed as:

$$\begin{aligned} S^\beta(\mathbf{k}, \mathbf{k}') &= \frac{2\pi}{\hbar} |\widetilde{V_{OP}}|^2 \delta[E_{\mathbf{k}'} - E_{\mathbf{k}} \mp E_{ph}^{j\beta}(q_x, q_{y\beta})] \cdot \\ &= \frac{n_{\mathbf{q}}^\mp \pi \hbar D_{OP}^2 (1 + \cos \theta_{\mathbf{k}\mathbf{k}'})}{2\rho L W E_{ph}^{j\beta}(q_x, q_{y\beta})} G(k_{y\eta}, k_{y\eta'}, q_{y\beta}) \times \\ &\quad \times \delta[E(k_x \pm q_x, k_{y\eta'}) - E(k_x, k_{y\eta}) \mp E_{ph}^{j\beta}(q_x, q_{y\beta})] \frac{1-f(E_{\mathbf{k}'})}{1-f(E_{\mathbf{k}})} \end{aligned} \quad (5.14)$$

where  $\delta$  is the Dirac delta function accounting for the energy conservation and the factor  $[1-f(E_{\mathbf{k}'})]/[1-f(E_{\mathbf{k}})]$  has to be considered in the degenerate semiconductor conditions.

The total momentum relaxation rate from  $\mathbf{k}$  to all possible  $\mathbf{k}'$  is obtained by integrating Eq. (5.14) over the 1D Brillouin zone (BZ) for each of the  $3l$  phonon subbranches  $(j, \beta)$  and then by summing the  $3l$  contributions for all final electron states  $\mathbf{k}'$  which are allowed with regard to the law of conservation of energy and longitudinal momentum (Fig. 5.5):

$$\begin{aligned} \frac{1}{\tau_{OP}(\mathbf{k})} &= \sum_{\eta'=1}^l \sum_{j=5}^6 \sum_{\beta} \sum_{q_x} S^\beta(\mathbf{k}, \mathbf{k}') \left(1 - \frac{k'_x}{k_x}\right) \\ &= \sum_{\eta'=1}^l \sum_{j=5}^6 \sum_{\beta} \int_{-k_F}^{+k_F} dq_x \frac{n_{\mathbf{q}}^\mp \hbar D_{OP}^2}{4\rho W E_{ph}^{j\beta}} (1 + \cos \theta_{\mathbf{k}\mathbf{k}'}) \times \\ &\quad \times G(k_{y\eta}, k_{y\eta'}, q_{y\beta}) \delta[E(k_x \pm q_x, k_{y\eta'}) - E(k_x, k_{y\eta}) \mp \\ &\quad \mp E_{ph}^{j\beta}(q_x, q_{y\beta})] \left(1 - \frac{k'_x}{k_x}\right) \frac{1-f(E_{\mathbf{k}'})}{1-f(E_{\mathbf{k}})}. \end{aligned} \quad (5.15)$$

where the factor  $1 - k'_x/k_x$  accounts for both forward and backward scattering in quasi-1D systems,  $k'_x = k_x \pm q_x$  and  $j = 5, 6$  correspond to the TO and LO graphene modes, respectively.

For what concerns acoustic phonons, the interaction potential is proportional to the strain [130] induced by the lattice displacement (5.7):

$$V_{AC}(x, y, t) = D_{AC} \nabla \mathbf{u}(x, y, t), \quad (5.16)$$



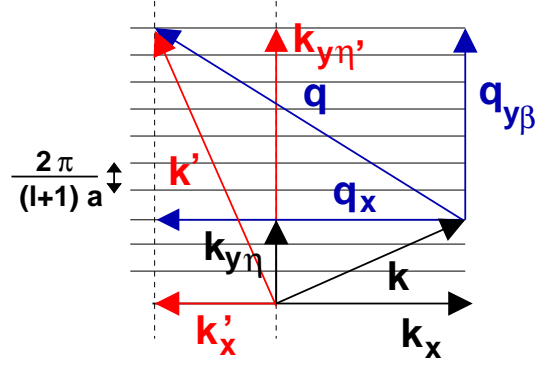


Figure 5.5: Graphical representation of the selection rule  $k'_x = k_x + q_x$  for an ABS process, when even the transverse momentum is conserved, i.e.  $k_{y\eta'} = k_{y\eta} + q_{y\beta}$ . In this figure a backscattering event is considered.

where  $D_{AC}$  is the acoustic deformation potential for in-plane vibrations [133]. Therefore the perturbation potential averaged on the many-phonon states reads:

$$\langle n_{\mathbf{q}} \mp 1 | V_{AC} | n_{\mathbf{q}} \rangle = \sqrt{\frac{n_{\mathbf{q}}^{\mp} \hbar^2}{2\rho L W E_{ph}^{j\beta}}} D_{AC} q \exp[\pm i(q_x x + q_y y)], \quad (5.17)$$

where  $q = \sqrt{q_x^2 + q_y^2}$ . It is worth noticing that Eq. (5.17) applies only to longitudinal acoustic modes LA since  $\mathbf{q} \cdot \mathbf{e}_{\mathbf{q}} = 0$  in the case of TA and ZA modes. The momentum relaxation rate due to scattering from acoustic phonons finally reads:

$$\begin{aligned} \frac{1}{\tau_{AC}(\mathbf{k})} &= \sum_{\eta'=1}^l \sum_{j=2}^2 \sum_{\beta} \sum_{q_x} S^{\beta}(\mathbf{k}, \mathbf{k}') \left(1 - \frac{k'_x}{k_x}\right) \\ &= \sum_{\eta'=1}^l \sum_{j=2}^2 \sum_{\beta} \int_{-k_F}^{+k_F} dq_x \frac{n_{\mathbf{q}}^{\mp} \hbar D_{AC}^2}{4\rho W E_{ph}^{j\beta}} (1 + \cos \theta_{\mathbf{k}\mathbf{k}'} \times \\ &\quad \times G(k_{y\eta}, k_{y\eta'}, q_{y\beta}) q^2 \delta[E(k_x \pm q_x, k_{y\eta'}) - E(k_x, k_{y\eta}) \mp \\ &\quad \mp E_{ph}^{j\beta}(q_x, q_{y\beta})] \left(1 - \frac{k'_x}{k_x}\right) \frac{1 - f(E_{\mathbf{k}'})}{1 - f(E_{\mathbf{k}})}, \end{aligned} \quad (5.18)$$

where  $j = 2$  corresponds to the LA graphene mode.

Let us note that for intravalley acoustic phonons scattering, which is the main scattering mechanism in intrinsic low-field mobility, the factor  $1 - k'_x/k_x$  can be replaced by  $1 - \cos \alpha$ , where  $\alpha$  is the angle between  $k_x$  and  $k'_x$ . In particular it is equal to 0 for forward scattering and to  $\pi$  for backward scattering. Indeed for quasi-1D system, by imposing the conservation of the energy and longitudinal momentum for each electron subband

$$\frac{(\hbar k'_x)^2}{2m_\eta} = \frac{(\hbar k_x)^2}{2m_\eta} + E_{ph} \quad (5.19)$$

$$k'_x = k_x \pm q_x, \quad (5.20)$$

where  $m_\eta$  is the effective mass of the  $\eta$ -th electron subband, we obtain:

$$q_x = \mp k_x \pm \left( k_x^2 \pm \frac{2m_\eta E_{ph}}{\hbar^2} \right)^{1/2}. \quad (5.21)$$

Since for intravalley acoustic phonons  $\hbar^2 k_x^2 / (2m_\eta) \gg E_{ph}$ , i.e. scattering is elastic, Eq. (5.21) can be simplified as:

$$\begin{aligned} q_x &\approx -k_x \pm k_x \text{ for ABS events,} \\ q_x &\approx +k_x \pm k_x \text{ for EM events.} \end{aligned} \quad (5.22)$$

As a consequence, for ABS we obtain  $q_x = 0, -2k_x$  and  $k'_x = \pm k_x$ , whereas for EM  $q_x = 0, 2k_x$  and  $k'_x = \pm k_x$ . Finally, we can write  $k'_x = k_x \cos \alpha$  for both ABS and EM events.

Note also that only six subbranches have zero transverse momentum  $q_{y\beta}$  (0-th modes). In particular the three acoustic subbranches with  $\beta = 0$  have zero phonon energy in the limit  $q_x \rightarrow 0$ . As indicated in Eq. (5.12), LA(0) mode is mainly involved in intrasubband electron transitions, since  $G$  has the main maxima  $G = 1$  for  $\eta' = \eta$  and  $\beta = 0$ . Instead most of the LA modes have a non-zero transverse momentum ( $\beta \neq 0$ ), and are involved in both intrasubband and intersubband electron scattering.

In Appendix C, we calculate the approximate expressions for Eqs. (5.18) and (5.15), accounting for intrasubband intravalley AC phonon scattering and using an effective phonon energy for the 0-th order LO mode [21]. From hereon we will refer to this approximation as approximation “IIS” (Intrasubband Intravalley Scattering). Within approximation IIS, in order to highlight the importance of spinor, we will refer instead to approximation “IISNS” (Intrasubband Intravalley Scattering No Spinor) when

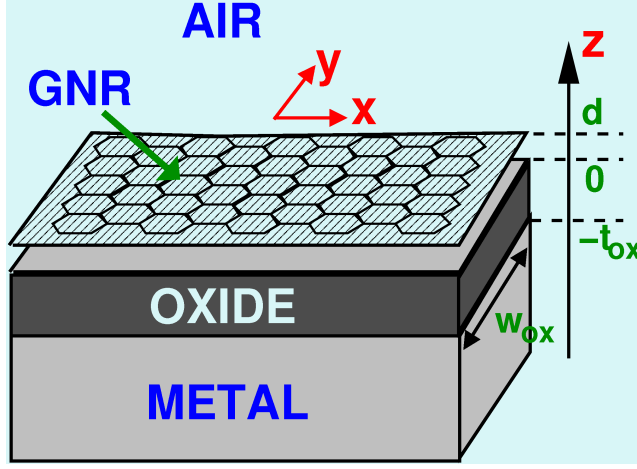


Figure 5.6: Sketch of the considered GNR/oxide/metal structure.

also neglecting the spinor. We also consider the case when both the spinor and the confinement of phonon wavefunction are neglected. Such approximation will be referred as approximation “2DPNS” (2D Phonons No Spinor).

### 5.1.2 Remote phonons

The electrostatic coupling between electrons in the GNR channel and polar vibrations of the substrate is modelled by considering the device geometry sketched in Fig. 5.6, where the GNR is placed at a distance  $d \approx 0.4$  nm [134] far from the oxide layer, whose thickness, length and width are equal to  $t_{ox}$ ,  $L$  and  $W_{ox}$ , respectively [96].

We also assume that the oxide is deposited on a metal gate. Since surface optical (SO) modes are nearly dispersionless, phonon energies  $E_{SO}^\beta$  are treated as constants as in Ref. [26]. The electron-phonon interaction Hamiltonian corresponding to the  $\beta$ -th SO mode reads [22, 27]:

$$H_{e-ph}^{SO} = eF_\beta \sum_{\mathbf{Q}} \left[ \frac{e^{-Qz}}{\sqrt{Q}} \left( e^{-i\mathbf{Q}\mathbf{r}} a_{\mathbf{Q}}^{\beta\dagger} + e^{i\mathbf{Q}\mathbf{r}} a_{\mathbf{Q}}^\beta \right) \right], \quad (5.23)$$

where  $z$  is the out-of-plane direction [22],  $\mathbf{Q}$  is the 2D wavevector in the ribbon plane,  $Q = |\mathbf{Q}|$ ,  $a_{\mathbf{Q}}^{\beta\dagger}$  ( $a_{\mathbf{Q}}^\beta$ ) represents the SO phonon creation

(annihilation) operator for the  $\beta$ -th mode and  $F_\beta$  is the electron-phonon coupling parameter [22, 27]:

$$F_\beta^2 = \frac{E_{SO}^\beta}{2LW_{ox}\epsilon_0} \left( \frac{1}{\epsilon_{ox}^\infty + 1} - \frac{1}{\epsilon_{ox}^0 + 1} \right). \quad (5.24)$$

In Eq. (5.24)  $\epsilon_0$  is the permittivity of vacuum,  $\epsilon_{ox}^\infty$  ( $\epsilon_{ox}^0$ ) is the high (zero) frequency dielectric constant of the dielectric. By means of Eq. (5.23), the scattering matrix element averaged on the electron and phonon wavefunctions reads:

$$\begin{aligned} |M_\beta(Q)|^2 &= |\langle n_{\mathbf{Q}} \mp 1, \Psi_{\mathbf{k}'}(\mathbf{r}) | H_{e-ph}^{SO} | n_{\mathbf{Q}}, \Psi_{\mathbf{k}}(\mathbf{r}) \rangle|^2 \\ &= \frac{e^2 F_\beta^2}{2Q} G(\eta, \eta', Q_y) e^{-2Qd} (1 + \cos \theta_{\mathbf{k}\mathbf{k}'}) n_{\mathbf{Q}}^\mp, \end{aligned} \quad (5.25)$$

where  $n_{\mathbf{Q}}^- = n_{\mathbf{Q}\beta}^-$ ,  $k'_x = k_x \pm q_x$ , the form factor  $G(\eta, \eta', Q_y)$  has the same form of Eq. (5.11) where  $q_{y\beta}$  is replaced by  $Q_y$ .

By exploiting Eq. (5.25) and assuming  $\Psi_{\mathbf{k}}(\mathbf{r}, z) = \Psi_{\mathbf{k}}(\mathbf{r}) \delta(z - d)$ , i.e electrons are confined in a plane, the momentum relaxation rate of an electron in the initial state  $\mathbf{k} = (k_x, k_{y\eta})$  is obtained by summing over all SO phonon modes:

$$\begin{aligned} \frac{1}{\tau_{ex}(\mathbf{k})} &= \frac{LW_{ox}}{2\pi\hbar} \sum_{\eta'=1}^l \sum_{\beta} \int_{-k_F}^{+k_F} dQ_x \int dQ_y \left| \frac{M_\beta(Q)}{\epsilon(Q)} \right|^2 \left( 1 - \frac{k'_x}{k_x} \right) \times \\ &\quad \times \delta(E_{\mathbf{k}'} - E_{\mathbf{k}} \mp E_{SO}^\beta) \frac{1 - f(E(\mathbf{k}'))}{1 - f(E(\mathbf{k}))} \\ &= \sum_{\eta'=1}^l \sum_{\beta} \int_{-k_F}^{+k_F} dQ_x \int dQ_y \frac{LW_{ox} e^2 F_\beta^2 G(\eta, \eta', Q_y) e^{-2Qd}}{4\pi\hbar [\epsilon(Q)]^2 Q} \times \\ &\quad \times (1 + \cos \theta_{\mathbf{k}\mathbf{k}'}) n_{\mathbf{Q}}^\mp \delta(E_{\mathbf{k}'} - E_{\mathbf{k}} \mp E_{SO}^\beta) (1 - k'_x/k_x) \frac{1 - f(E_{\mathbf{k}'})}{1 - f(E_{\mathbf{k}})} \end{aligned} \quad (5.26)$$

where  $\epsilon$  is the static dielectric function and  $E_{\mathbf{k}'} = E(k_x \pm Q_x, k_{y\eta'})$ .

In particular, for narrow ribbons ( $W < 5$  nm) we use the GNR static dielectric function calculated within the Random Phase Approximation (RPA) [21]:

$$\epsilon(Q) \equiv \epsilon_{1D}(Q_x) = 1 + \frac{e^2}{2\pi\epsilon_0\epsilon_{avg}} \mathcal{F}(Q_x) \mathcal{L}(Q_x), \quad (5.27)$$

where  $\epsilon_{avg} = (\epsilon_{ox}^0 + 1)/2$  is the average dielectric constant [21],  $\mathcal{F}$  determines the contribution to the screening of the coupled transverse modes and  $\mathcal{L}(Q_x)$  is the Lindhard function [21]: as in Refs. [21, 107],  $\mathcal{F}$  and  $\mathcal{L}$  are computed in the size quantum limit [21, 107]. For 10 nm-wide GNRs, screening of the electric field due to polar vibrations is instead modeled by means of the 2D RPA graphene static dielectric function  $\epsilon_{2D}(Q)$  [106].

## 5.2 Low-field GNR phonon-limited mobility

Scattering rates are proportional to the final density of states. Since the density of states exhibits peaks in Van Hove singularities, particular attention has to be paid when evaluating scattering rates in correspondence of such points. In particular, a collisional broadening approach has been adopted. The Dirac delta in Eqs. (5.15) and (5.18) has been represented by a Gaussian window function with a width  $\Delta E$  enclosing 11 momentum points close to locations which ensure the exact energy conservation for each scattering event. For the lowest AC subbranches, a self-consistent broadening of the Gaussian window function has been implemented for each term of the sum in Eqs. (5.15) and (5.18), according to the Heisenberg principle [97]:

$$\Delta E = \frac{\hbar}{2} \frac{1}{\tau(\mathbf{k}, q_{y\beta})}. \quad (5.28)$$

We have also verified a very satisfactory agreement between scattering rates computed by means of a Gaussian window and a rectangular window. In the latter case, up to three zeroes of the Fourier transform of the rectangular window have been taken into account, which allows to reduce noise in the scattering rates. Such solution has been preferred when self-consistency has been applied to AC subbranches.

Once the scattering rates are known, the low-field GNR phonon-limited mobility  $\mu_{in}$  has been computed by means of the Kubo-Greenwood formula modified for 1D transport [92, 135, 98]. In particular, when considering the FB approach, the following integration in the reciprocal

space has been performed [92]:

$$\begin{aligned}\mu_{in} &= -\frac{e}{\pi\hbar n_{2D}W} \sum_{\eta=1}^l \int_{-k_F}^{+k_F} dk_x \tau(\mathbf{k}) v(\mathbf{k}) \frac{\partial f(E(\mathbf{k}))}{\partial \mathbf{k}} \\ &= \frac{e}{\pi^3 k_B T \hbar^2 n_{2D}W} \sum_{\eta=1}^l \int_{-k_F}^{+k_F} dk_x \frac{\tau(\mathbf{k})}{[D_\eta(\mathbf{k})]^2} \\ &\quad f(E(\mathbf{k})) [1 - f(E(\mathbf{k}))],\end{aligned}\tag{5.29}$$

where

$$\frac{1}{\tau(\mathbf{k})} = \frac{1}{\tau_{AC}(\mathbf{k})} + \frac{1}{\tau_{OP}(\mathbf{k})}\tag{5.30}$$

is the inverse lifetime for an electron with initial momentum  $\mathbf{k} = (k_x, k_{y\eta})$  and energy  $E(\mathbf{k})$  [Eqs. (5.15) and (5.18)], whereas  $n_{2D}$  is the total electron density,  $T$  is the temperature,  $v(\mathbf{k}) = 1/\hbar (\partial E(\mathbf{k})/\partial \mathbf{k})$  is the band velocity and  $D_\eta(\mathbf{k}) = 1/\pi [dk_x/dE_\eta(\mathbf{k})]$  is the 1D density of states for the  $\eta$ -th electron subband.

When considering only intravalley intrasubband acoustic phonon scattering (approximation IIS) or when neglecting the spinor (approximation IISNS) and assuming 2D phonons (approximation 2DPNS), the effective mass approximation has been exploited considering four conduction subbands. In this case Eq. (5.29) reduces to [92]:

$$\begin{aligned}\mu_{EM} &= \frac{2e}{\pi\hbar n_{2D}W k_B T} \sum_{\eta} \int_{E_\eta}^{+\infty} dE \tau_\eta(E) \frac{f(E) [1-f(E)]}{E - E_\eta + E_{\eta 0}} \\ &\quad \left( \frac{E_{\eta 0}}{m_\eta} \left[ (E - E_\eta + E_{\eta 0})^2 - E_{\eta 0}^2 \right] \right)^{1/2},\end{aligned}\tag{5.31}$$

where  $\tau_\eta$  is the momentum relaxation time for an initial state on the  $\eta$ -th subband with cutoff energy  $E_\eta$  (equal to  $E_{\eta 0}$  for zero bias) and  $m_\eta$  is the effective mass of the  $\eta$ -th subband.

Eq. (5.29) is used also for SO phonons, where  $1/\tau(\mathbf{k}) = 1/\tau_{ex}(\mathbf{k})$ . In this case, the self-consistent broadening of the window function, i.e. Eq. (5.28), is not required.

### 5.3 Results

From a numerical point of view, GNR widths  $W$  ranging from 1.12 nm to 10.10 nm have been simulated at room temperature ( $T = 300$  K),

unless otherwise specified.

As a first step, efforts have been directed towards the determination of an effective deformation potential  $D_{AC}$  within the DPA approximation to use in the later calculations. Actually  $D_{AC}$  values are extracted by fitting experimental mobility of graphene samples, which has led to a wide spread of  $D_{AC}$  values reported in literature [26], ranging from  $\approx 17$  eV [3] to 29 eV [6]. This is due to the fact that the state-of-the-art graphene samples are far from being ideal, so that the measured mobility is not only affected by phonon scattering, but also by other sources of scattering such as LER.

Lacking of an exhaustive understanding of the intrinsic transport characteristics of graphene, density functional theory (DFT) can represent the only available tool to quantitatively evaluate the correct  $D_{AC}$ . Since recent ab-initio calculations [110] have reported a deformation potential  $D_{AC} \approx 10.9$  eV specific for the GNR family  $3l+1$  [110], in the following we will use such values in our simulations.

### 5.3.1 Scattering rates

We now focus on the scattering rates evaluated by exploiting the FB approach for GNR phonons [Eqs. (5.15) and (5.18)]. Unless otherwise specified, the Fermi level is in correspondence of the midgap. Figs. 5.7 refers to a 1.12 nm-wide GNR. In particular, Figs. 5.7a-b show the energy dispersion curves, whereas Figs. 5.7c-f show the different contribution to  $1/\tau$  due to absorption (ABS) and emission (EM) of AC and OP phonons, respectively. Due to the one-dimensional nature, scattering rates show peaks in correspondence of subband minima. As already found in graphene [25], emission rates are at least one order of magnitude higher than absorption rates, due to the higher occupation factor  $n_{\mathbf{q}}^+$ . Although scattering due to an emission of an OP phonon is stronger at high energy (Fig. 5.7f), an OP phonon may be emitted only if an high energy carrier participates to the scattering process. As a consequence, the low-field intrinsic mobility  $\mu_{in}$  is mainly determined by AC phonons [96, 97], as we will see in the following sections.

Figs. 5.8a-d show instead the different contribution to  $1/\tau$  for an electron in the first subband due to scattering with LA (intrasubband + intersubband and only intrasubband scattering), LO and TO phonons ( $W = 1.12$  nm). For narrow GNRs, intrasubband scattering gives the main contribution to the total LA scattering rate in a wide energy window up to 2 eV, as expected. In addition, due to their similar dispersion

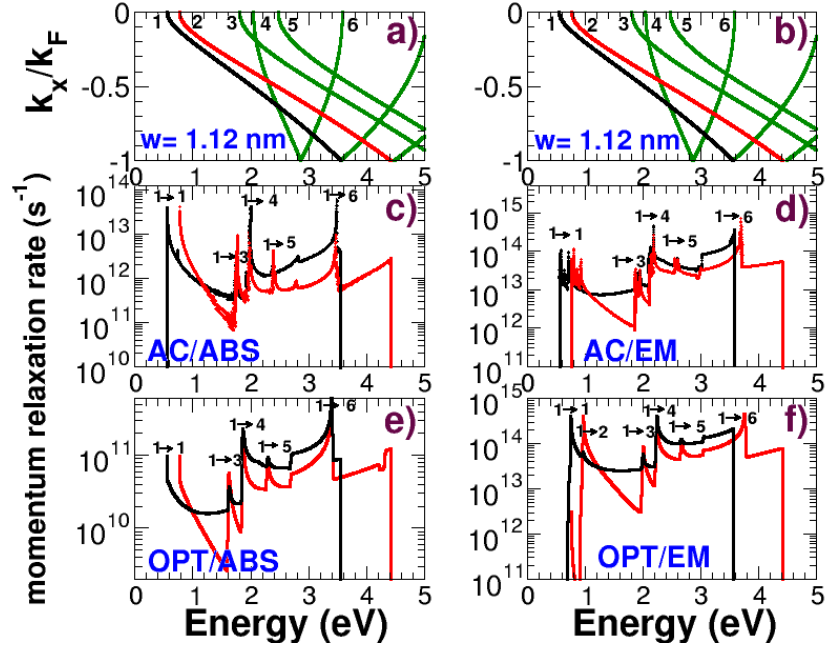


Figure 5.7: (a)-(b): conduction subbands for  $W = 1.12$  nm. (c)-(f): momentum relaxation rates for ABS and EM scattering events of AC phonons ((c) and (d), respectively) and OP phonons ((e) and (f), respectively) for the first two subbands 1 (black) and 2 (red).



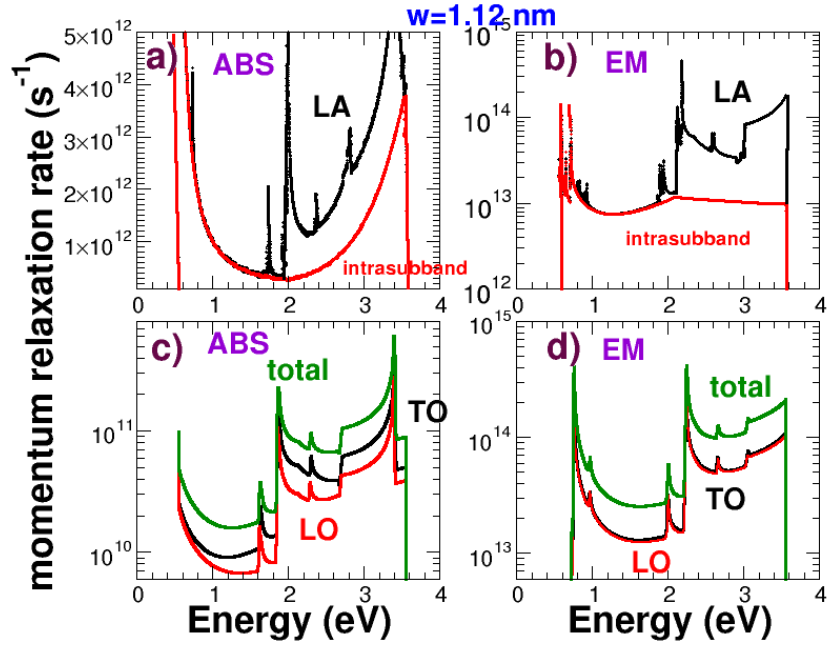


Figure 5.8: Contributions to the momentum relaxation rates due to ABS and EM of LA phonons ((a) and (b), respectively) and OP in-plane phonons ((c) and (d), respectively) for the first subband ( $W = 1.12$  nm). In (a) and (b) the intrasubband contribution is also depicted.

profiles, the in-plane OP vibrations yield comparable scattering rates and have to be properly taken into account in the transport model, especially when considering polaron formation [96].

In order to check the validity of our FB approach, we have also computed scattering rates of a graphene sheet in the 2D limit, thus removing the condition of backward scattering ( $\alpha = \pi$ ) and in the case of the widest considered GNR, i.e.  $W = 10.10$  nm. In such a case, the factor  $(1 - k'_x/k_x)(1 + \cos \theta_{\mathbf{k}\mathbf{k}'})$  in Eqs. (5.15) or (5.18) reduces to  $(1 - \cos \theta_{\mathbf{k}\mathbf{k}'})(1 + \cos \theta_{\mathbf{k}\mathbf{k}'}) = \sin^2 \theta_{\mathbf{k}\mathbf{k}'}$ . Rates are sketched in Figs. 5.9a-f in the  $(k_x, k_y)$  plane for one-phonon ABS and EM processes involving LA, LO and TO modes ( $W = 10.10$  nm). For a simple comparison with graphene scattering rates, we have plotted the transverse electron momentum  $k_y$  up to the Dirac point  $\mathbf{K}'$ . Qualitatively in agreement with Ref. [25], rates drop down in correspondence of the  $\Gamma$  and  $\mathbf{K}'$  points of the Brillouin zone and are isotropic around the  $\Gamma$  point.

### 5.3.2 Optical energy offset

The obtained FB scattering rates can be exploited to evaluate the optical energy offset to be used in the approximation IIS, IISNS and 2DPNS [97, 136]. In Fig. 5.10 the energy offset for the LO and TO modes ( $E_{LO}$  and  $E_{TO}$ , respectively) are shown as a function of  $W$ , considering for LO phonons three different cases: (i) only intrasubband scattering ( $\eta' = \eta$ ) with  $q_{y\beta} = 0$  (i.e. transverse momentum conservation); (ii) no constrain on  $q_{y\beta}$  (i.e. transverse momentum not conserved); (iii) both intrasubband and intersubband scattering.

Let us stress some main learnings. First, the energy offset exhibits a weak GNR width dependence ( $E_{LO}, E_{TO} \propto 1/W^\alpha$  with  $\alpha \approx 0.02$ ), therefore the adoption of a constant offset represents an accurate approximation even for narrower GNRs. Second, our calculated  $E_{LO}$  agrees very well with those generally used in the literature [21, 88, 100] (152-160 meV), referred to the zone-boundary graphene LO mode. Third, for the case (i)  $E_{LO}$  is almost equal to 180 meV. As a consequence, the use of the energy offset  $E_{LO} = 160$  meV, within a model accounting for only intrasubband scattering in the transverse momentum conservation approximation, is incongruous, as shown in Fig. 5.10.

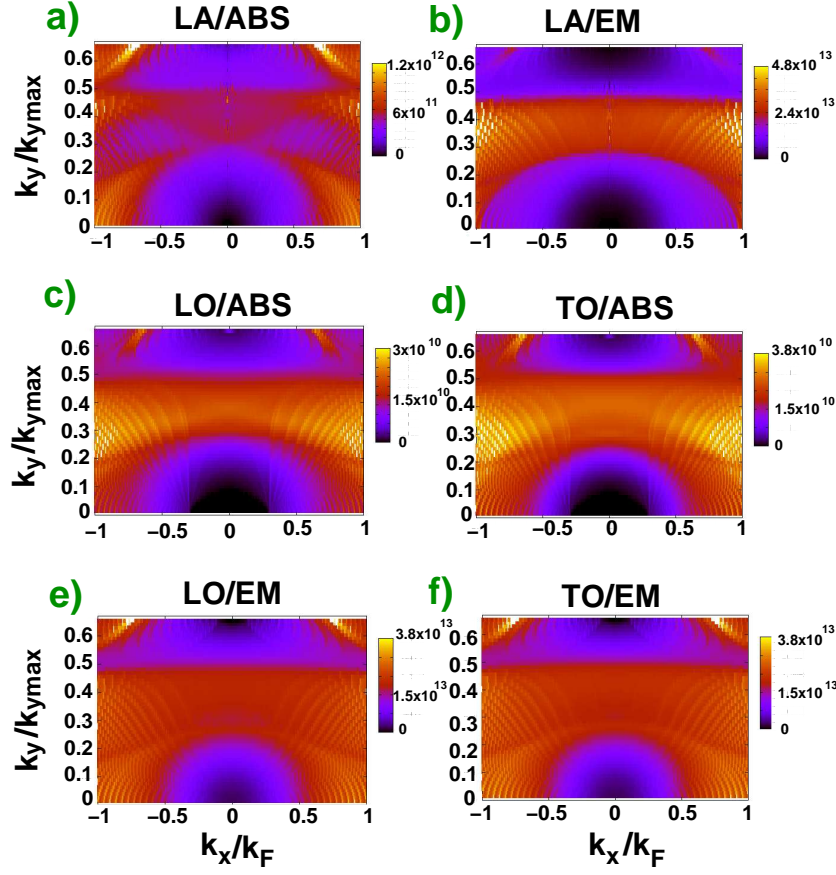


Figure 5.9: (a)-(f) 2D limit of the momentum relaxation rates in the  $(k_x, k_y)$  plane for ABS and EM scattering events involving LA, LO and TO phonons for a 10.10 nm-wide GNR.  $k_{ymax}$  is the maximum transverse electron momentum:  $k_{ymax} = k_{y\eta}$  for  $\eta = l$ .

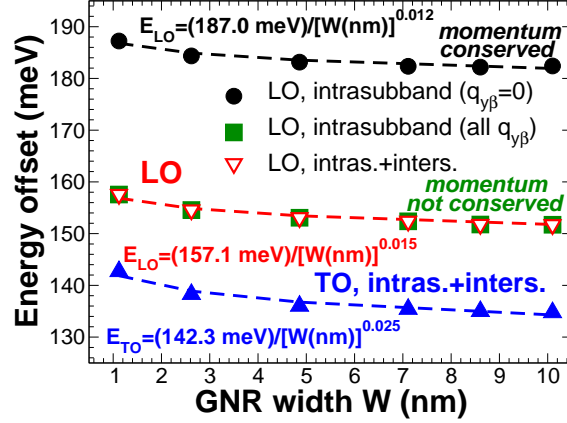


Figure 5.10: Optical energy offset as a function of  $W$  for the TO (blu triangles) and LO modes. In the latter case, black circles and red triangles correspond to only intrasubband scattering, accounting for or neglecting the transverse momentum conservation, respectively. Green squares correspond instead to the more general case including both intrasubband and intersubband scattering. Dashed lines correspond to the fitting.

### 5.3.3 Effect of the intrasubband intravalley scattering approximation

Let us compare results obtained by means of the FB approach with those computed following Ref. [21] (approximation IIS). Figs. 5.11a-b-e-f show the FB intrasubband momentum relaxation rates for the lowest subband of a 1.12 nm-wide GNR limited by in-plane LA and LO modes and accounting for both ABS and EM processes. In particular, we show results obtained by means of the FB model and taking into account only intravalley 0-th order phonons ( $q_{y\beta} = 0$ , red solid curves) as well as higher order phonons ( $q_{y\beta} \neq 0$ , violet solid curves). Rates obtained within approximation IIS by exploiting Eqs. (C.1) are also plotted (black solid curves), adopting the sound speed  $v_{LA}$  ( $\approx 20700$  m/s) for the 0-LA mode and optical energy offset  $E_{LO}$  ( $\approx 187.2$  meV). As can be seen, by considering only 0-th order phonons, the FB approach and approximation IIS fairly agree up to 0.2-0.4 eV far from the bottom of subband  $E_C$ .

However, by considering in the FB the uncertainty in the transverse momentum conservation, i.e. higher order phonons (violet solid curves), the agreement worsens even near  $E_C$ , especially for emission of

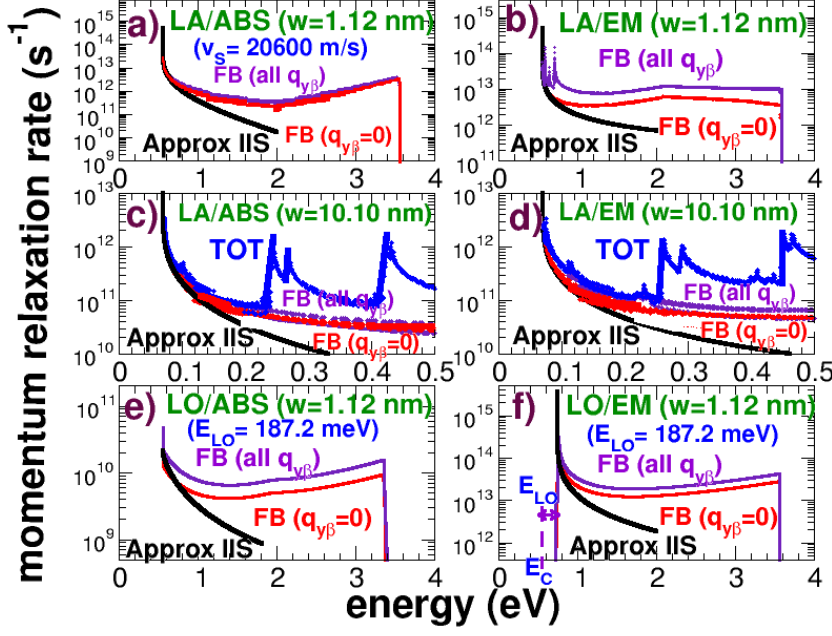


Figure 5.11: Intracubband scattering rates for ABS and EM processes of LA and LO modes obtained by means of the FB approach (Eqs. (5.15) and (5.18)) for the lowest conduction subband for  $W = 1.12$  nm ((a)-(b)-(e)-(f)) and  $10.10$  nm ((c)-(d)), considering only 0-th order phonons (red curves) and also higher order phonon modes (violet curves). Scattering rates obtained by employing the approximation IIS [Eqs. (C.1)] are also shown (black curves). In (c) and (d) we also report the total (intracubband + intersubband) scattering rate limited by LA phonons.

AC phonons and transitions involving intervalley OP phonons. In addition, in Figs. 5.11b the FB rates exhibit few peaks near  $E_C$  due to inelasticity. In Figs. 5.11c-d we report the same quantities for a 10 nm-wide ribbon as well as the total LA scattering rate. As expected, since the form factor  $G$  tends to a Dirac delta as soon as  $W$  increases, the impact of the transverse momentum conservation uncertainty on rate is weaker. Instead, unlike 1 nm-wide GNRs, intersubband scattering (blue curves) is important even at energies relatively close to  $E_C$ .

### 5.3.4 Low-field GNR phonon-limited mobility and mean free path

Let us now introduce the low-field intrinsic mobility  $\mu_{in}$ . We remark that, although in this chapter  $\mu_{in}$  has been computed by means of Eqs. (5.29) and (5.30), the Mathiessen rule

$$\frac{1}{\mu_{Math}} = \frac{1}{\mu_{AC}} + \frac{1}{\mu_{OP}} \quad (5.32)$$

has been verified to hold for all the considered carrier densities  $n_{2D}$  [97], as shown in Fig. 5.12a, where we show the module of the relative error of the Mathiessen rule  $\mu_{Math}$ . We would like also to point out that, although the degeneracy factor  $[1 - f(E_{\mathbf{k}})]/[1 - f(E_{\mathbf{k}})]$  in Eqs. (5.15) and (5.18) has been rarely considered in the literature [137], when taken into account, for  $n_{2D} \geq 10^{12} \text{ cm}^{-2}$  it leads to differences up to 30% with increasing  $n_{2D}$  and  $W$ , due to the increase number of subbands contributing to transport (Fig. 5.12b).

The general assumption made when studying mobility in GNRs is that forward scattering ( $\alpha = 0$ ) is neglected [21]. Here we want to verify such assumption. In particular, FB phonon-limited mobility for  $W = 4.86 \text{ nm}$  and  $10.10 \text{ nm}$  is shown in Figs. 5.13a-b by including only backscattering (B) and backward + forward scattering (B+F) processes. Scattering rates corresponding to absorption and emission of AC phonons for both B and B+F are instead plotted in Figs. 5.13c-f ( $n_{2D} = 9 \times 10^{12} \text{ cm}^{-2}$ ). As can be seen, the contribution to  $1/\tau$  due to forward scattering can be reasonably neglected up to  $W = 10.10 \text{ nm}$ , therefore phonon-limited mobility is mainly degraded by backward scattering (Figs. 5.13a-b).

Low-field mobility  $\mu_{in}$  is shown in Fig. 5.14a as a function of the electron density  $n_{2D}$  for different widths. Results obtained through DFT calculations for 2D suspended graphene sheet [24] are also reported.  $\mu_{in}$

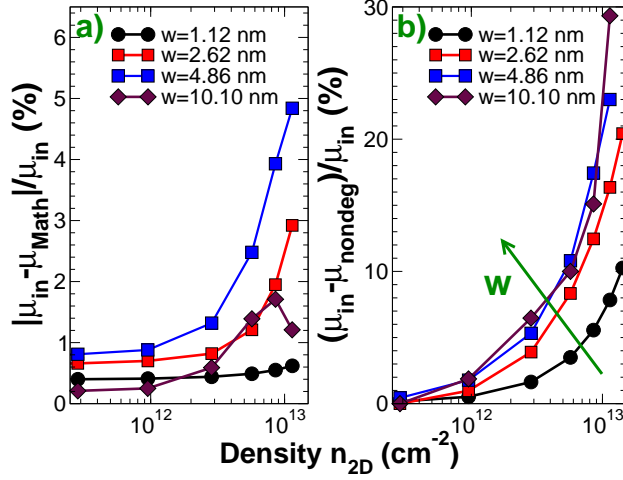


Figure 5.12: (a) Module of the relative error  $|\mu_{in} - \mu_{Math}|/\mu_{in}$  [Eqs. (5.29), (5.30)) and (5.32)]. (b) Percentage difference  $(\mu_{in} - \mu_{nondeg})/\mu_{in}$ , where  $\mu_{nondeg}$  is obtained by neglecting the degeneracy factor  $[1 - f(E_{\mathbf{k}}')]/[1 - f(E_{\mathbf{k}})]$  in Eqs. (5.15) and (5.18).

close to  $500 \text{ cm}^2/\text{Vs}$  is found for 1 nm-wide GNR, exceeding by almost one order of magnitude the experimental mobility of GNRs [12, 18] and the intrinsic phonon-limited mobility of silicon nanowires [138] of comparable size [96]. We find that  $\mu_{in}$  is mainly limited by backward scattering involving AC phonons, due to the large mode-dependent OP energy offset ( $\approx 130\text{-}160 \text{ meV}$ ) [136]. Unlike in two-dimensional graphene, where  $\mu_{in} \propto 1/n_{2D}$  [26], the lateral confinement in GNRs leads to a non-monotonic  $n_{2D}$ -dependence as also observed in CNTs [139] (Fig. 5.14a). For small  $W$ ,  $\mu_{in}$  increases with  $n_{2D}$ , due to the reduction of final states available for scattering. For wider GNRs biased in the inversion regime, electrons can populate excited subbands opening additional channels for scattering, thus reducing  $\mu_{in}$ . As can be seen, mobility in GNR is much smaller than  $\mu_{in}$  in graphene [24] (Fig. 5.14a).

The mean free path in the first subband  $\langle L_{\mathbf{k}} \rangle$  is shown in Fig. 5.14b as a function of  $n_{2D}$ , where  $\langle L_{\mathbf{k}} \rangle \equiv \langle v(\mathbf{k}) \tau(\mathbf{k}) \rangle$ ,  $v(\mathbf{k})$  is the group velocity and the expectation value  $\langle \cdot \rangle$  has been computed in the Brillouin zone,

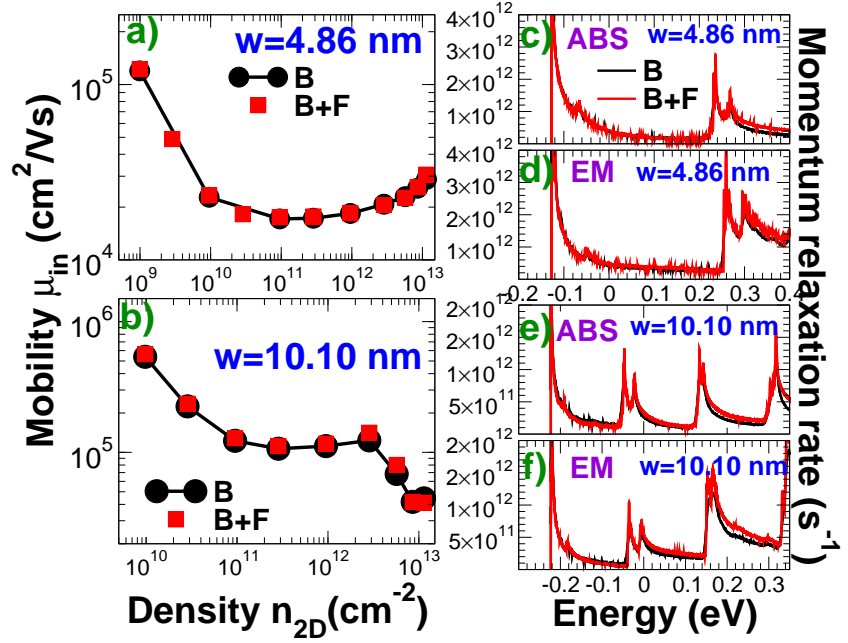


Figure 5.13: Full-band mobility  $\mu_{in}$  as a function of  $n_{2D}$  computed including only backward (B) and both backward and forward scattering (B+F) for  $W = 4.86 \text{ nm}$  (a) and  $10.10 \text{ nm}$  (b). (c)-(f): momentum relaxation rates corresponding to absorption (ABS) and emission (EM) of AC phonons calculated for B and B+F for the first conduction subband of  $4.86 \text{ nm}$  and  $10.10 \text{ nm}$ -wide GNRs.  $n_{2D} = 9 \times 10^{12} \text{ cm}^{-2}$ .



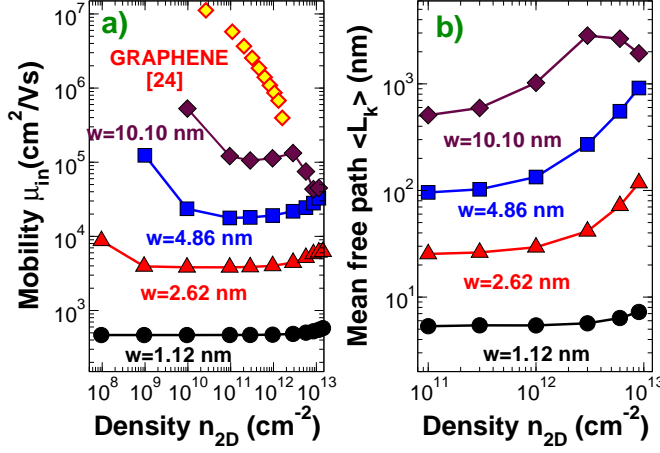


Figure 5.14: (a)  $\mu_{in}$  and (b)  $\langle L_k \rangle$  for an electron in the lowest subband as a function of  $n_{2D}$  for different  $W$ . DFT calculations [24] for graphene are also shown in (a).

considering  $f(1 - f)$  as the distribution function [136]:

$$\langle L_k \rangle = \frac{\int_{-k_F}^{k_F} dk_x v(\mathbf{k}) \tau(\mathbf{k}) f(E_k) (1 - f(E_k))}{\int_{-k_F}^{k_F} dk_x f(E_k) (1 - f(E_k))}. \quad (5.33)$$

At  $T = 300$  K,  $\langle L_k \rangle$  is of the order of few  $\mu m$  for larger GNRs in the inversion regime, as expected in graphene flakes, while it is  $\approx 10$  nm for narrower GNRs (Figs. 5.14b). In addition,  $\langle L_k \rangle$  shows a non-monotonic behaviour as a function of  $n_{2D}$ , as  $\mu_{in}$ .

Figs. 5.15a-b show  $L_k$  as a function of  $E_k$  and  $\langle L_k \rangle$  as a function of  $W$  in the strong inversion regime ( $n_{2D} = 9 \times 10^{12} \text{ cm}^{-2}$ ) for the lowest four conduction subbands.  $L_k$  exhibits a strong energy dependence, with a wide maximum at low energies, but electrons placed in the first subband can be injected in the GNR channel even at high energies, with  $L_k \approx 1$  nm or larger (Fig. 5.15a). As can be noted in Fig. 5.15b,  $\langle L_k \rangle$  increases about two orders of magnitude with  $W$ , saturating to few  $\mu m$  for the wider GNRs. However it can be of the order of few nanometers (Fig. 5.15b) for narrower GNRs, far from the ballistic assumption generally made for ultrashort devices. Note that these values are at least a factor of 10 lower than those in Ref. [118], where only the contribution to

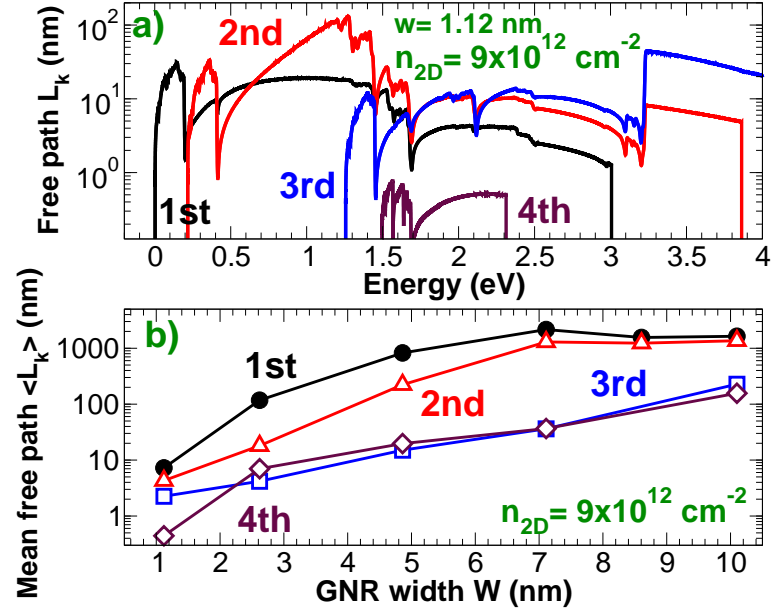


Figure 5.15: (a): free path  $L_k$  as a function of the electron energy for  $W = 1.12$  nm. (b): mean free path  $\langle L_k \rangle$  as a function of  $W$ . Data for the lowest four conduction subbands are shown.  $n_{2D} = 9 \times 10^{12} \text{ cm}^{-2}$ .

electron-phonon coupling due to the phonon-induced modulation of the hopping parameter has been considered, completely neglecting the local change of the electron spectrum due to the lattice distortions induced by phonons, i.e. the deformation potential contribution [109].

### 5.3.5 Effect of temperature

In Fig. 5.16a,  $\mu_{in}$  is plotted as a function of temperature  $T$ . Similarly to what has been observed in small-diameter CNTs [140], in narrow GNRs the dependence on  $W$  and  $T$  can be expressed by means of the empirical relation

$$\mu_{in}(W, T) = \mu_0 \frac{300 \text{ K}}{T} \left( \frac{W}{1 \text{ nm}} \right)^{\alpha_{AC}}, \quad (5.34)$$

where  $\mu_0 \approx 391 \text{ cm}^2/\text{Vs}$  and  $\alpha_{AC} = 2.65$ , which is close to  $\mu_{in} \propto W^3$  expected for narrow GNRs, since [see Eq. (5.29)]

$$\mu_{in} \propto \frac{\tau}{W \times DOS} \propto \frac{1}{G \times DOS^2} \quad (5.35)$$

and  $G \propto 1/W^2$  and the density of states  $DOS \propto 1/\sqrt{W}$  [96]. Of course, for large  $W$ ,  $\mu_{in}$  saturates to that of 2D graphene. Since AC in-plane phonons scattering is dominant and  $n_{\mathbf{q}}^- \approx kT/\hbar\omega$  for  $kT \gg \hbar\omega$ ,  $\mu_{in}$  is inversely proportional to  $T$  (Fig. 5.16a). In addition,  $\langle L_{\mathbf{k}} \rangle \propto 1/T$ , as  $\mu_{in}$  (Figs. 5.16b).

### 5.3.6 Acoustic and optical phonon-limited mobility

Figs. 5.17a-d show the FB mobility limited by LA modes ( $\mu_{AC}$ ) and mobilities computed within the approximation IIS [21], IISNS and 2DPNS [130] ( $\mu_{AC}^{IIS}$ ,  $\mu_{AC}^{IISNS}$  and  $\mu_{AC}^{2DPNS}$ , respectively). For a fair comparison, as in Figs. 5.11a-f, the very same phonon parameters of the FB approach ( $D_{AC}$ , as well as  $v_{LA}$ ) are exploited. Four different values of  $W$  are taken into account. As can be seen in Figs. 5.17a-c, the agreement between  $\mu_{AC}$  and  $\mu_{AC}^{IIS}$  is satisfactory in narrow GNRs, since intravalley intrasubband scattering represents the dominant limiting factor and the low-field mobility is affected by electrons with energies close to  $E_C$ . Discrepancies mainly derive from the disagreement found in the emission rates (Figs. 5.11c-d).

However, the agreement worsens with increasing  $W$ . As can be observed in Fig. 5.17d, a FB approach is required for wider ribbons: indeed,

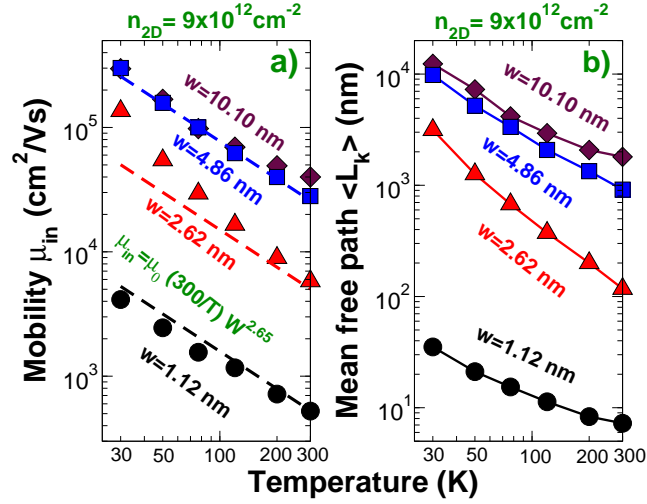


Figure 5.16: (a) mobility  $\mu_{in}$  and (b) mean free path  $\langle L_k \rangle$  for the lowest subband as a function of  $T$  for different  $W$ . In (a) dashed lines correspond to the empirical formula for  $\mu_{in}(W, T)$ .

within approximation IIS, mobility can be overestimated up to a factor of 7 for  $n_{2D} \approx 1.5 \times 10^{13} \text{ cm}^{-2}$  and  $W = 10.10 \text{ nm}$ . As already observed when discussing Figs. 5.11, such differences are mainly due to the activation of intersubband scattering, which becomes more severe as soon as the energy separations between subbands decreases. When neglecting the spinor, mobility  $\mu_{AC}^{IISNS}$  is suppressed by a factor of almost 1.4 with respect to  $\mu_{AC}^{IIS}$  for 1 nm-wide GNRs, and increasing up to a factor 10 or larger for  $W = 10.10 \text{ nm}$  and high  $n_{2D}$ . In addition,  $\mu_{AC}^{IISNS}$  can underestimate  $\mu_{AC}$  up to a factor 3 for wide ribbons in the inversion regime, which means that spinor cannot be neglected. For what concerns  $\mu_{AC}^{2DPNS}$ , the adoption of a 2D model for the phonon system clearly fails: we obtain an underestimation of  $\mu_{AC}$  by a factor of  $\approx 2$  even for narrow GNRs, increasing up to  $\approx 5$  for the larger considered widths.

As can be noted in Figs. 5.17a-d,  $\mu_{in} \approx \mu_{AC}$ . Indeed, like  $\mu_{in}$ ,  $\mu_{AC}$  of 1 nm-wide ribbons is close to  $500 \text{ cm}^2/\text{Vs}$ , some orders of magnitudes smaller with respect to 2D graphene [5, 141]. In addition, as already observed for  $\mu_{in}$ , size effects leads to a non-monotonic  $n_{2D}$ -dependence of  $\mu_{AC}$ .

Figs. 5.18a-d show the FB mobility limited by TO ( $\mu_{TO}$ ) and LO

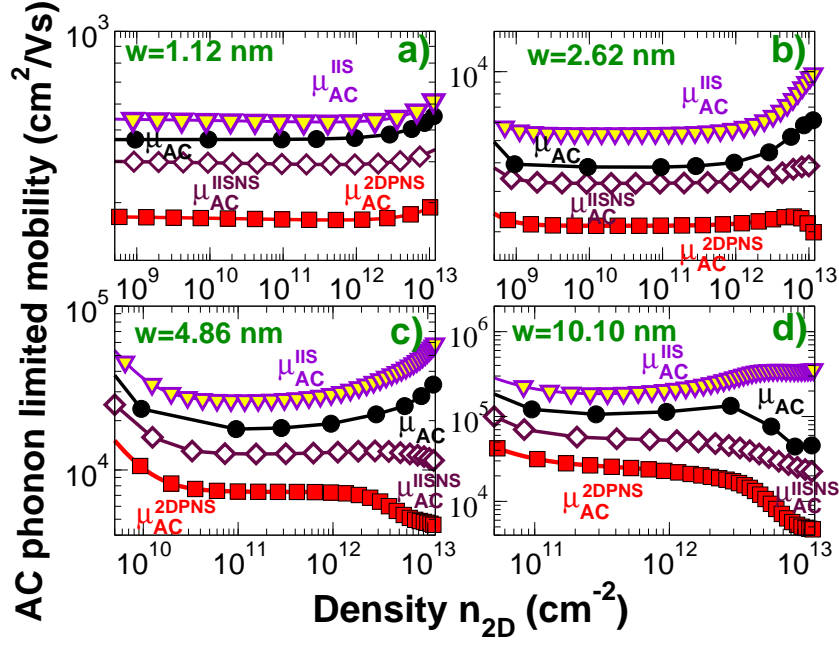


Figure 5.17: LA phonon-limited mobility  $\mu_{AC}$  obtained by exploiting the FB approach. The mobilities  $\mu_{AC}^{IIS}$ ,  $\mu_{AC}^{IISNS}$  and  $\mu_{AC}^{2DPNS}$  calculated following the approximation IIS, IISNS and 2DPNS are also shown. Four different GNR widths  $W$  have been considered: (a)  $W = 1.12 \text{ nm}$ , (b)  $W = 2.62 \text{ nm}$ , (c)  $W = 4.86 \text{ nm}$  and (d)  $W = 10.10 \text{ nm}$ .

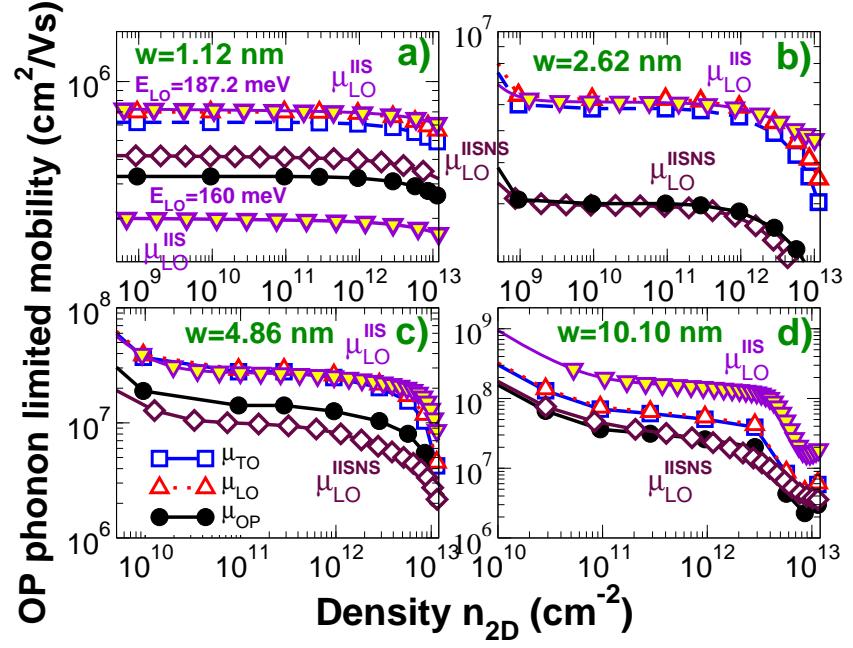


Figure 5.18:  $\mu_{OP}$ ,  $\mu_{LO}$  and  $\mu_{TO}$  obtained by exploiting the FB approach. The mobilities  $\mu_{LO}^{IIS}$  and  $\mu_{LO}^{IISNS}$  computed by means of the approximations IIS and IISNS are also plotted. Four different values of GNR widths  $W$  have been considered: (a)  $W = 1.12$  nm, (b)  $W = 2.62$  nm, (c)  $W = 4.86$  nm and (d)  $W = 10.10$  nm. In (a) two different set of phonon parameters are used for  $\mu_{LO}^{IIS}$ .

( $\mu_{LO}$ ) modes, the total FB mobility limited by OP phonons ( $\mu_{OP}$ ) and the mobilities calculated by using the approximation IIS ( $\mu_{LO}^{IIS}$ ) and IISNS ( $\mu_{LO}^{IISNS}$ ), for  $E_{LO} = 187.2$  meV (and 160 meV [21] for  $\mu_{LO}^{IIS}$  in Fig. 5.18a). Four different values of  $W$  are considered.  $\mu_{OP}$  is roughly 3 order of magnitude larger than  $\mu_{AC}$  (Figs. 5.18a-d). We note that for OP phonons the agreement between  $\mu_{LO}$  and  $\mu_{LO}^{IIS}$  calculated for  $E_{LO} = 160$  meV (Fig. 5.18a, violet downwards triangles) is poor. Good results are instead obtained when using  $E_{LO} = 187.2$  meV (Fig. 5.10), and  $\mu_{LO}^{IIS} \approx \mu_{LO}$  for narrow GNRs (Figs. 5.18a-c). As already found for acoustic phonons, the neglect of spinor ( $\mu_{LO}^{IISNS}$ ) fails to quantitatively reproduce  $\mu_{LO}$ : indeed it yields underestimation of mobility ranging from  $\approx 2$  to 5.

### 5.3.7 Remote phonon-limited mobility

The SO phonon-limited mobility  $\mu_{ex}$  as a function of  $n_{2D}$  is shown in Figs. 5.19a-b for  $W$  smaller than 10 nm, considering GNRs deposited both on SiO<sub>2</sub> and on HfO<sub>2</sub>. As in graphene [22, 26], the higher the dielectric constant, the larger the mobility suppression due to SO phonon scattering. In particular, we observe  $\mu_{ex}$  down to 700 cm<sup>2</sup>/Vs for SiO<sub>2</sub> (Fig. 5.19a) and 60 cm<sup>2</sup>/Vs for HfO<sub>2</sub> (Fig. 5.19b), due to the smaller energy offset of the emission processes. As in CNTs [111],  $\mu_{ex} \propto W^{\alpha_{SO}}$  with  $\alpha_{SO}$  ( $\approx 1.4$ -1.6) dependent on  $n_{2D}$  and smaller than  $\alpha_{AC}$ . Let us stress the fact that including screening when evaluating  $\mu_{ex}$  is compulsory, since it has a significant effect for  $n_{2D} \geq 10^{11}$  cm<sup>-2</sup>, as can be seen in Figs. 5.19a-b for  $W < 5$  nm, where  $\mu_{ex}$  increases with electron concentration. In addition, for SiO<sub>2</sub>  $\mu_{ex}$  tends to saturate for the Fermi level  $E_F > E_C$  (Fig. 5.19a), since  $DOS(E_F)$  decreases with  $E_F$ , and  $\mathcal{L}(Q_x \rightarrow 0) \propto DOS(E_F)$  [107]. Although the very same considerations holds for sub-5 nm GNRs on HfO<sub>2</sub>, in this case  $\mu_{ex}$  continues to increase due to the much weaker impact of screening on  $1/\tau$  (Fig. 5.19b).

Comparing Figs. 5.19a-b with Fig. 5.14a, it can be observed that SO phonons are predominant for  $n_{2D} < 10^{12}$  cm<sup>-2</sup> in SiO<sub>2</sub>, and for all  $n_{2D}$  densities on HfO<sub>2</sub> [96]. Comparison with measurements on GNRs deposited on SiO<sub>2</sub> [12] reveals that  $\mu_{ex}$  is larger up to one order of magnitude, showing that fabrication technology improvement could lead to a tenfold increase in mobility, once the present dominant scattering mechanisms (e.g. LER) are suppressed. However,  $\mu_{ex}$  is larger at least by a factor of  $\approx 3$  with respect to experiments for 10-nm-wide GNRs deposited with ultrathin HfO<sub>2</sub> dielectric [115] (Fig. 5.19b), maybe due

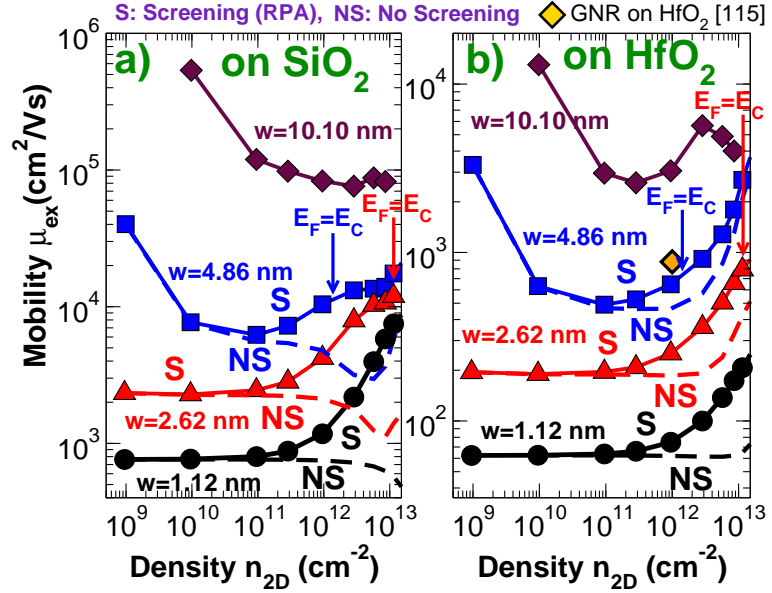


Figure 5.19:  $\mu_{ex}$  as a function of  $n_{2D}$  for GNR deposited (a) on  $\text{SiO}_2$  and (b) on  $\text{HfO}_2$ . Results for  $W < 5$  nm obtained neglecting electron screening (NS) and considering quasi-1D screening (S) are shown. For 10 nm-wide GNRs on  $\text{SiO}_2$  and  $\text{HfO}_2$ , 2D screening is considered. Results for 10 nm-wide GNRs on  $\text{HfO}_2$  [115] are also plotted in (b). The carrier density for which the Fermi level  $E_F$  is almost aligned to the bottom  $E_C$  of the first subband is also shown.



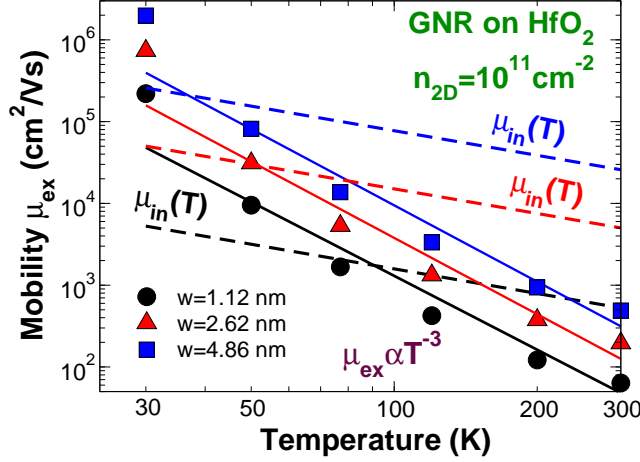


Figure 5.20: Mobility  $\mu_{ex}$  for GNR on  $\text{HfO}_2$  as a function of  $T$  for different  $W$ . Dashed lines correspond to the empirical formula (5.34) for  $\mu_{in}(W, T)$  and solid lines to the fit for  $\mu_{ex}$ .  $n_{2D} = 10^{11} \text{ cm}^{-2}$ .

to the presence of additional scattering sources in the state-of-the-art GNRs.

As can be noted in Fig. 5.20 and as it also occurs in CNTs deposited on polar dielectrics [111],  $\mu_{ex} \propto 1/T^\gamma$ . In particular, for  $\text{HfO}_2$ ,  $\gamma \approx 3$ . Since  $\mu_{in} \propto 1/T$ , SO phonon scattering dominates transport roughly above 100 K for all  $W$  (Fig. 5.20), as for CNTs on  $\text{SiO}_2$  [111].

### 5.3.8 Comparison with results present in the literature

In this section, we will compare our results with experiments and simulations present in the literature. In particular, in Fig. 5.21a we show  $\mu_{in}$  as a function of  $W$  computed by means of FB simulations as well as  $\mu_{in}$  obtained in Refs. [21, 88] exploiting different set of phonon parameters ( $n_{2D} = 10^{12} \text{ cm}^{-2}$ ). As can be seen, FB leads to results really different as compared to those reported in the literature. In particular, in the worst case (approximation 2DPNS, set B) GNR mobility is underestimated by a factor of  $\approx 2.5$  for narrow ribbons, whereas for larger GNRs ( $W \geq 5$ ) the approximation IIS ( $D_{AC} = 14 \text{ eV}$ ) is able to accurately reproduce the FB results. Note also that the assumption of 2D phonons

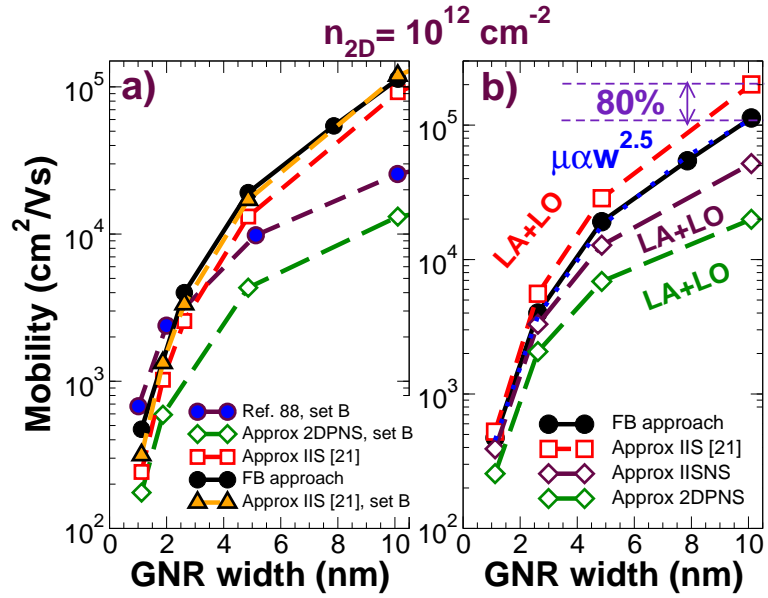


Figure 5.21: (a) Mobility  $\mu_{in}$  as a function of  $W$  for different models and exploiting different set of phonon parameters. The set B [88]  $E_{ph}^{LO} = 160 \text{ meV}$ ,  $D_{AC} = 14 \text{ eV}$ ,  $D_{OP} = 10^{11} \text{ eV/m}$  has been used by Ref. [88] and within the approximations IIS and 2DPNS. Results calculated following the approximation IIS (parameters from Ref. [21]) and by means of the FB approach are also shown. (b) Mobility as a function of  $W$  for the FB approach and approximations IIS, IISNS and 2DPNS, and exploiting in the latter three cases phonon parameters calculated by using the FB approach. Blue dotted line refers to the fit of  $\mu_{in}$ .  $n_{2D} = 10^{12} \text{ cm}^{-2}$ .

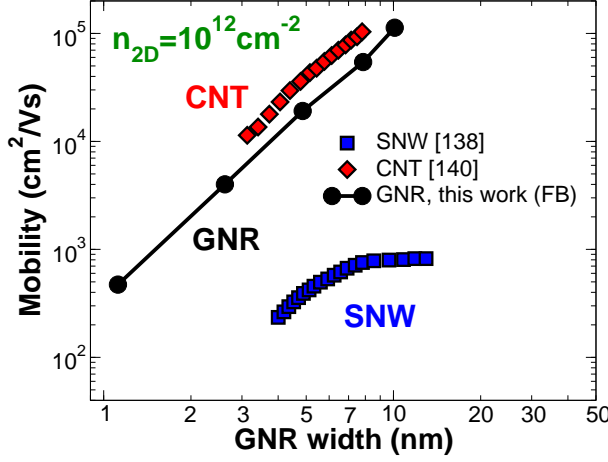


Figure 5.22: Mobility as a function of  $W$  for different quasi-1D devices: GNR, CNT and SNW. Results from simulations (intrinsic mobility) for CNT [140], SNW [138] and our calculated data for the intrinsic GNR phonon-limited mobility are shown.  $n_{2D} = 10^{12} \text{ cm}^{-2}$ .

(approximation 2DPNS) leads to a slope of  $\mu_{in}(W)$  in qualitative agreement with Ref. [88], where a 2D model is implemented neglecting the spinor.

In particular, in order to make a fair comparison, we have also calculated results following the approximation IIS, IISNS and 2DPNS by exploiting the same phonon parameters as in FB (Fig. 5.21b). As can be noted, approximation IIS [21] is in very good agreement with FB results for narrow GNR, since, as expected, intravalley intrasubband scattering dominates transport. However, when increasing  $W$  it tends to overestimate mobility up to 50% for 5 nm-wide GNRs and up to 80% for 10 nm-wide GNRs, when intersubband scattering is dominant. The situation even worsens for  $n_{2D} > 10^{12} \text{ cm}^{-2}$ . We also remark that the spinor has to be properly included in a transport model: indeed approximation IISNS [130] underestimates mobility up to 100% for 10 nm-wide GNRs. A two-dimensional phonon model (approximation 2DPNS) is instead inappropriate for all the considered  $W$ , underestimating mobility up to a factor of 5 for  $W = 10.10 \text{ nm}$  [97].

In Fig. 5.22, for a carrier density  $n_{2D} = 10^{12} \text{ cm}^{-2}$ ,  $\mu_{in}$  is compared with the intrinsic mobility of CNTs [140] and SNWs [138] obtained by

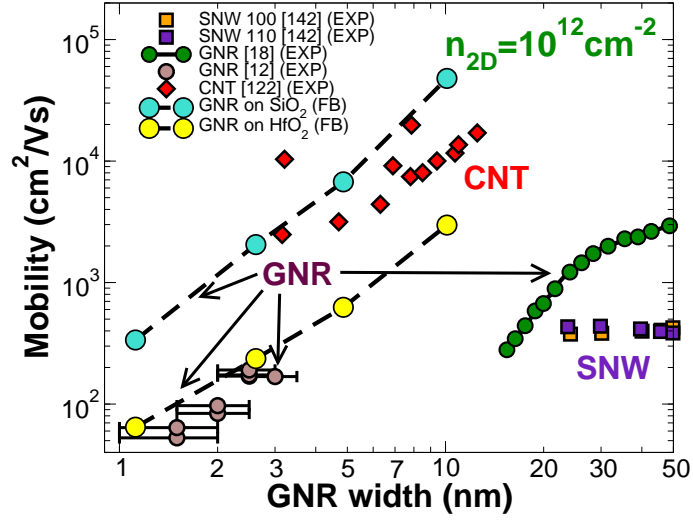


Figure 5.23: Mobility as a function of  $W$  for different quasi-1D devices: GNR, CNT and SNW. Results from experiments for quasi-1D devices deposited on  $\text{SiO}_2$  [12, 18, 122, 142] (EXP), and our calculated data for the FB phonon-limited mobility of GNR on  $\text{SiO}_2$  and on  $\text{HfO}_2$  are shown.  $n_{2D} = 10^{12} \text{ cm}^{-2}$ .

means of simulations. As can be seen, transverse confinement leads to a mobility degradation slightly stronger than that of CNTs with the same number of dimer lines  $l$  (i.e. with a comparable energy gap), but the intrinsic mobility is still much higher than that of narrow SNWs [138].

In Fig. 5.23 the FB phonon-limited mobility of GNRs on  $\text{SiO}_2$  is compared with experiments available for quasi-1D devices: results for GNRs [12, 18], CNTs [122] and Silicon NanoWires (SNW) [142] on the same insulator are shown. As can be seen, GNR phonons are not the most limiting factor in the state-of-the-art GNRs.

Indeed, it is important to observe that even when depositing GNRs on  $\text{SiO}_2$ , phonon-limited mobility is still a factor 5 higher than that observed in the state-of-the-art GNRs on the same insulator [12, 18] (Fig. 5.23). However deposition on high- $k$  oxides, such as  $\text{HfO}_2$ , strongly degrades the intrinsic mobility by a factor of 10, therefore losing all the advantages with respect to SNW-based technology [142] (Fig. 5.23).

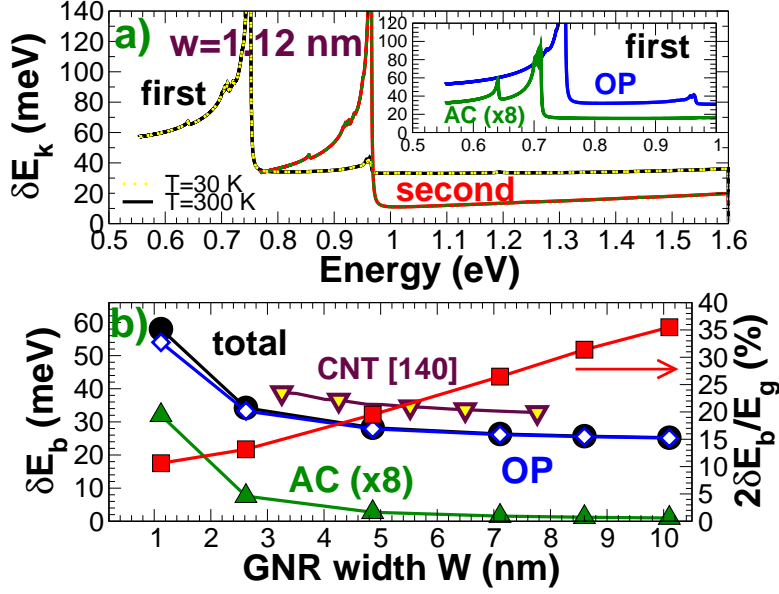


Figure 5.24: (a) Polaronic energy shift  $\delta E_k$  as a function of the energy  $E_k$  for the first two subbands ( $W = 1.12$  nm). Solid curves correspond to  $T = 300$  K, dotted curves to  $T = 30$  K. Inset: OP and AC ( $\times 8$ ) contributions to  $\delta E_k$  for the first subband. (b): Polaronic binding energy  $\delta E_b$  (left) and polaronic correction to the band gap  $2\delta E_b/E_g$  (right) as a function of  $W$ . Results for CNTs [140] are also reported.

### 5.3.9 Polarons in armchair GNRs

Now we focus on the polaronic energy shift  $\delta E_k$  due to the electron-phonon coupling, computed exploiting the second-order perturbation theory [140]:

$$\begin{aligned}
 \delta E_k &= \lim_{\delta \rightarrow 0} \text{Re} \sum_j \sum_{\mathbf{k}', \mathbf{q}} \frac{|\langle n_{\mathbf{q}} \mp 1, \Psi_{\mathbf{k}'}(\mathbf{r}) | H_{e-ph} | n_{\mathbf{q}}, \Psi_{\mathbf{k}}(\mathbf{r}) \rangle|^2}{E_{\mathbf{k}} - E_{\mathbf{k}'} \pm E_{ph}(\mathbf{q}) - i\delta} \\
 &= \lim_{\delta \rightarrow 0} \text{Re} \sum_j \sum_{\beta, \eta'} \int_{-k_F}^{k_F} dq_x \frac{1}{4\pi} G_{\eta, \eta', \beta} M_{\mathbf{q}}^2 (1 + \cos \theta_{\mathbf{k}\mathbf{k}'}) \cdot \\
 &\quad \cdot \left[ \frac{n_{\mathbf{q}}^- + 1/2 \mp 1/2}{E_{\mathbf{k}} - E_{k_x \pm q_x, k_{y\eta'}} \pm E_{ph}^{j\beta}(q_x, q_{y\beta}) - i\delta} \right], \quad (5.36)
 \end{aligned}$$

where  $M_{\mathbf{q}} = D_j \sqrt{\hbar^2 / (2\rho W E_{ph,q_x}^{j\beta})}$  in the DPA [129] and  $E_{\mathbf{k}}, E_{\mathbf{k}'}$  are unperturbed electron energies.

Fig. 5.24a shows  $\delta E_{\mathbf{k}}$  as a function of  $E_{\mathbf{k}}$  for the lowest two subbands for the  $W = 1.12$  nm case.  $\delta E_{\mathbf{k}}$  is weakly energy dependent near the cutoff subband, is independent on  $T$  and increases sharply in correspondence of intersubband transitions. As in CNTs [140], OP phonons mostly contribute to  $\delta E_{\mathbf{k}}$  (inset of Fig. 5.24a). Instead, unlike in CNTs [140], AC phonons leads to few peaks due to the transverse momentum conservation uncertainty (inset of Fig. 5.24a). The polaronic binding energy  $\delta E_b = \delta E_{\mathbf{k}}(E_{\mathbf{k}} = E_{C1})$  is almost 59 meV for 1 nm-wide GNRs, close to that obtained for semiconducting CNTs with the same number of dimer lines  $l$  [140] (Fig. 5.24b) and corresponds to a band gap renormalization  $2\delta E_b \approx 118$  meV for 1-nm nanoribbons, and to a relative correction of -35% of the energy gap  $E_g$  of 10-nm nanoribbons [96] (Fig. 5.24b).

## 5.4 Concluding remarks

In summary, in this chapter we have proposed a very accurate full-band approach to evaluate low-field phonon-limited mobility  $\mu_{in}$  in GNRs including all the relevant aspects which have been often neglected in previous works: (i) inclusion of all in-plane phonon modes contributing to the coupling through the dominant deformation potential term (LA, LO and TO), (ii) inclusion of the intersubband scattering, (iii) the uncertainty in the transverse momentum conservation and (iv) of the spinor. Through comparison with few GNR models published in the literature [21, 88] and with experimental results for quasi-1D devices [12, 18, 122, 142], some main learnings have been inferred.

First, a FB treatment of electrons and phonons is essential in order to obtain accurate results, since, by only including LA intravalley phonons [21], intrinsic mobility for a carrier density  $n_{2D} = 10^{12} \text{ cm}^{-2}$  can be overestimated more than 50% for GNR width  $W \geq 5$  nm, due to the large contribution of intervalley intersubband phonon scattering for the wider ribbons. The inclusion of spinor is also mandatory, since even neglecting both the spinor and intersubband scattering, the FB mobility is underestimated up to a factor of 3 in 10 nm-wide ribbons and up to a factor 10 with respect to the intrasubband scattering case. A 2D phonon model neglecting the spinor is also inadequate, since it can underestimate FB mobility by up to a factor 5. We have also shown that forward scattering can be reasonably neglected for width up to  $W = 10$  nm. A very

smooth dependence of the optical energy offset on the GNR widths is also found, with values in good agreement with those appeared in the literature. If one neglects the degeneracy factor, as very often happens in literature, electron mobility can be underestimated up to 30%.

$\mu_{in}$  is close to 500 cm<sup>2</sup>/Vs in suspended 1 nm-wide GNRs at room temperature, and it is suppressed down to 60 cm<sup>2</sup>/Vs in 1 nm-wide GNR deposited on HfO<sub>2</sub>, due to SO phonons coupling. The resulting mean free paths range from 1 to 10 nm, undermining the possibility of performing ballistic or coherent transport experiments at room temperature. Whereas suspended 2D graphene has an intrinsic mobility at room temperature several orders of magnitude larger than that of bulk semiconductors, narrow GNRs with reasonable semiconducting gap have only slightly larger mobility than comparable silicon nanowires. Finally, we have also found polaron formation in armchair GNRs, with a remarkable band gap renormalization of up to 35% in the case of 10 nm-wide ribbons.





## Appendix A

# Alternative derivation of the shot noise formula

In this Appendix we use an alternative approach in order to compute an approximate formula for the shot noise power spectral density [57]. Such approach is independent of the second quantization formalism and therefore it does not take into account the fact that electrons are identical fermions.

Let us introduce some quantities. In particular  $\sigma_{Sm}$  ( $\sigma_{Dm}$ ) is the random occupation at source S (drain D) contact for the mode  $m$ : it can be either 0 or 1, with a mean value equal to the Fermi occupation factor for the source (drain) contact  $f_S$  ( $f_D$ ). Equivalently, we can define the source-to-drain (drain-to-source) trasmission occurrence  $\Omega_{mn}$  ( $\Omega'_{mn}$ ) from mode  $n$  to  $m$ , whose mean value is equal to  $\mathcal{T}_{mn}$  ( $\mathcal{T}'_{mn}$ ), the transmission coefficient from mode  $n$  to  $m$ . For the CNT-FET structure, the index  $m$  and  $n$  run along all the transverse modes, the energies and the spin, while for the SNWT structure they also run along the six equivalent minima of the conduction band in the  $\mathbf{k}$  space. From a computational point of view,  $\sigma_{Sm}$  ( $\Omega_{mn}$ ) is obtained by extracting a random number  $\mathfrak{R}$  with uniform distribution between 0 and 1: if  $\mathfrak{R} < f_S(E)$  ( $\mathfrak{R} < \mathcal{T}_{mn}(E)$ ) then  $\sigma_{Sm} = 1$  ( $\Omega_{mn} = 1$ ), otherwise  $\sigma_{Sm} = 0$  ( $\Omega_{mn} = 0$ ). The statistical average of random occupation and trasmission occurrences can be

synthesized as follows ( $\alpha \in \{S, D\}$ ,  $l \in \alpha$ ):

$$\begin{aligned}\langle \sigma_{\alpha m} \rangle &= f_{\alpha} \quad ; \quad \langle \sigma_{\alpha m}^2 \rangle = f_{\alpha} \\ \langle \Omega_{mn} \rangle &= \mathcal{T}_{mn} \quad ; \quad \langle \Omega_{mn}^2 \rangle = \mathcal{T}_{mn} \\ \langle \Omega'_{mn} \rangle &= \mathcal{T}'_{mn} \quad ; \quad \langle \Omega'^2_{mn} \rangle = \mathcal{T}'_{mn}\end{aligned}$$

Of course, in the self-consistent computation of the electrostatic and transport equations, transmission occurrences depend on random occupations at both reservoirs:

$$\Omega_{mn} = \Omega_{mn} \{ \sigma_{S1}, \sigma_{S2}, \dots, \sigma_{D1}, \sigma_{D2}, \dots \}. \quad (\text{A.1})$$

Indeed, although transmission events and occupancy of incoming states are independent events, the probability that the transmission event occurs is affected by the occupation of the initial and final states through Pauli's exclusion principle. Starting from the two-terminal Landauer formula [35], the randomized current can be expressed as:

$$I = \frac{e dE}{2\pi\hbar} \sum_{m \in S} \sum_{n \in D} \left[ \sigma_{Sm} \Omega_{nm} - \sigma_{Dn} \Omega'_{mn} \right] \quad (\text{A.2})$$

where  $dE$  is the energy step and  $e$  is the elementary charge.

In order to compute the statistical average of the current, we have to perform mean products between two stochastic variables ( $A$  and  $B$  in the following):

$$\begin{aligned}\langle A B \rangle &= \int \int A B P(A) P_{1|1}(B | A) dB dA \\ &= \int A \bar{B}(A) P(A) dA \\ &= \langle A \bar{B}(A) \rangle\end{aligned} \quad (\text{A.3})$$

where  $P_{1|1}(B | A) = P(A; B)/P(A)$  is the 2-order conditional probability that the second quantity assumes the value  $B$  when the first one is  $A$  and  $\bar{B}(A)$  is the average of  $B$  for a constant value of  $A$ .

According to (A.3), the mean current reads:

$$\begin{aligned}\langle I \rangle &= \frac{e dE}{2\pi\hbar} \left\langle \sum_{m_1 \in S} \sum_{m_2 \in D} \left[ \sigma_{Sm_1} \Omega_{m_2 m_1} - \sigma_{Dm_2} \Omega'_{m_1 m_2} \right] \right\rangle \\ &= \frac{e dE}{2\pi\hbar} \left\{ \left\langle \sum_{m_1 \in S} \sigma_{Sm_1} [\mathbf{t}^\dagger \mathbf{t}]_{m_1, m_1}^C - \sum_{m_2 \in D} \sigma_{Dm_2} [\mathbf{t}'^\dagger \mathbf{t}']_{m_2, m_2}^C \right\rangle \right\}\end{aligned} \quad (\text{A.4})$$

where the index  $C$  means that the trasmission probabilities depend on random occupation at both reservoirs. In (A.4) we have used the following observation ( $m_1 \in S$ ):

$$\begin{aligned} \langle \sum_{m_2 \in D} \Omega_{m_2 m_1} \rangle &= \sum_{m_2 \in D} \mathcal{T}_{m_2 m_1} = \sum_{m_2 \in D} |\mathbf{t}_{m_2 m_1}|^2 = [\mathbf{t}^\dagger \mathbf{t}]_{m_1 m_1} , \\ \langle \sum_{m_1 \in S} \Omega'_{m_1 m_2} \rangle &= \sum_{m_1 \in S} \mathcal{T}'_{m_1 m_2} = \sum_{m_1 \in S} |\mathbf{t}'_{m_1 m_2}|^2 = [\mathbf{t}'^\dagger \mathbf{t}']_{m_2 m_2} , \end{aligned} \quad (\text{A.5})$$

where  $\mathbf{t}'$  is the drain-to-source trasmission amplitude matrix.

In order to evaluate the power spectral density of shot noise at zero frequency, the mean squared current and the variance of the current are requested. The mean squared current reads:

$$\begin{aligned} \langle I^2 \rangle &= \left( \frac{e dE}{2\pi\hbar} \right)^2 \langle \sum_{m_1, m_2 \in S} \sum_{n_1, n_2 \in D} [\sigma_{S m_1} \sigma_{S m_2} \Omega_{n_1 m_1} \Omega_{n_2 m_2} \\ &\quad - \sigma_{S m_1} \sigma_{D n_2} \Omega_{n_1 m_1} \Omega'_{m_2 n_2} - \sigma_{D n_1} \sigma_{S m_2} \Omega'_{m_1 n_1} \Omega_{n_2 m_2} \\ &\quad + \sigma_{D n_1} \sigma_{D n_2} \Omega'_{m_1 n_1} \Omega'_{m_2 n_2}] \rangle = F_{SS} + F_{SD} + F_{DS} + F_{DD} \end{aligned} \quad (\text{A.6})$$

Eq. (A.6) contains four terms. The first (fourth) term represents the statistical average of products of two trasmission occurrences for electrons incident from the same reservoir S (D) and transmitted into D (S), with weights given by the random occupations of the initial states in S (D).

Let us consider for example the first term  $F_{SS}$  in Eq. (A.6). Although in the eigen-channels basis the modes can be considered independent from each other, i.e. trasmission occurs along separate trasmission channels, in the basis of incoming waves from source and drain extensions modes are coupled between them. This means that random occurrences, such as  $\Omega_{n_1 m_1}$  and  $\Omega_{n_2 m_1}$ , are not independents from each other. Indeed if an electron incident from the channel  $m_1$  in S is transmitted into channel  $n_1$  in D, the trasmission occurrence is 1 in this channel and 0 in the other all ( $\Omega_{n_2 m_1} = \delta_{n_1, n_2}$ ). As a consequence, channels are coupled between them. Moreover  $\Omega_{n_1 m_1}$  and  $\Omega_{n_1 m_2}$  ( $m_1 \neq m_2$ ) are not independent, due to the Pauli exclusion principle which inhibits trasmission of two electrons into the same channel  $n_1$  in D. However, if  $m_1 \neq m_2$ ,  $\sum_{n_1 \in D} \Omega_{n_1 m_1}$  and  $\sum_{n_2 \in D} \Omega_{n_2 m_2}$  are independent from each other since they represent the occurrences  $\Omega_{m_1}$  and  $\Omega_{m_2}$  that an electron incident from the channels  $m_1$  and  $m_2$  in S, respectively, is transmitted into D.

As a result, the first term of the expression (A.6) reads:

$$F_{SS} = \left( \frac{e dE}{2\pi\hbar} \right)^2 \left\{ \left\langle \sum_{m_1 \in S} \sigma_{Sm_1}^2 [\mathbf{t}^\dagger \mathbf{t}]_{m_1, m_1}^C \left[ 1 - [\mathbf{t}^\dagger \mathbf{t}]_{m_1, m_1}^C \right] \right\rangle \right. \\ \left. + \left\langle \left[ \sum_{m_1 \in S} \sigma_{Sm_1} [\mathbf{t}^\dagger \mathbf{t}]_{m_1, m_1}^C \right]^2 \right\rangle \right\} \quad (\text{A.7})$$

The fourth term ( $F_{DD}$ ) has the same structure, but replacing the random occupations of the source contact with the drain ones and the trasmission amplitude matrix  $\mathbf{t}$  with  $\mathbf{t}'$ .

The second term can be expressed as:

$$F_{SD} = - \left( \frac{e dE}{2\pi\hbar} \right)^2 \left\langle \sum_{m_1 \in S} \sigma_{Sm_1} \sum_{m_2 \in S} \left[ \sum_{n_1 \in D} \Omega_{n_1 m_1} \sum_{n_2 \in D} \sigma_{Dn_2} \Omega'_{m_2 n_2} \right] \right\rangle \quad (\text{A.8})$$

Note that we are interested to the case of *zero magnetic field*, when the reversal time symmetry holds. In this case, if  $m_2 \neq m_1$ , transmission events are independent and the statistical average of the product in the squared bracket in Eq. (A.8) is simply the product of two sums. In addition, by using the time reversal symmetry ( $\mathbf{t}' = \mathbf{t}^\dagger$ ), we find:

$$\left\langle \sum_{n_2 \in D} \sigma_{Dn_2} \Omega'_{m_2 n_2} \right\rangle = \left\langle \sum_{n_2 \in D} \sigma_{Dn_2} |\mathbf{t}_{n_2 m_2}|_C^2 \right\rangle. \quad (\text{A.9})$$

Instead if  $m_2 = m_1$ , the term  $\sum_{n_1 \in D} \Omega_{n_1 m_1}$  can be neglected since it does not provide an independent information with respect to  $\sum_{n_2 \in D} \sigma_{Dn_2} \Omega'_{m_1 n_2}$ . Indeed, in the case of zero magnetic field,  $\sum_{n_1 \in D} \Omega_{n_1 m_1} = \sum_{n_1 \in D} \Omega'_{m_1 n_1}$ . Finally the second term has the following expression:

$$F_{SD} = - \left\langle \sum_{m_1 \in S} \sum_{n_2 \in D} \sigma_{Sm_1} \sigma_{Dn_2} [\mathbf{t}^\dagger \mathbf{t}]_{m_1, m_1}^C [\mathbf{t} \mathbf{t}^\dagger]_{n_2, n_2}^C \right\rangle \\ - \left\langle \sum_{m_1 \in S} \sum_{n_2 \in D} \sigma_{Sm_1} \sigma_{Dn_2} |\mathbf{t}_{n_2 m_1}|_C^2 \left[ 1 - [\mathbf{t}^\dagger \mathbf{t}]_{m_1, m_1}^C \right] \right\rangle \quad (\text{A.10})$$

It can be seen that the third term in Eq. (A.6) is identical to the second one:  $F_{DS} = F_{SD}$ . Nevertheless, the mean-squared current can be

expressed in a symmetrical form with respect to the reservoirs S and D by simply changing the order of sums in the third term.

The mean-squared current can be expressed as:

$$\begin{aligned}
 \langle I^2 \rangle = & \left( \frac{e dE}{2\pi\hbar} \right)^2 \left\{ \left\langle \sum_{\alpha \in S, D} \sum_{n \in \alpha} \sigma_{\alpha n}^2 \tau_{\alpha;nn} [1 - \tau_{\alpha;nn}] \right\rangle \right. \\
 & + \left\langle \sum_{\alpha \in S, D} \left[ \sum_{n \in \alpha} \sigma_{\alpha} \tau_{\alpha;nn} \right]^2 \right\rangle - \left\langle \sum_{\substack{\alpha, \beta \in S, D \\ \beta \neq \alpha}} \sum_{m \in \alpha} \sum_{n \in \beta} \right. \\
 & \left. \left. \sigma_{\alpha m} \sigma_{\beta n} [\tau_{\alpha;mm} \tau_{\beta;nn} + \gamma_{nm}^{\beta \leftarrow \alpha} (1 - \tau_{\alpha;mm})] \right] \right\rangle \right\} \quad (\text{A.11})
 \end{aligned}$$

where we have defined the quantities ( $m \in S, n \in D$ )

$$\gamma_{nm}^{D \leftarrow S} = |\mathbf{t}_{nm}|_C^2 \quad ; \quad \gamma_{mn}^{S \leftarrow D} = |\mathbf{t}'_{mn}|_C^2 = \gamma_{nm}^{D \leftarrow S}$$

and ( $l \in \alpha$ )

$$\tau_{\alpha;ll} = \begin{cases} \tau_{S;ll} = [\mathbf{t}^\dagger \mathbf{t}]_{ll}^C & \text{if } \alpha = S \\ \tau_{D;ll} = [\mathbf{t}'^\dagger \mathbf{t}']_{ll}^C = [\mathbf{t} \mathbf{t}^\dagger]_{ll} & \text{if } \alpha = D \end{cases}$$

The result for the drain current fluctuations in a two terminal non-interacting mesoscopic conductor reads [57]:

$$\begin{aligned}
 \text{var}(I) = & \left( \frac{e dE}{2\pi\hbar} \right)^2 \left\{ \left\langle \sum_{\alpha \in S, D} \sum_{n \in \alpha} \sigma_{\alpha n} \tau_{\alpha;nn} [1 - \tau_{\alpha;nn}] \right\rangle \right. \\
 & - \sum_{\substack{\alpha, \beta \in S, D \\ \beta \neq \alpha}} \sum_{m \in \alpha} \sum_{n \in \beta} \sigma_{\alpha m} \sigma_{\beta n} \gamma_{nm}^{\beta \leftarrow \alpha} (1 - \tau_{\alpha;mm}) \rangle \\
 & + \text{var} \left( \sum_{m \in S} \sigma_{Sm} \tau_{S;mm} - \sum_{n \in D} \sigma_{Dn} \tau_{D;nn} \right) \}, \quad (\text{A.12})
 \end{aligned}$$

where we have exploited the relation  $\sigma_{\alpha n}^2 = \sigma_{\alpha n}$ . Finally, according to the Milatz Theorem, the power spectral density at zero frequency  $S(0)$  reads

$$S(0) = \frac{2}{\nu} \text{var}(I) = \frac{4\pi\hbar}{dE} \text{var}(I), \quad (\text{A.13})$$

where  $\nu = dE/(2\pi\hbar)$  is the maximum injection rate of the carriers [143] and  $\text{var}(I)$  is given by Eq. (A.12). We can observe that the first and the fourth terms of Eq. (2.19) are correctly reproduced in Eq. (A.13), whereas exchange interference effects are only partially considered. This is because, unlike the approach used in this appendix, the second quantization formalism automatically accounts for the quantum-mechanical impossibility to distinguish between indential carriers.

## Appendix B

# The Fischer-Lee relation

Let us consider a 2D channel of length  $L$  and denote with  $x$  and  $y$  the longitudinal direction and the transverse one, respectively. If the interface between the lead S (D) and the conductor is defined by  $x_S = 0$  ( $x_D = 0$ ),  $\mathbf{G}_{DS}(y_D; y_S) = \mathbf{G}_{DS}(x_D = 0, y_D; x_S = 0, y_S)$  represents the wavefunction at  $(x_D = 0, y_D)$  due to an excitation at  $(x_S = 0, y_S)$ . In real space the *Fischer-Lee relation* reads:

$$\mathbf{s}_{nm} = -\delta_{nm} + \frac{i\hbar\sqrt{v_n v_m}}{a} \int dy_D \int dy_S \chi_n(y_D) \mathbf{G}_{DS}(y_D; y_S) \chi_m(y_S) \quad (\text{B.1})$$

where  $n$  is a mode outgoing at lead D with velocity  $v_n$ ,  $m$  is a mode incoming at lead S with velocity  $v_m$  and  $a$  is the lattice constant along the  $x$  direction. In the  $\mathbf{k}$ -representation, for a conductor of uniform cross-section, we can exploit a mode representation in the transverse direction and a plane wave representation in the longitudinal direction and (B.1) becomes:

$$\mathbf{s}_{nm} = -\delta_{nm} + \frac{i\hbar\sqrt{v_n v_m}}{L} \mathbf{G}_{DS}(n, m) \quad (\text{B.2})$$

where  $\mathbf{G}_{DS}(n, m) = \mathbf{G}_{DS}(n, k_n; m, k_m)$  and  $k_n$  is the longitudinal wavevector of the transverse mode  $n$ . Let us assume both leads to be identical and denote with  $\{k_1^S, \dots, k_N^S\}$  ( $\{k_1^D, \dots, k_N^D\}$ ) the set of wavevectors associated to the  $N$  modes coming from the lead S (D). Since the only non-zero components of the self-energy involve the end-points, in the

$\mathbf{k}$ -representation  $\mathbf{\Gamma}_S$  and  $\mathbf{\Gamma}_D$  can be expressed as

$$\mathbf{\Gamma}_S = \begin{pmatrix} \mathbf{\Gamma}_{S;11} & \mathbf{0} \\ \mathbf{0} & \mathbf{0} \end{pmatrix}_{2N \times 2N} \quad \mathbf{\Gamma}_D = \begin{pmatrix} \mathbf{0} & \mathbf{0} \\ \mathbf{0} & \mathbf{\Gamma}_{D;22} \end{pmatrix}_{2N \times 2N}$$

where  $\mathbf{\Gamma}_{S;11}(n, m) = \delta_{nm} \frac{\hbar v(k_n^S)}{L} \forall n, m \in S$  and  $\mathbf{\Gamma}_{D;22}(n, m) = \delta_{nm} \frac{\hbar v(k_n^D)}{L} \forall n, m \in D$ .

Generalization to a CNT-FET structure is straightforward. Let us indicate with  $N_C$  and  $N_M$  the number of carbon atoms rings and the number of modes propagating along the channel, respectively. Since the coupling between the identical reservoirs and the channel involve only the end-rings of the channel,  $\mathbf{\Gamma}_S$  and  $\mathbf{\Gamma}_D$  are  $(N_M N_C) \times (N_M N_C)$  diagonal matrix and the only non-zero blocks are the first one and the latter one, respectively:

$$\begin{aligned} \mathbf{\Gamma}_{S;11}(n, m) &= \delta_{nm} \frac{\hbar v(k_n)}{L} \quad \forall n, m = 1, \dots, N_M \\ \mathbf{\Gamma}_{D;N_C N_C}(n, m) &= \delta_{nm} \frac{\hbar v(k_n)}{L} \quad \forall n, m = 1, \dots, N_M \end{aligned} \quad (\text{B.3})$$

By exploiting Eqs. (B.2) and (B.3) we can find the transmission ( $\mathbf{t}$ ) and reflection ( $\mathbf{r}$ ) amplitude matrix:

$$\begin{aligned} \mathbf{t}_{nm} &= i \sqrt{\mathbf{\Gamma}_{D;N_C N_C}(n, n) \mathbf{G}_{N_C 1}(n, m)} \sqrt{\mathbf{\Gamma}_{S;11}(m, m)} \\ \mathbf{r}_{nm} &= -\delta_{nm} + i \sqrt{\mathbf{\Gamma}_{S;11}(n, n) \mathbf{G}_{11}(n, m)} \sqrt{\mathbf{\Gamma}_{S;11}(m, m)} \end{aligned} \quad (\text{B.4})$$

Since at zero magnetic field  $\mathbf{t}' = \mathbf{t}^\dagger$ , relations (B.4) is all we need to compute the power spectral density (2.1) from Eq. (2.19). A similar procedure has been adopted for SNW-FETs where, from a computational point of view, the channel has been discretized in a sequence of slices in the longitudinal direction. In this case Eqs. in (B.4) are obtained as well, but replacing the number of rings with the number of slices



## Appendix C

# Approximations of electron-phonon scattering

### C.1 Approximation IIS: intrasubband intravalley scattering

Eqs. (5.15) and (5.18) requires the complete knowledge of the electron and phonon dispersion curves mapped in the entire Brillouin zone, which demands prohibitively large amount of computational power when calculating phonon scattering rates and electron mobility.

For convenience, let us focus on the 0-th order LA and LO subbranches ( $q_{y\beta} = 0$ ), 0-LA and 0-LO respectively, and considering only the lowest electron subbands [21]. In particular, neglecting both the inter-subband scattering ( $k_{y\eta'} = k_{y\eta}$ ) and the factor  $[1 - f(E_{\mathbf{k}'})] / [1 - f(E_{\mathbf{k}})]$ , assuming  $\alpha = \pi$  and accounting for a single phonon energy value  $E_{ph}^{LO}$  in the LO subbranch, Eqs. (5.15) and (5.18) reduces to the momentum relaxation rates in Ref. [21], since the form factor  $G = 1$ , as shown in

Eq. (5.12):

$$\begin{aligned}\frac{1}{\tau_{AC}(\mathbf{k})} &= \frac{n_{\mathbf{q}}^{\mp} \pi \hbar D_{AC}^2 q_x^2}{4 \rho W E_{ph}^{LA}} \rho_{GNR}(E_{\mathbf{k}} \pm E_{ph}^{LA}) (1 + \cos \tilde{\theta}_{\mathbf{k}\mathbf{k}'}) \\ \frac{1}{\tau_{OP}(\mathbf{k})} &= \frac{n_{\mathbf{q}}^{\mp} \pi \hbar D_{OP}^2}{4 \rho W E_{ph}^{LO}} \rho_{GNR}(E_{\mathbf{k}} \pm E_{ph}^{LO}) (1 + \cos \tilde{\theta}_{\mathbf{k}\mathbf{k}'}),\end{aligned}\tag{C.1}$$

where  $E_{ph}^{LA} = \hbar v_{LA} q_x$ ,  $v_{LA}$  ( $\approx 20600$  m/s) is the LA sound velocity,  $|q_x| = 2|k_x|$  for a backscattering event,  $\rho_{GNR}$  is the 1D density of states per unit length and the following relation have been exploited:

$$\begin{aligned}2 \frac{L}{2\pi} \int dq_x \delta_D[E(k_x \pm q_x, k_y') - E(k_x, k_y) \mp E_{ph}^{LA}(q_x)] \times \\ \times (1 + \cos \theta_{\mathbf{k}\mathbf{k}'}) = \frac{L}{2} (1 + \cos \tilde{\theta}_{\mathbf{k}\mathbf{k}'}) \rho_{GNR}(E_{\mathbf{k}} \pm E_{ph}^{LA})\end{aligned}\tag{C.2}$$

In Eqs. (C.1) the overlap factor  $(1 + \cos \tilde{\theta}_{\mathbf{k}\mathbf{k}'})$  has to be evaluated in correspondence of the backscattering event which satisfies the energy and longitudinal momentum conservations. Note also that Eqs. (C.1) include the main contribution to intrasubband scattering, since they consider the main maxima ( $G = 1$ ) of the form factor  $G$ .

Eqs. (C.1) may be convenient when adopting a formula for the electron dispersion curves which well approximates the tight-binding conduction band of a graphene sheet close to the conduction band minima, i.e. for  $E(\mathbf{k})$  at the Dirac Point  $\mathbf{K} = (2\pi/\sqrt{3}a, 2\pi/3a)$  or  $\mathbf{K}' = (0, 4\pi/3a)$ . For example, a good approximation between the tight-binding and the effective mass approximation is [124]:

$$E(k_x, k_{y\eta}) = \sqrt{E_{\eta}^2 + \frac{E_{\eta} \hbar^2 k_x^2}{m_{\eta}}},\tag{C.3}$$

where  $E_{\eta}$  is the energy minimum of the  $\eta$ -th subband computed by means of the tight-binding method and including edge relaxations [124, 144] and  $m_{\eta}$  is the corresponding effective mass.

In order to calculate Eqs. (C.1), the overlap factor  $(1 + \cos \theta_{\mathbf{k}\mathbf{k}'})$  can be evaluated by means of Eq. (5.6). In particular, since the transverse momentum of the lower tight-binding subbands is close to the point  $\mathbf{K}'$  [124], we can exploit an appropriate series expansion of the electron wavevector around  $\mathbf{K}'$ . Starting from  $k_x = \tilde{k}_x$  ( $\tilde{k}_x \ll k_F$ ) and  $k_{y\eta} =$

### C.1. Approximation IIS: intrasubband intravalley scattering 31

$\mathbf{K}'_y + \tilde{k}_{y\eta}$  ( $\tilde{k}_{y\eta} \ll \mathbf{K}'_y = 4\pi/3a$ ), where  $\tilde{k}_x$  ( $\tilde{k}_{y\eta}$ ) are the longitudinal (transverse) momentum referred to  $\mathbf{K}'$ , we obtain:

$$t_{\mathbf{k}} \approx \frac{\sqrt{3}a}{2} \left( i\tilde{k}_x - \tilde{k}_{y\eta} \right), \quad (\text{C.4})$$

and:

$$e^{i\theta_{\mathbf{k}}} = \frac{t_{\mathbf{k}}}{|t_{\mathbf{k}}|} = \frac{i\tilde{k}_x - \tilde{k}_{y\eta}}{\sqrt{\tilde{k}_x^2 + \tilde{k}_{y\eta}^2}}, \quad (\text{C.5})$$

or, equivalently:

$$\theta_{\mathbf{k}} = -\text{arctg} \left( \tilde{k}_x / \tilde{k}_{y\eta} \right). \quad (\text{C.6})$$

For intrasubband scattering, Eq. (C.5) can be expressed as:

$$e^{i\theta_{\mathbf{k}\mathbf{k}'}} = \frac{i\tilde{k}_x - \tilde{k}_{y\eta}}{i\tilde{k}'_x - \tilde{k}_{y\eta}} \frac{|\tilde{\mathbf{k}}'|}{|\tilde{\mathbf{k}}|}. \quad (\text{C.7})$$

Therefore the overlap factor reads:

$$1 + \cos \theta_{\mathbf{k}\mathbf{k}'} = \frac{\tilde{k}_{y\eta}^2 \left( |\tilde{\mathbf{k}}| + |\tilde{\mathbf{k}}'| \right)^2 + \left( \tilde{k}'_x |\tilde{\mathbf{k}}| + \tilde{k}_x |\tilde{\mathbf{k}}'| \right)^2}{2 |\tilde{\mathbf{k}}|^2 |\tilde{\mathbf{k}}'|^2}, \quad (\text{C.8})$$

where  $\tilde{\mathbf{k}} = (\tilde{k}_x, \tilde{k}_{y\eta})$  ( $\tilde{\mathbf{k}}' = (\tilde{k}'_x, \tilde{k}_{y\eta})$ ) is the initial (final) electron wavevector referred to the  $\mathbf{K}'$  point. By using Eq. (C.8) along with Eqs. (C.1), the momentum relaxation rates for intrasubband scattering in the  $\eta$ -th subband can be computed.

Let now consider the limit of elastic scattering, which well applies to scattering from acoustic phonons at room temperature. In this case backscattering restricts the value of the final electron wavevector to  $\tilde{k}'_x = -\tilde{k}_x$  and Eq. (C.8) reduces to:

$$1 + \cos \theta_{\mathbf{k}\mathbf{k}'} = \frac{2\tilde{k}_{y\eta}^2}{\tilde{k}_{y\eta}^2 + \tilde{k}_x^2}. \quad (\text{C.9})$$

We note in Eq. (C.9) that the overlap factor starts from the value 2 at low energies ( $|\tilde{k}_x| \ll \tilde{k}_{y\eta}$ ) and decreases moving out from the bottom of the upwards conduction subband: the lower the value of  $\tilde{k}_{y\eta}$ , and

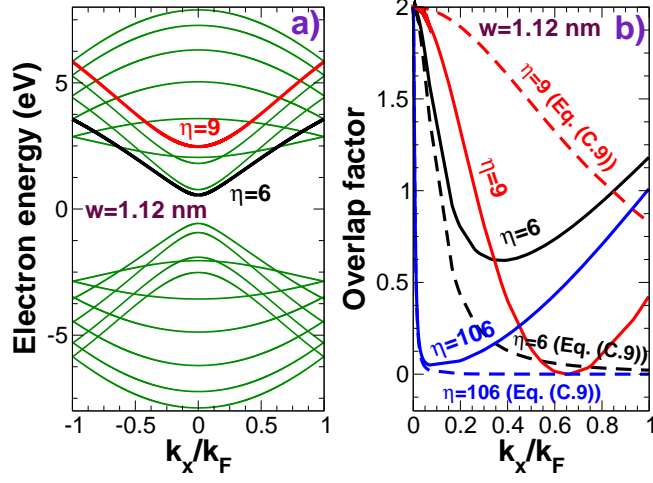


Figure C.1: a) Electron dispersion curve considering edge relaxation computed for a GNR width  $W = 1.12$  nm. b) Overlap factor for intra-subband scattering computed by means of Eq. (5.6) (solid lines) and by exploiting Eq. (C.9) (dashed lines) for the two colored subbands in (a) ( $W = 1.12$  nm). The overlap factor for the lowest subband ( $\eta = 106$ ) computed by means of Eq. (5.6) and Eq. (C.9) (blue solid and dashed lines, respectively) for  $W = 19.83$  nm is also sketched.

therefore more accurate the series expansion (C.4) and Eq. (C.9), the faster the decrease of the overlap factor.

Fig. C.1b shows the overlap factor computed by means of the full-band approach (Eqs. (5.6)), solid lines) and by means of Eq. (C.9) (dashed lines) for intrasubband scattering in a 1 nm-wide GNR. As can be seen in Fig. C.1b, the agreement between the full-band analysis and Eq. (C.9) is good at low  $k_x$  for the lowest subband  $\eta = 6$  due to its transverse momentum  $k_{y\eta}$  close to  $\mathbf{K}'_y$ . We also note that Eq. (C.9) fails to reproduce the correct behaviour when  $k_x \gg k_{y\eta}$  and for upwards subbands with  $k_{y\eta}$  far from the Dirac points  $\mathbf{K}'$  ( $\eta = 9$  in Fig. C.1b).

The geometrical interpretation of  $\theta_{\mathbf{k}}$  as the angle between the vector  $\tilde{\mathbf{k}}$  and  $k_{y\eta}$  (Eq. (C.6)) forbids backscattering when the energy is high and far from the bottom of the conduction subbands ( $k_x \gg k_{y\eta}$ ). In general this is not true, since the angle  $\theta_{\mathbf{k}\mathbf{k}'}$  has not a simple geomet-

ric interpretation but it is intrinsically tied to the spinor nature of the graphene wavefunction. Since the transverse momentum  $k_{y\eta}$  of the lowest conduction subband becomes closer and closer to  $\mathbf{K}'_y$  with increasing  $W$ , the Taylor expansion (C.4) becomes more and more accurate. As a consequence, at low electron energies the agreement between the full-band approach and Eq. (C.9) improves for large  $W$  (see Fig. C.1b for  $W = 19.83$  nm).

## C.2 Approximation IISNS: neglect of the spinor

We now consider the case when spinor is neglected, within the intrasubband intravalley scattering case. Such approximation will be referred as approximation IISNS. Starting from the electron wavefunction:

$$\Psi_{\mathbf{k}}(x, y) = \frac{1}{\sqrt{L}} e^{ik_x x} \Psi_{\perp, \eta}(y) = \frac{1}{\sqrt{L}} e^{ik_x x} \sqrt{\frac{2}{W+a}} \sin \left[ k_{y\eta} \left( y + \frac{a}{2} \right) \right], \quad (\text{C.10})$$

Eqs. (C.1) reduce to:

$$\begin{aligned} \frac{1}{\tau_{AC}(\mathbf{k})} &= \frac{n_{\mathbf{q}}^{\mp} \pi \hbar D_{AC}^2 q_x^2}{2 \rho W E_{ph}^{LA}} \rho_{GNR}(E_{\mathbf{k}} \pm E_{ph}^{LA}) \\ \frac{1}{\tau_{OP}(\mathbf{k})} &= \frac{n_{\mathbf{q}}^{\mp} \pi \hbar D_{OP}^2}{2 \rho W E_{ph}^{LO}} \rho_{GNR}(E_{\mathbf{k}} \pm E_{ph}^{LO}). \end{aligned} \quad (\text{C.11})$$

It is immediate to see that the factor  $(1 + \cos \tilde{\theta}_{\mathbf{k}\mathbf{k}'})/4$  in Eq. (C.1) is replaced by a factor  $1/2$  in Eq. (C.11). Therefore, according to Eq. (C.9), for energies very close to the conduction subband edge no differences are observed. In particular, according to Fig. C.1b, we can expect that the effect of neglect of spinor becomes more and more severe for wider ribbons, where the decrease of the overlap factor  $(1 + \cos \theta_{\mathbf{k}\mathbf{k}'})$  from the value 2 becomes faster and faster.

### C.3 Approximation 2DPNS: neglect of the spinor and 2D phonons

Phonon scattering corresponding to the momentum relaxation rates (C.1) is not isotropic, i.e. the scattering mechanism tends to deflect electrons by large angles (backward scattering), presents an energy dependent overlap factor  $(1 + \cos \theta_{\mathbf{k}\mathbf{k}'})$  and applies only to intrasubband scattering. On the other hand, Eqs. (5.15) and (5.18), which include both the intrasubband and intersubband scattering, requires the knowledge of the full-band phonon dispersion curves and the integrals must be performed numerically with a high computational cost.

In order to include both intrasubband and intersubband scattering without computing the GNR phonon spectra, a quite rude approximation consists in neglecting the two-component nature of the graphene eigenfunction, assuming 2D phonons (i.e.  $q_y$  is continuous) and considering simple hard-wall boundary conditions for the electron eigenfunction, as in Eq. (5.3). The electron wavefunction in this case can be expressed as [130]:

$$\Psi_{\mathbf{k}}(x, y) = \frac{1}{\sqrt{L}} e^{ik_x x} \Psi_{\perp, \eta}(y) = \frac{1}{\sqrt{L}} e^{ik_x x} \sqrt{\frac{2}{W}} \sin(k_y \eta y), \quad (\text{C.12})$$

where  $\Psi_{\perp, \eta}(y)$  is the transverse component of the wavefunction. By means of Eq. (5.17), the matrix element of the interaction potential on the eigenfunction (C.12) reads:

$$\begin{aligned} \widetilde{V}_{AC} &= \langle \Psi_{\mathbf{k}}, n_{\mathbf{q}} \mp 1 | V_{AC} | \Psi_{\mathbf{k}}, n_{\mathbf{q}} \rangle \\ &= \sqrt{\frac{D_{AC}^2 n_{\mathbf{q}}^{\mp} \hbar^2 q^2}{2\rho W L E_{ph}}} \int_0^W dy \Psi_{\perp}^{\prime*}(y) \Psi_{\perp}(y) e^{\pm i q_y y} \delta(k'_x - k_x \mp q_x). \end{aligned} \quad (\text{C.13})$$

If longitudinal acoustic phonons of small  $\mathbf{q}$ , belonging to the LA graphene mode, are taken into account, the phonon dispersion curve can be approximated as:

$$E_{ph} = E_{ph}^{LA} = \hbar v_{LA} q. \quad (\text{C.14})$$

By using Eq. (C.14) and assuming 2D phonons, i.e. a continuum of wavevectors in the transverse direction  $y$ , the momentum relaxation rate

can be expressed as ( $\alpha = 0, \pi$ ):

$$\begin{aligned}
 \frac{1}{\tau_{AC}(\mathbf{k})} &= \sum_{\mathbf{k}'} S(\mathbf{k}, \mathbf{k}') (1 - \cos \alpha) \\
 &= \frac{D_{AC}^2 n_{\mathbf{q}}^{\mp} \pi \hbar}{2 \rho E_{ph}^{LA}} \left( \frac{E_{ph}^{LA}}{\hbar v_{LA}} \right)^2 \left( \int_0^W dy_1 \Psi'_{\perp}(y_1) \Psi_{\perp}^*(y_1) \right) \times \\
 &\quad \times \left( \int_0^W dy \Psi'_{\perp}^*(y) \Psi_{\perp}(y) \right) \delta(y - y_1) \frac{2}{\pi} \int dq_x \delta_D[E(k_x \pm q_x, k_{y\eta'}) - \\
 &\quad - E(k_x, k_{y\eta}) \mp E_{ph}^{LA}]
 \end{aligned} \tag{C.15}$$

Finally, by exploiting:

$$\int_0^W dy |\Psi'_{\perp}(y)|^2 |\Psi_{\perp}(y)|^2 = \frac{3}{2W} \delta_{\eta', \eta} + \frac{1}{W} (1 - \delta_{\eta', \eta}), \tag{C.16}$$

and Eq. (C.2) without the overlap factor  $(1 + \cos \theta_{\mathbf{k}\mathbf{k}'})$ , we obtain:

$$\begin{aligned}
 \frac{1}{\tau_{AC}(\mathbf{k})} &= \frac{\pi D_{AC}^2 E_{ph}^{LA} n_{\mathbf{q}}^{\mp}}{2 \hbar \rho v_{LA}^2} \left[ \frac{3}{2W} \delta_{\eta', \eta} + \frac{1}{W} (1 - \delta_{\eta', \eta}) \right] \times \\
 &\quad \times \rho_{GNR}(E_{\mathbf{k}} \pm E_{ph}^{LA}),
 \end{aligned} \tag{C.17}$$

where the quantity in the squared brackets represents the new overlap factor. According to Eq. (C.17), the intrasubband scattering rate ( $\eta' = \eta$ ) is enhanced by a factor of 3/2 with respect to the rate of intersubband transitions ( $\eta' \neq \eta$ ) [130]. Following a similar procedure, the scattering rate for optical LO phonons reads:

$$\begin{aligned}
 \frac{1}{\tau_{OP}(\mathbf{k})} &= \frac{\pi \hbar D_{OP}^2 n_{\mathbf{q}}^{\mp}}{2 \rho E_{ph}^{LO}} \left[ \frac{3}{2W} \delta_{\eta', \eta} + \frac{1}{W} (1 - \delta_{\eta', \eta}) \right] \times \\
 &\quad \times \rho_{GNR}(E_{\mathbf{k}} \pm E_{ph}^{LO}).
 \end{aligned} \tag{C.18}$$

We can see that, when focusing on only intrasubband scattering, the factor  $(1 + \cos \theta_{\mathbf{k}\mathbf{k}'})/4$  in Eq. (C.1) is replaced by the factor 3/4 in Eq. (C.17). Since  $(1 + \cos \theta_{\mathbf{k}\mathbf{k}'})/4 \approx 1/2$  near the subband edge [Eq. (C.9)], Eq. (C.17) overestimates the rate by roughly a factor 3/2 for narrow ribbons.





# Bibliography

- [1] S. Iijima and T. Ichihashi. Single-shell carbon nanotubes of 1-nm diameter. *Nature*, vol. 363, pp. 603–605, 1993.
- [2] K. S. Novoselov, A. K. Geim, S. V. Morozov, D. Jiang, Y. Zhang, S. V. Dubonos, I. V. Grigorieva, and A. A. Firsov. Electric Field Effect in Atomically Thin Carbon Films. *Science*, vol. 306, pp. 666, 2004.
- [3] J.-H. Chen, C. Jang, S. Xiao, M. Ishigami, and M. S. Fuhrer. Intrinsic and extrinsic performance limits of graphene devices on  $\text{SiO}_2$ . *Nature Nanotechnology*, vol. 3, pp. 206–209, 2008.
- [4] X. Li, X. Wang, L. Zhang, S. Lee, and H. Dai. Chemically derived, ultrasmooth graphene nanoribbon semiconductors. *Science*, vol. 319, pp. 1229–1231, 2008.
- [5] X. Du, I. Skachko, A. Barker, and E. Y. Andrei. Approaching ballistic transport in suspended graphene. *Nature Nanotechnology*, vol. 3, pp. 491–495, 2008.
- [6] K. I. Bolotin, K. J. Sikes, J. Hone, H. L. Stormer, and P. Kim. Temperature-Dependent Transport in Suspended Graphene. *Phys. Rev. Lett.*, vol. 101, pp. 096802, 2008.
- [7] Z. Chen and J. Appenzeller. Mobility Extraction and Quantum Capacitance Impact in High Performance Graphene Field-effect Transistor Devices. *IEDM Tech. Digest*, pp. 509–512, 2008.
- [8] K. S. Novoselov, A. K. Geim, S. V. Morozov, D. Jiang, M. I. Katsnelson, I. V. Grigorieva, S. V. Dubonos, and A. A. Firsov. Two-dimensional gas of massless dirac fermions in graphene. *Nature*, vol. 438, pp. 197–200, 2005.

- [9] G. Fiori, S. Lebegue, A. Betti, P. Michetti, M. Klintenberg, O. Eriksson, and G. Iannaccone. Simulation of hydrogenated graphene field-effect transistors through a multiscale approach. *Phys. Review B*, vol. 82, pp. 153404, 2010.
- [10] G. Fiori, S. Lebegue, A. Betti, P. Michetti, M. Klintenberg, O. Eriksson, and G. Iannaccone. A multi-scale approach for performance assessment of hydrogenated graphene field-effect transistors. *IWCE Tech. Digest*, pp. 1–4, 2010.
- [11] Y. Zhang, T.-T. Tang, C. Girit, Z. Hao, M. C. Martin, A. Zettl, M. F. Crommie, Y. R. Shen, and F. Wang. Direct observation of a widely tunable bandgap in bilayer graphene. *Nature*, vol. 459, pp. 820–823, 2009.
- [12] X. Wang, Y. Ouyang, X. Li, H. Wang, J. Guo, and H. Dai. Room-temperature all-semiconducting sub-10 nm graphene nanoribbon field-effect transistors. *Phys. Rev. Lett.*, vol. 100, pp. 206803, 2008.
- [13] Y. Li, A. Sinitskii, and J. M. Tour. Electronic two-terminal bistable graphitic memories. *Nature Materials*, vol. 7, pp. 966–971, 2008.
- [14] M. D. Stoller, S. Park, Y. Zhu, J. An, and R. S. Ruoff. Graphene-based ultracapacitors. *Nano Lett.*, vol. 8, pp. 3498–3502, 2008.
- [15] F. Bonaccorso, Z. Sun, T. Hasan, and A. C. Ferrari. Graphene photonics and optoelectronics. *Nature Photonics*, vol. 4, pp. 611–622, 2010.
- [16] O. M. Bulashenko and J. M. Rubí. Shot-noise suppression by Fermi and Coulomb correlations in ballistic conductors. *Phys. Rev. B*, vol. 64, pp. 045307, 2001.
- [17] L. G. Herrmann, T. Delattre, P. Morfin, J.-M. Berroir, B. Placais, D. C. Glatthi, and T. Kontos. Shot Noise in Fabry-Perot Interferometers Based on Carbon Nanotubes. *Phys. Rev. Lett.*, vol. 99, pp. 156804, 2007.
- [18] Y. Yang and R. Murali. Impact of Size Effect on Graphene Nanoribbon Transport. *IEEE Elec. Dev. Lett.*, vol. 31, pp. 237–239, 2010.
- [19] J.-H. Chen, W. G. Cullen, C. Jang, M. S. Fuhrer, and E. D. Williams. Defect Scattering in Graphene. *Phys. Rev. Lett.*, vol. 102, pp. 236805, 2009.

- [20] J.-H. Chen, C. Jang, S. Adam, M. S. Fuhrer, E. D. Williams, and M. Ishigami. Charged-impurity scattering in graphene. *Nature Physics*, vol. 4, pp. 377–381, 2008.
- [21] T. Fang, A. Konar, H. Xing, and D. Jena. Mobility in semiconducting graphene nanoribbons: Phonon, impurity, and edge roughness scattering. *Phys. Rev. B*, vol. 78, pp. 205403, 2008.
- [22] A. Konar, T. Fang, and D. Jena. Effect of high- $k$  gate dielectrics on charge transport in graphene-based field effect transistors. *Phys. Rev. B*, vol. 82, pp. 115452, 2010.
- [23] R. Murali, K. Brenner, Y. Yang, T. Beck, and J. D. Meindl. Resistivity of Graphene Nanoribbon Interconnects. *IEEE Electron Device Lett.*, vol. 30, pp. 611–613, 2009.
- [24] K. M. Borysenko, J. T. Mullen, E. A. Barry, S. Paul, Y. G. Semenov, J. M. Zavada, M. Buongiorno Nardelli, and K. W. Kim. First-principles analysis of electron-phonon interactions in graphene. *Phys. Rev. B*, vol. 81, pp. 121412, 2010.
- [25] A. Akturk and N. Goldsman. Electron transport and full-band electron-phonon interactions in graphene. *J. Appl. Phys.*, vol. 103, pp. 053702, 2008.
- [26] V. Perebeinos and P. Avouris. Inelastic scattering and current saturation in graphene. *Phys. Rev. B*, vol. 81, pp. 195442, 2010.
- [27] S. Fratini and F. Guinea. Substrate-limited electron dynamics in graphene. *Phys. Rev. B*, vol. 77, pp. 195415, 2008.
- [28] X. Li, E. A. Barry, J. M. Zavada, M. B. Nardelli, and K. W. Kim. Surface polar phonon dominated electron transport in graphene. *Appl. Phys. Lett.*, vol. 97, pp. 232105, 2010.
- [29] S. Datta. Electronic transport in mesoscopic systems. *Cambridge University Press*, 1995.
- [30] S. Datta. Nanoscale device modeling: the Green’s function method. *Superlattices and Microstructures*, vol. 28, pp. 253–278, 2000.
- [31] J. Guo, S. Datta, and M. S. Lundstrom. Towards Multi-Scale Modeling of Carbon Nanotube Transistors. *International J. on*

*Multiscale Computational Engineering, special issue on multiscale methods for emerging technologies*, ed. N. Aluru, vol. 2, pp. 257–276, 2004.

- [32] I. Hassaninia, Z. Kordrostami, and M. H. Sheikhi. Simulation of carbon nanotube FETs with linear doping profile near the source and drain contacts. *Solid-State Electronics*, vol. 52, pp. 980–985, 2008.
- [33] A. Svizhenko, M. P. Anantram, T. R. Govindan, and B. Biegel. Two-dimensional quantum mechanical modeling of nanotransistors. *J. Appl. Phys.*, vol. 91, pp. 2343–2354, 2002.
- [34] W. van Haeringen, B. Farid, and D. Lenstra. *Physica Scripta*, vol. T19, pp. 282, 1987.
- [35] R. Landauer. "Spatial Variation of Currents and Fields Due to Localized Scatterers in Metallic Conduction". *IBM J. Res. Dev.*, vol. 1, pp. 223, 1957.
- [36] R. Landauer. Condensed-matter physics: The noise is the signal. *Nature*, vol. 392, pp. 658–659, 1998.
- [37] Y. M. Lin, J. Appenzeller, J. Knoch, Z. Chen, and P. Avouris. Low-Frequency Current Fluctuations in Individual Semiconducting Single-Wall Carbon Nanotubes. *Nano Lett.*, vol. 6, pp. 930–936, 2006.
- [38] J. Appenzeller, Y.-M. Lin, J. Knoch, Z. Chen, and P. Avouris. 1/f Noise in Carbon Nanotubes Devices-On the Impact of Contacts and Device Geometry. *IEEE Trans. on Nanotechnology*, vol. 6, pp. 368–373, 2007.
- [39] J. Tersoff. Low-Frequency Noise in Nanoscale Ballistic Transistors. *Nano Lett.*, vol. 7, pp. 194–198, 2007.
- [40] P.-E. Roche, M. Kociak, S. Guéron, A. Kasumov, B. Reulet, and H. Bouchiat. Very low shot noise in carbon nanotubes. *Eur. Phys. J. B*, vol. 28, pp. 217–222, 2002.
- [41] Y. Naveh, A. N. Korotkov, and K. K. Likharev. Shot-noise suppression in multimode ballistic Fermi conductors. *Phys. Rev. B*, vol. 60, pp. R2169–R2172, 1999.

- [42] G. Iannaccone. Analytical and Numerical Investigation of Noise in Nanoscale Ballistic Field Effect Transistors. *J. Comput. Electron.*, vol. 3, pp. 199–202, 2004.
- [43] G. Iannaccone, G. Lombardi, M. Macucci, and B. Pellegrini. Enhanced Shot Noise in Resonant Tunneling: Theory and Experiment. *Phys. Rev. Lett.*, vol. 80, pp. 1054–1057, 1998.
- [44] G. Iannaccone, M. Macucci, and B. Pellegrini. Shot noise in resonant-tunneling structures. *Phys. Rev. B*, vol. 55, pp. 4539–4550, 1997.
- [45] Ya. M. Blanter and M. Büttiker. Transition from sub-poissonian to super-poissonian shot noise in resonant quantum wells. *Phys. Rev. B*, vol. 59, pp. 10217–10226, 1999.
- [46] M. Büttiker. Scattering theory of current and intensity noise correlations in conductors and wave guides. *Phys. Rev. B*, vol. 46, pp. 12485–12507, 1992.
- [47] Th. Martin and R. Landauer. Wave-packet approach to noise in multichannel mesoscopic systems. *Phys. Rev. B*, vol. 45, pp. 1742–1755, 1992.
- [48] S. Datta. "Nanoscale Device Simulation: The Green's Function Method". *Superlattices and Microstructures*, 28:253–278, 2000.
- [49] A. van der Ziel. Noise in Solid State Device and Circuits. *Wiley, New York*, pp. 16 and 75–78, 1986.
- [50] Ya. M. Blanter and M. Büttiker. Shot noise in mesoscopic conductors. *Physics Reports*, vol. 336, pp. 1–166, 2000.
- [51] S. Datta. Electronic transport in mesoscopic systems. *Cambridge University Press*, 1995.
- [52] A. Betti, G. Fiori, and G. Iannaccone. Shot noise suppression in quasi one-dimensional Field Effect Transistors. *IEEE Trans. on Electron Devices*, vol. 56, pp. 2137–2143, 2009.
- [53] N. Sai, M. Zwolak, G. Vignale, and M. Di Ventra. *Phys. Rev. Lett.*, vol. 94, pp. 186810, 2005.

- [54] G. Vignale and M. Di Ventra. Incompleteness of the Landauer formula for electronic transport. *Phys. Rev. B*, vol. 79, pp. 014201, 2009.
- [55] A. Betti, G. Fiori, and G. Iannaccone. Statistical theory of shot noise in quasi-1d field effect transistors in the presence of electron-electron interaction. *Phys. Review B*, vol. 81, pp. 035329, 2010.
- [56] Code and Documentation can be found at the url: <http://www.nanohub.org/tools/vides>.
- [57] A. Betti, G. Fiori, and G. Iannaccone. Shot noise in quasi one-dimensional FETs. *IEDM Tech. Digest*, pp. 185–188, 2008.
- [58] D. S. Fisher and P. A. Lee. Relation between conductivity and transmission matrix. *Phys. Rev. B*, vol. 23, pp. 6851–6854, 1981.
- [59] T. González, C. González, J. Mateos, D. Pardo, L. Reggiani, O. M. Bulashenko, and J. M. Rubi'. Universality of the 1/3 Shot-Noise Suppression Factor in Nondegenerate Diffusive Conductors. *Phys. Rev. Lett.*, vol. 80, pp. 2901–2904, 1998.
- [60] E. V. Sukhorukov and D. Loss. Universality of Shot-Noise in Multiterminal Diffusive Conductors. *Phys. Rev. Lett.*, vol. 80, pp. 4959–4962, 1998.
- [61] Ya. M. Blanter and M. Büttiker. Shot-noise current-current correlations in multiterminal diffusive conductors. *Phys. Rev. B*, vol. 56, pp. 2127–2136, 1997.
- [62] A. H. Steinbach, J. M. Martinis, and M. H. Devoret. Observation of Hot-Electron Shot Noise in a Metallic Resistor. *Phys. Rev. Lett.*, vol. 76, pp. 3806–3809, 1996.
- [63] R. J. Schoelkopf, P. J. Burke, A. A. Kozhevnikov, D. E. Prober, and M. J. Rooks. *Phys. Rev. Lett.*, vol. 78, pp. 3370–3373, 1997.
- [64] G. Iannaccone, F. Crupi, and B. Neri. Suppressed shot noise in trap-assisted tunneling of metal-oxide- semiconductor capacitors. *Appl. Phys. Lett.*, vol. 77, pp. 2876–2878, 2000.
- [65] G. Iannaccone, F. Crupi, B. Neri, and S. Lombardo. Theory and experiment of suppressed shot noise in stress- induced leakage currents. *IEEE Trans. Electron Devices*, vol. 50, pp. 1363–1369, 2003.

- [66] L. Di Carlo, J. R. Williams, Y. Zhang, D. T. McClure, and C. M. Marcus. Shot Noise in Graphene. *Phys. Rev. Lett.*, vol. 100, pp. 156801, 2008.
- [67] A. Betti, G. Fiori, and G. Iannaccone. Shot noise analysis in quasi one-dimensional Field Effect Transistors. *International Conference on Noise and Fluctuations*, pp. 581–584, 2009.
- [68] A. Betti, G. Fiori, and G. Iannaccone. Enhanced shot noise in carbon nanotube field-effect transistors. *Appl. Phys. Lett.*, vol. 95, pp. 252108, 2009.
- [69] A. Betti, G. Fiori, and G. Iannaccone. Enhanced shot noise in carbon nanotube FETs due to electron-hole interaction. *IWCE Tech. Digest*, pp. 1–4, 2010.
- [70] G. Fiori and G. Iannaccone. Coupled Mode Space Approach for the Simulation of Realistic Carbon Nanotube Field-Effect Transistors. *IEEE Trans. on Nanotechnology*, vol. 6, pp. 475–479, 2007.
- [71] J. Guo, S. Datta, M. Lundstrom, and M. P. Anantam. Towards Multi-Scale Modeling of Carbon Nanotube Transistors. *Int. J. Multiscale Comput. Eng.*, vol. 2, pp. 257, 2004.
- [72] G. Fiori and G. Iannaccone. Three-dimensional simulation of one-dimensional transport in silicon nanowire transistors. *IEEE Trans. on Nanotechnology*, vol. 6, pp. 524–529, 2007.
- [73] J. Wang, E. Polizzi, and M. Lundstrom. A three-dimensional quantum simulation of silicon nanowire transistors with the effective-mass approximation. *J. Appl. Phys.*, vol. 96, pp. 2192–2203, 2004.
- [74] G. Fiori, G. Iannaccone, and G. Klimeck. A three-dimensional simulation study of the performance of carbon nanotube field-effect transistors with doped reservoirs and realistic geometry. *IEEE Trans. Electron Devices*, vol. 53, pp. 1782–1788, 2006.
- [75] H. H. Park, S. Jin, Y. J. Park, and H. S. Min. "Quantum simulation of noise in silicon nanowire transistors". *J. Appl. Phys.*, vol. 104, pp. 023708, 2008.
- [76] T. Gramespacher and M. Büttiker. Local densities, distribution functions, and wave-function correlations for spatially resolved shot noise at nanocontacts. *Phys. Rev. B*, vol. 60, pp. 2375–2390, 1999.

- [77] E. V. Sukhorukov and D. Loss. Universality of Shot Noise in Multiterminal Diffusive Conductors. *Phys. Rev. Lett.*, vol. 80, pp. 4959–4962, 1998.
- [78] M. Büttiker. Flux-Sensitive Correlations of Mutually Incoherent Quantum Channels. *Phys. Rev. Lett.*, vol. 68, pp. 843–846, 1992.
- [79] H. H. Park, S. Jin, Y. J. Park, and H. S. Min. "Quantum simulation of noise in silicon nanowire transistors with electron-phonon interactions". *J. Appl. Phys.*, vol. 105, pp. 023712, 2009.
- [80] A. A. Abidi. "High-Frequency Noise Measurements on FET's with Small Dimensions". *IEEE Transactions on electron devices*, vol. 33, pp. 1801–1805, 1986.
- [81] R. Navid and R. W. Dutton. "The physical phenomena responsible for excess noise in short-channel MOS devices". *IEDM Tech. Digest*, pp. 75–78, 2002.
- [82] K. Han, H. Shin, and K. Lee. "Analytical Drain Thermal Noise Current Model Valid for Deep Submicron MOSFETs". *IEEE Transactions on electron devices*, vol. 51, pp. 261–269, 2004.
- [83] M. R. Döring, A. Hangleiter, and N. Klötzer. Electron-hole correlation effects in generation-recombination noise. *Phys. Rev. B*, vol. 45, pp. 1163–1171, 1992.
- [84] J. Bardeen. Tunneling from a many-particle point of view. *Phys. Rev. Lett.*, vol. 6, pp. 57–59, 1961.
- [85] G. Iannaccone and B. Pellegrini. Unified approach to electron transport in double-barrier structures. *Phys. Rev. B*, vol. 52, pp. 17406–17412, 1995.
- [86] H. J. Reittu. Fermi's golden rule and bardeen's tunneling theory. *Am. J. Phys.*, vol. 63, pp. 940–944, 1995.
- [87] M. T. Ahmadi, R. Ismail, M. L. P. Tan, and V. K. Arora. The Ultimate Ballistic Drift Velocity in Carbon Nanotubes. *Journ. of Nanomat.*, pp. 769250, 2008.
- [88] M. Bresciani, P. Palestri, and D. Esseni. Simple and efficient modeling of the E-k relationship and low-field mobility in Graphene Nano-Ribbons. *Solid-State Electronics*, vol. 54, pp. 1015–1021, 2010.



- [89] D. A. Areshkin, D. Gunlycke, and C. T. White. Ballistic Transport in Graphene Nanostrips in the Presence of Disorder: Importance of Edge Effects. *Nano Lett.*, vol. 7, pp. 204–210, 2007.
- [90] D. Querlioz, Y. Apertet, A. Valentin, K. Huet, A. Bournel, S. Galdin-Retailleau, and P. Dollfus. Suppression of the orientation effects on bandgap in graphene nanoribbons in the presence of edge disorder. *Appl. Phys. Lett.*, vol. 92, pp. 042108, 2008.
- [91] A. Betti, G. Fiori, G. Iannaccone, and Y. Mao. Physical insights on graphene nanoribbon mobility through atomistic simulations. *IEDM Tech. Digest*, pp. 897–900, 2009.
- [92] A. Betti, G. Fiori, and G. Iannaccone. Atomistic investigation of low-field mobility in graphene nanoribbons. *IEEE Trans. on Electron Devices*, DOI:10.1109/TED.2010.2100045, 2011.
- [93] I. Deretsiz, G. Forte, A. Grassi, A. La Magna, G. Piccitto, and R. Pucci. A multiscale study of electronic structure and quantum transport in  $C_{6n^2}H_{6n}$ -based graphene quantum dots. *J. Phys.: Condens. Matter*, vol. 22, pp. 095504, 2010.
- [94] K. Rytkönen, J. Akola, and M. Manninen. Density functional study of alkali metal atoms and monolayers on graphite (0001). *Phys. Rev. B*, vol. 75, pp. 075401, 2007.
- [95] R. Saito, G. Dresselhaus, and M. Dresselhaus. Physical Properties of Carbon Nanotubes. *Imperial College Press, London*, 2003.
- [96] A. Betti, G. Fiori, and G. Iannaccone. Strong mobility degradation in ideal graphene nanoribbons due to phonon scattering. *submitted to Appl. Phys. Lett.*, 2011.
- [97] A. Betti, G. Fiori, and G. Iannaccone. Electron-phonon scattering in graphene nanoribbons. *submitted*, 2011.
- [98] R. Kubo. Statistical-Mechanical Theory of Irreversible Processes. *J. Phys. Soc. Jpn.*, vol. 12, pp. 570, 1957.
- [99] E. Mariani and F. von Oppen. Flexural Phonons in Free-Standing Graphene. *Phys. Rev. Lett.*, vol. 100, pp. 076801, 2008.
- [100] A. C. Ferrari, J. C Meyer, V. Scardaci, C. Casiraghi, M. Lazzeri, F. Mauri, S. Piscanec, D. Jiang, K. S. Novoselov, S. Roth, and

- A. K. Geim. Raman Spectrum of Graphene and Graphene Layers. *Phys. Rev. Lett.*, vol. 97, pp. 187401, 2006.
- [101] C. Casiraghi, A. Hartschuh, H. Qian, S. Piscanec, C. Georgi, A. Fasoli, K. S. Novoselov, D. M. Basko, and A. C. Ferrari. Raman Spectroscopy of Graphene Edges. *Nano Lett.*, vol. 9, pp. 1433–1441, 2009.
- [102] S. Poli, M. G. Pala, T. Poiroux, S. Deleonibus, and G. Bacarani. Size Dependence of Surface-Roughness-Limited Mobility in Silicon-Nanowire FETs. *IEEE Trans. Electron Devices*, vol. 55, pp. 2968–2976, 2008.
- [103] M. Evaldsson, I. V. Zozoulenko, H. XU, and T. Heinzel. Edge-disorder-induced anderson localization and conduction gap in graphene nanoribbons. *Phys. Rev. B*, vol. 78, pp. 161407, 2008.
- [104] T. Stauber, N. M. R. Peres, and F. Guinea. Electronic transport in graphene: A semiclassical approach including midgap states. *Phys. Rev. B*, vol. 76, pp. 205423, 2007.
- [105] C. Casiraghi, S. Pisana, K. S. Novoselov, A. K. Geim, and A. C. Ferrari. Raman fingerprint of charged impurities in graphene. *Appl. Phys. Lett.*, vol. 91, pp. 233108, 2007.
- [106] E. H. Hwang, S. Adam, and S. Das Sarma. Carrier Transport in Two-Dimensional Graphene Layers. *Phys. Rev. Lett.*, vol. 98, pp. 186806, 2007.
- [107] J. Lee and H. Spector. Dielectric response function for a quasi-one-dimensional semiconducting system. *J. Appl. Phys.*, vol. 57, pp. 366–372, 1985.
- [108] D. A. Greenwood. The Boltzmann Equation in the Theory of Electrical Conduction in Metals. *Proc. Phys. Soc. London*, vol. 71, pp. 585, 1958.
- [109] H. Suzuura and T. Ando. Phonons and electron-phonon scattering in carbon nanotubes. *Phys. Rev. B*, vol. 65, pp. 235412, 2002.
- [110] M.-Q. Long, L. Tang, D. Wang, L. Wang, and Z. Shuai. Theoretical Predictions of Size-Dependent Carrier Mobility and Polarity in Graphene. *JACS*, vol. 131, pp. 17728–17729, 2009.

- [111] V. Perebeinos, J. Tersoff, and P. Avouris. Mobility in Semiconducting Carbon Nanotubes at Finite Carrier Density. *Nano Lett.*, vol. 6, pp. 205–208, 2006.
- [112] A. H. Castro Neto, F. Guinea, N. M. R. Peres, K. S. Novoselov, and A. K. Geim. The electronic properties of graphene. *Rev. Mod. Phys.*, vol. 81, pp. 109–162, 2009.
- [113] C. Berger, Z. Song, T. Li, X. Li, A. Y., Ogbazghi, R. Feng, Z. Dai, A. N. Marchenkov, E. Conrad, P. N. First, and W. A. de Heer. *J. Phys. Chem.*, vol. 108, pp. 19912, 2004.
- [114] F. Sols, F. Guinea, and A. H. Castro Neto. Coulomb Blockade in Graphene Nanoribbons. *Phys. Rev. Lett.*, vol. 99, pp. 166803, 2007.
- [115] L. Liao, J. Bai, R. Cheng, Y.-C. Lin, S. Jiang, Y. Huang, and X. Duan. Top-Gated Graphene Nanoribbon Transistors with Ultrathin High- $k$  Dielectrics. *Nano Lett.*, vol. 10, pp. 1917–1921, 2010.
- [116] T. Kitayama, H. Minari, and N. Mori. Full-band and atomistic study of electron-phonon interaction in graphene nanoribbons. *J. Phys.: Conference Series*, vol. 193, pp. 012112, 2009.
- [117] L. Pietronero, S. Strässler, and H. R. Zeller. Electrical conductivity of a graphite layer. *Phys. Rev. B*, vol. 22, pp. 904–910, 1980.
- [118] D. Gunlycke, H. M. Lawler, and C. T. White. Room-temperature ballistic transport in narrow graphene strips. *Phys. Rev. B*, vol. 75, pp. 085418, 2007.
- [119] R. Mickevicius and V. Mitin. Acoustic-phonon scattering in a rectangular quantum wire. *Phys. Rev. B*, vol. 48, pp. 17194–17201, 1993.
- [120] A. Kabasi, D. Chattopadhyay, and C. K. Sarkar. *J. Appl. Phys.*, vol. 65, pp. 1598, 1989.
- [121] J. L. Manes. Symmetry-based approach to electron-phonon interactions in graphene. *Phys. Rev. B*, vol. 76, pp. 045430, 2007.
- [122] X. Zhou, J.-Y. Park, S. Huang, J. Liu, and P. L. McEuen. Band Structure, Phonon Scattering, and the Performance Limit

- of Single-Walled Carbon Nanotube Transistors. *Phys. Rev. Lett.*, vol. 95, pp. 146805, 2005.
- [123] S. Malola, H. Häkkinen, and P. Koskinen. Comparison of Raman spectra and vibrational density of states between graphene nanoribbons with different edges. *Eur. Phys. Journ. D*, vol. 52, pp. 71–74, 2008.
- [124] P. Michetti and G. Iannaccone. Analytical Model of One-Dimensional Carbon-Based Schottky-Barrier Transistors. *IEEE Trans. Electron Devices*, vol. 57, pp. 1616–1625, 2010.
- [125] L. Wirtz and A. Rubio. The phonon dispersion of graphite revised. *Solid State Communications*, vol. 131, pp. 141–152, 2004.
- [126] G. D. Mahan. Oscillations of a thin hollow cylinder: carbon nanotubes. *Phys. Rev. B*, vol. 65, pp. 235402–235407, 2002.
- [127] Z. K. Wang, H. S. Lim, S. C. Ng, B. Özyilmaz, and M. H. Kuok. Brillouin scattering study of low-frequency bulk acoustic phonons in multilayer graphene. *Carbon*, vol. 46, pp. 2133–2136, 2008.
- [128] A. V. Rozhkov, S. Savel'ev, and F. Nori. Electronic properties of armchair graphene nanoribbons. *Phys. Rev. B*, vol. 79, pp. 125420, 2009.
- [129] L. M. Woods and G. D. Mahan. Electron-phonon effects in graphene and armchair (10,10) single-wall carbon nanotubes. *Phys. Rev. B*, vol. 61, pp. 10651–10663, 2000.
- [130] M. Lundstrom. Fundamental of carrier transport. *Cambridge University Press, Second edition*, 2000.
- [131] B. K. Ridley. The electron-phonon interaction in quasi-two dimensional semiconductor quantum-well structures. *J. Phys. C: Solid State Phys.*, vol. 15, pp. 5899–5917, 1982.
- [132] G. Pennington and N. Goldsman. Semiclassical transport and phonon scattering of electrons in semiconducting carbon nanotubes. *Phys. Rev. B*, vol. 68, pp. 045426, 2003.
- [133] K. Sugihara. Thermoelectric power of graphite intercalation compounds. *Phys. Rev. B*, vol. 28, pp. 2157–2165, 1983.

- [134] M. Ishigami, J. H. Chen, W. G. Cullen, M. S. Fuhrer, and E. D. Williams. Atomic Structure of Graphene on SiO<sub>2</sub>. *Nano Lett.*, vol. 7, pp. 1643–1648, 2007.
- [135] R. Kotlyar, B. Obradovic, P. Matagne, M. Stettler, and M. D. Giles. Assessment of room-temperature phonon-limited mobility in gated silicon nanowires. *Appl. Phys. Lett.*, vol. 84, pp. 5270, 2004.
- [136] A. Betti, G. Fiori, and G. Iannaccone. Full band assesment of phonon-limited mobility in graphene nanoribbons. *IEDM Tech. Digest*, pp. 728–731, 2010.
- [137] E. H. Hwang and S. Das Sarma. Acoustic phonon scattering limited carrier mobility in two-dimensional extrinsic graphene. *Phys. Rev. B*, vol. 77, pp. 115449, 2008.
- [138] S. Jin, M. V. Fischetti, and T. Tang. Modeling of electron mobility in gated silicon nanowires at room temperature: Surface roughness scattering, dielectric screening, and band nonparabolicity. *Journ. Appl. Phys.*, vol. 102, pp. 083715, 2007.
- [139] V. Perebeinos, S. V. Rotkin, A. G. Petrov, and P. Avouris. The Effects of Substrate Phonon Mode Scattering on Transport in Carbon Nanotubes. *Nano Lett.*, vol. 9, pp. 312–316, 2009.
- [140] V. Perebeinos, J. Tersoff, and P. Avouris. Electron-Phonon Interaction and transport in Semiconducting Carbon Nanotubes. *Phys. Rev. Lett.*, vol. 94, pp. 086802, 2005.
- [141] P. Neugebauer, M. Orlita, C. Faugeras, A. L. Barra, and M. Potemski. How Perfect Can Graphene Be? *Phys. Rev. Lett.*, vol. 103, pp. 136403, 2009.
- [142] J. Chen, T. Saraya, and T. Hiramoto. Experimental Investigations of Electron Mobility in Silicon Nanowire nMOSFETs on (110) Silicon-on-Insulator. *IEEE Electron Device Letters*, vol. 30, pp. 1203–1205, 2009.
- [143] Xavier Oriols. Quantum mechanical effects on noise properties of nanoelectronic devices: application to Monte Carlo simulation. *IEEE Trans. on Electron Devices*, vol. 50, pp. 1830–1836, 2003.

- [144] Y. W. Son, M. L. Cohen, and S. Louie. Energy gaps in graphene nanoribbons. *Phys. Rev. Lett.*, vol. 97, pp. 216803, 2006.

# List of Acronyms

**CMOS** Complementary Metal-Oxide Semiconductor.

**ITRS** International Technology Roadmap for Semiconductors.

**GNR** Graphene NanoRibbon.

**CNT** Carbon NanoTube.

**SNW** Silicon NanoWire.

**1D** One-Dimensional.

**2D** Two-Dimensional.

**3D** Three-Dimensional.

**FET** Field-Effect Transistor.

**NEGF** Non-Equilibrium Green Function formalism.

**MOSFET** Metal-Oxide-Semiconductor Field-Effect Transistor.

**PN** Partition Noise.

**PN ON** On-Diagonal Partition Noise.

**PN OFF** Off-Diagonal Partition Noise.

**IN** Injection Noise.

**SC-MC** Self-Consistent Monte Carlo simulations.

**LB** Landauer-Büttiker.

**DOS** Density of States.

**LDOS** Local Density of States.

**LER** Line-Edge Roughness.

**FB** Full-Band.

**DPA** Deformation Potential Approximation.

**LA** Longitudinal Acoustic phonon mode.

**TA** Transversal Acoustic phonon mode.

**LO** Longitudinal Optical phonon mode.

**TO** Transversal Optical phonon mode.

**ZA** Out-of-plane (flexural) Acoustic phonon mode.

**ZO** Out-of-plane (flexural) Optical phonon mode.

**TB** Tight-Binding.

**4NNFC** Fourth Nearest Neighbors Force Constant approach.

**AC** Acoustic.

**OP** Optical.

**SO** Surface Optical.

**ABS** Absorption.

**EM** Emission.

**RPA** Random Phase Approximation.

**SQL** Size Quantum Limit.

**IIS** Intraband Intravalley Scattering.

**IISNS** Intraband Intravalley Scattering No Spinor.

**2DPNS** 2D Phonons No Spinor.



# Curriculum Vitae

Alessandro Betti was born in Pisa, Italy, on April 30, 1980. He studied Physics at the University of Pisa. He received the M.S. degree in Physics from the University of Pisa in 2007 with the master thesis entitled *L'effetto Jahn-Teller sullo ione  $Ti^{3+}$  in semiconduttori III-V* which was supervised by Prof. L. Martinelli. In November 2007 he joined the Department of Electrical Engineering of Pisa, where he received the Ph.D. degree in Electrical Engineering in 2011. His research interest focus on transport and noise properties of silicon and carbon-based quasi-one dimensional devices.